Università degli Studi di Cagliari

DOTTORATO DI RICERCA

Scienze e Tecnologie Chimiche

Ciclo XXXI

TITOLO TESI

Structural Properties of β-Lactamase Inhibtors: Computational Study to Enhance Permeability Through General Porins of Gram-Negative Bacteria

Settore scientifico disciplinare di afferenza

CHIM/02

Presentata da:	Alessandro Pira
Coordinatore Dottorato	Prof. Stefano Enzo
Tutor	Prof. Mariano Casu Prof. Matteo Ceccarelli Dr. Mariano Andrea Scorciapino

Esame finale anno accademico 2017 – 2018

Abstract

The rapid development of resistance to many current antibiotics in numerous pathogenic bacterial strains represents an urgent global public health problem. Therefore, we need to develop alternative strategies for the development of new molecules characterized by appropriate therapeutic properties. Among the pathogens in question, Gram-negative bacteria, in particular, represent an important challenge because of their external membrane, which represents and additional barrier against any molecular species.

This work is focused on the investigation of the permeability of β-lactamase inhibitors through porins, considered the main pathway for the entry of small polar molecules into Gram negative bacteria. We selected OmpF (Outer Membrane Protein F) from *E. coli* as a model system of porins from the bacterial family of *Enterobacteriaceae*. The understanding of the physico-chemical parameters that govern the permeation process is a prerequisite to design/optimize antibacterials with improved efficacy. To this aim, *Molecular Dynamics* (MD) simulations combined with the enhanced sampling technique *Well-Tempered Metadynamics* (WT-METAD) provided important details, at the atomic level, on the interactions between the permeating molecules and these protein channels and allowed overcoming limitations of experimental techniques like electrophysiology. The latter, which is based on the measurement of ionic current kinetics through the pores upon addition of specific molecules inside the channel itself, does not allow discriminating between the effective translocation of the molecules or the interaction with binding sites located within the channel.

The presentation of the work has been divided into three main sections. First, the structural comparison of different porins from the *Enterorobacteriaceae* showed that

OmpF and OmpC from *E. Coli* can be actually considered as good model system for the entire channel family. Then, MD and WT-METAD simulations have been used to guide the development of an experimental method for the quantification of the flow of solutes through these bacterial pores by using electrophysiology combined with single-channel conductance. Finally, the comparative study of the free energy surface for the permeation of selected β-lactamase inhibitors through OmpF showed how the free energy profile of permeation process depend of a combination between steric hindrance (entropic contribution) and electrostatic interaction between pore and substrate (enthalpic contribution).

Contents:

1 Introduction

Resistance is a natural process related to bacteria evolution. It occurs when the microrganisms undergo replication and resistant traits are introduced by chance of exchanged between different cells. This is accelerated by the pressure exerted by the use of the antibiotics themselves in human and human-related activities. The use, abuse and misuse of antimicrobial drugs, thus, accelerate the selection of drug-resistant strains. Poor infection control practices, inadequate sanitary conditions and inappropriate food-handling encourage the further spread of antimicrobial resistance. Since bacteria evolve under antibiotic pressure, people will always need new antibiotics to fight bacteria. However, today, our inability to come up with new effective molecules has turned simple treatable infections into deadly ones, representing a serious challenge for modern medicine worldwide.[1]

a)

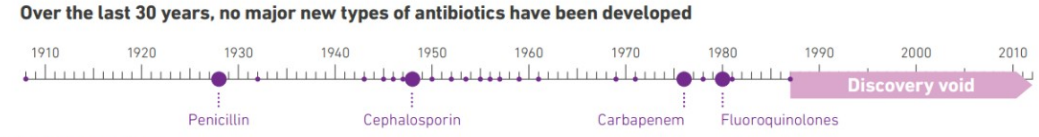

World Health Organization
"ANTIMICROBIAL RESISTANCE" Global Report on surveillance 2014

b)

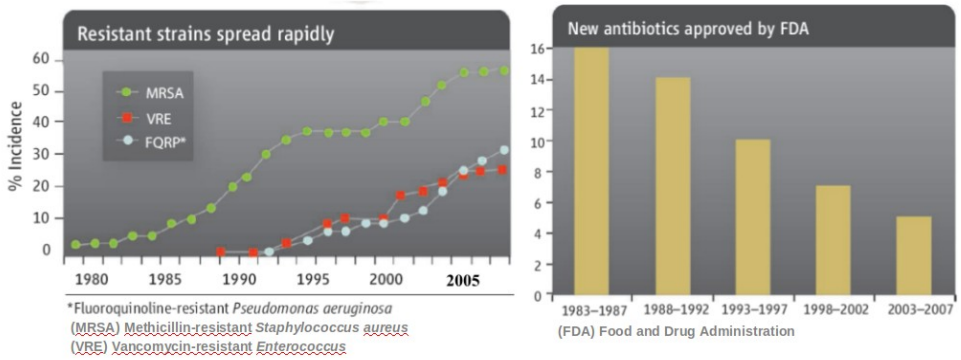

Gary Taubes.
"The Bacteria Fight Back" Science, 321(5887):356–361, 2008.

Fig. 1.1: a) Lack of new classes of antibiotics. Reprinted from [42]. b) Resistance is on rise while antibiotic discovery and development are on decline. Modified from [1].

The last decades have seen the appearance of “superbugs” which are able to counteract drugs from different families (multi-drug resistant MDR). The major problem for the development of new drugs is the difficulty to identify new chemical classes of antibiotics. The most common chemical scaffolds from which “new” antibiotics have been chemically built, were introduced a century ago (Fig. 1.1). During the years 60’ to 90’, the pharmaceutical companies focused their research on medicinal chemistry techniques that allowed easily obtaining many synthetic molecules by modifying scaffolds obtained earlier. This approach represented only an incremental improvement to the existing scaffolds and resulted to be a short-term strategy against bacteria. However, the abundance of new molecules on the market obtained with such approach has stopped the research in this field and has created the so-called innovation gap, i.e. the lack of fundamental knowledge and of rational rules to design completely new scaffolds. A more sustainable way to contrast resistance would be to discover completely new scaffolds. Such a scenario highlights the importance of developing alternative strategies aimed at finding new molecules characterized by therapeutic properties and at filling such innovation gap. (you need to explain what is the innovation gap, as I tried above).

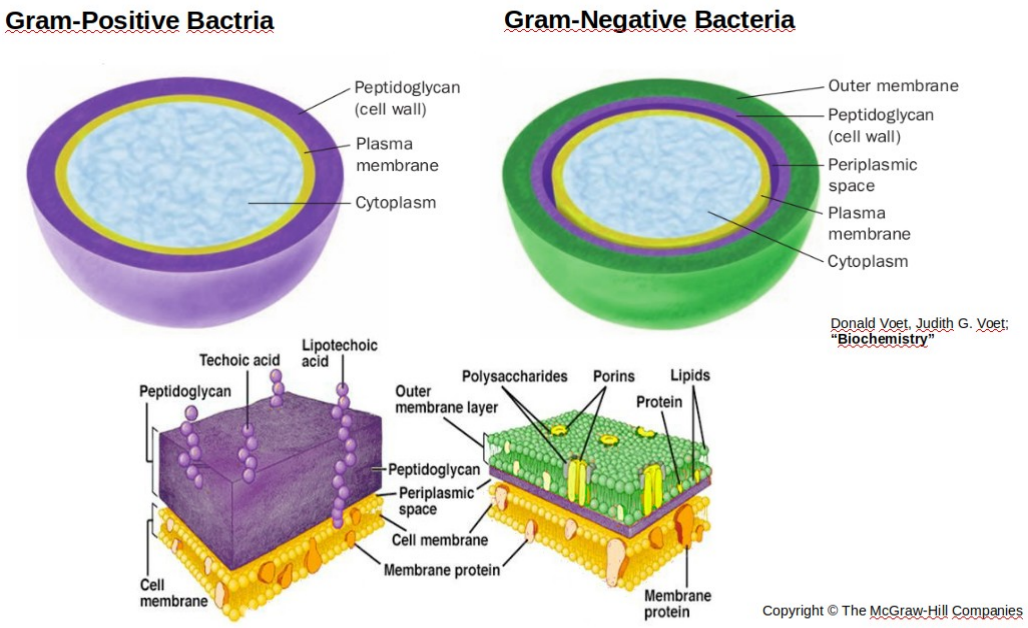

Fig. 1.2: Comparison between Gram-Positive and Gram-Negative bacteria is represented. Reprinted from [2]

1.2 Gram- Positive and Gram-Negative Bacteria

This class of pathogens is subdivided in two principal families: Gram-positive and Gram-negative bacteria (fig. 1.2). [2] From a structural point of view, these two groups differ mainly in the composition of their cell membrane. Gram-positive bacteria give a positive result in the Gram staining test, which is traditionally used to quickly classify them into the two mentioned broad categories according to their cell wall composition. Gram-positive bacteria take up the crystal violet stain used in the test, and then appear to be purple-colored when observed through a microscope. This is because the thick peptidoglycan layer in the bacterial cell wall retains the stain after it is washed away from the rest of the sample, in the decolorization stage of the test. In general, the Gram-positive bacteria are characterized by a cytoplasmic lipid membrane and a thick external peptidoglycan layer. Also teichoic acids and lipoids are present, forming the lipoteichoic acids, which serve as chelating agents and for certain mechanisms of adhesion. Only some species have a capsule, usually consisting of polysaccharides.

Gram-negative bacteria, on the other hand, do not retain the crystal violet stain used in the Gram staining method. They are characterized by a cell shell, which is composed of a thin peptidoglycan layer confined between an inner cytoplasmic cell membrane and the outer membrane. Thus, the cell wall of Gram-negative bacteria is more complex than that of the Gram-positive ones. Both gram-positive and gram-negative bacteria have a surface layer called S-layer. In gram-positive bacteria, the S-layer is attached to the peptidoglycan layer. In Gram-negative bacteria, S-layer is attached directly to the outer membrane.

Gram-negative bacteria represent a big challenge for the design of antibiotics because of the presence of the additional outer membrane (OM) that endows them with a more

effective protection against any molecular species. This OM is composed of a lipid bilayer containing lipopolysaccharides (LPS, which consists of lipid A, core polysaccharide, and the O antigen) in the outer leaflet and phospholipids in the inner leaflet, and acts as a real physical barrier for the diffusion of any molecule, especially those with a polar character. A family of protein channels, called porins, is expressed and inserted in the OM, working as passive transporters for polar molecules to overcome the OM.

1.3 Porins

It is possible, from a general point of view, to divide the porins in two groups: **selective porins** and **general porins**. The former group allows the entry of specific molecular species. These proteins are characterized by a lower accessible area with respect to the general porins, and by the presence of strongly selective, affinity binding sites. The presence of a stable and selective binding site reduces the rate at which specific substrates can penetrate through the channel, producing kinetics of saturation. The latter group, a family of nonspecific channels, allows the diffusive passage of water, ions and are widely recognized as the main access route for polar substrates to overcome the OM. Numerous classes of charged/polar antibiotics, including *β-lactam antibiotics* [4] and *β-lactamase inhibitors* [5], make use of these channels in order to enter the periplasm. Usually, general porins have a low degree of selectivity, which is mostly based on steric hindrance, structural features such as the molecular shape and their net charge, in addition to intrinsic chemical properties. The net flux of compounds through general porins is expected to be proportional to the gradient concentration of the compounds themselves. It is worth to note that not all bacterial species do express general porins.

The most studied general porin is OmpF (Outer Membrane Protein F) expressed as a trimer by the *E. Coli* species in low osmolarity conditions (fig. 3). It was the first porin to be crystallized in the ‘80. This protein confer membrane permeability to water, ions and small molecular species having a size < 600 D. It is characterized by a high negative charge. Its structure is that of β-barrel, determined by 16 antiparallel β-strands, with a central narrowing (due to the internal folding of the L3 loop), referred to as the Constriction Region (CR) (fig. 3). This region represents the steric filter. In addition,

OmpF is characterized by a clear separation of residues with opposite charge. In particular, the loop L3 itself has three negatively charged residues, D113, E117 and D121, exposed to the eyelet. In the barrel wall opposite to the loop L3, a cluster of positively charged residues is located, which is referred to as the Basic Ladder. This is composed by the residues K16, R42, R82 and R132.

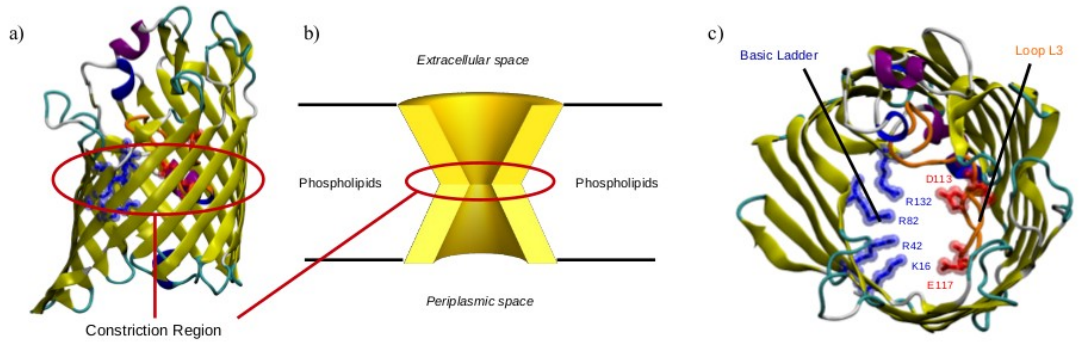

Fig. 1.3: PDB ID: 2OMF, 2Å resolution; a) side view of single monomer of OmpF; b) schematisation of hourglass-shape inserted in phospholipid bilayer; c) top view of single monomer of OmpF, the positive charged residues are represented in blue and the negative charged residues are represented in red.

The net charge separation at the level of the CR is responsible for the intrinsic transversal electric field in the eyelet. During the permeation, specific energetically favored interactions between the molecule and the protein wall (hydrogen bonds, salt bridges and general electrostatic interactions) might slow down the transport. More recent studies conducted by the research team, on the contrary, have shown that the presence of non-specific interactions, such as those due to the intrinsic electric field generated by the charge distribution inside the protein, could have great importance in facilitating the passage of polar molecules through the protein.[3] The mentioned charge separation at the level of the CR determines in fact a transverse electric field in the eyelet that would seem able to discriminate between different molecular species.

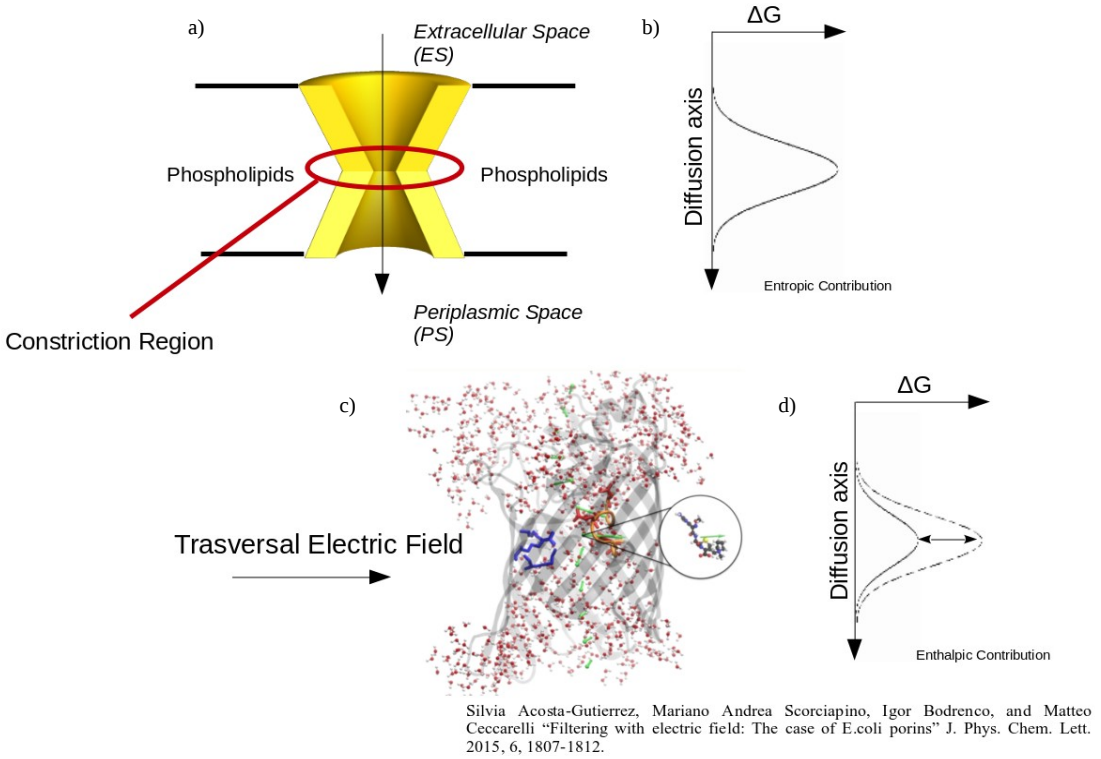

Fig. 1.4: a) Schematic representation of hourglass-shape inserted in phospholipid bilayer; b) hypothetical free energy profile of translocation process without specific interactions as due to steric hindrance only. c) Representation of substrate aligning its dipole moment in favor to the transversal electric field of OmpF during the translocation (reprinted from [3]); d) hypothetical free energy profile of translocation process with non-specific interactions (like dipole alignment) able to reduce the energy barrier for translocation.

Since the CR is the steric filter for transport, a permeating molecule will encounter a free energy barrier of entropic nature due to the small size of the CR. The ability of the molecule to align its electric dipole moment along the transversal electric field would compensate the steric barrier, thus allowing the substrate to finallyreach the periplasmic space with a lower energetic cost (fig. 4). This compensation is enthalpic in nature and depends on the distribution of charged groups over the structure of the permeating molecule.

1.4 β-Lactam Antibiotics, β-Lactamase Inhibitors and Bacteria Resistence

A typical example of polar antibiotic is represented by the class of β-lactam antibiotics. [4] Since Fleming's accidental discovery of the penicillin-producing mold, ninety years of steady progress has followed, and today the β-lactam group of compounds is the most successful example of natural product application and chemotherapy. The discovery of penicillin not only led to the era of the wonder drugs but also provided the most important antibiotics to Medicine.

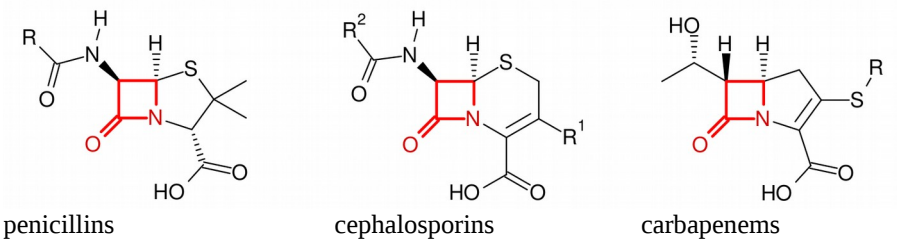

Fig. 1.5: 2D structure of three families of β-lactam antibiotics, the β-lactam ring is highlighted in red.

The β-lactam ring (cyclic amide) is the functional group that characterizes this family of antibiotics. The principal subgroups differs by the cycle condensed to the main cyclic amide (fig. 5):

- *Monolactams*: unique constituent lactam ring
- *Penicillins*: lactam ring condensed to a thiazolidine ring
- *Cephalosporins*: lactam ring condensed to a dihydrothiazine ring
- *Carbapenems*: lactam ring condensed to a pyrrole ring.

In order to exhibit their pharmacological effects, antibiotics must reach the periplasmic space (that is, the space between the outer and inner membrane) where their target is

located, i.e. specific enzymes involved in cell wall synthesis. The integrity of the bacterial cell wall is essential to maintaining cell shape and is also very specific to bacteria. Osmotic stability is preserved by a rigid peptidoglycan polymer consisting in alternating N-acetyl-muramic acid (NAM) and N-acetylglucosamine (NAG) units. A pentapeptide is attached to each NAM unit, and the cross-linking of D-alanine–D-alanine NAM pentapeptides is catalyzed by penicillin binding proteins (PBP), which act as transpeptidases. These cross-linkages between adjacent glycan strands confers the rigidity to the peptidoglycan. The structure of the β-lactam ring is similar to the D-alanine–D-alanine moiety of the NAM pentapeptide, from which the affinity of b-lactam antibiotics for the PBPs resulting in competitive inhibition of their enzymatic activity during cell wall synthesis. This results in acylation of the PBP, which renders the enzyme unable to catalyze further transpeptidation reactions. As the cell wall synthesis slows to a halt, constitutive peptidoglycan autolysis continues. At this point, the cell wall is compromised and permeability increases. Thus, the β-lactam mediated inhibition of transpeptidation causes cell lysis, although the specific details of penicillin's bactericidal effects are still being unveiled.[5]

The drug, however, once inside the periplasmic space can be subject to different defense mechanisms by bacteria. Efflux pumps [6], are capable of exporting a wide range of substrates from the periplasm to the surrounding environment against the gradient concentration (fig. 1.6). These pumps are an important determinant of multidrug resistance in many Gram-negative pathogens. Overexpression of AcrA, AcrB and TolC in combination with the low outer membrane permeability of organism, can contribute to decreased susceptibility to penicillins and cephalosporins, as well as quinolones, tetracycline, and chloramphenicol.

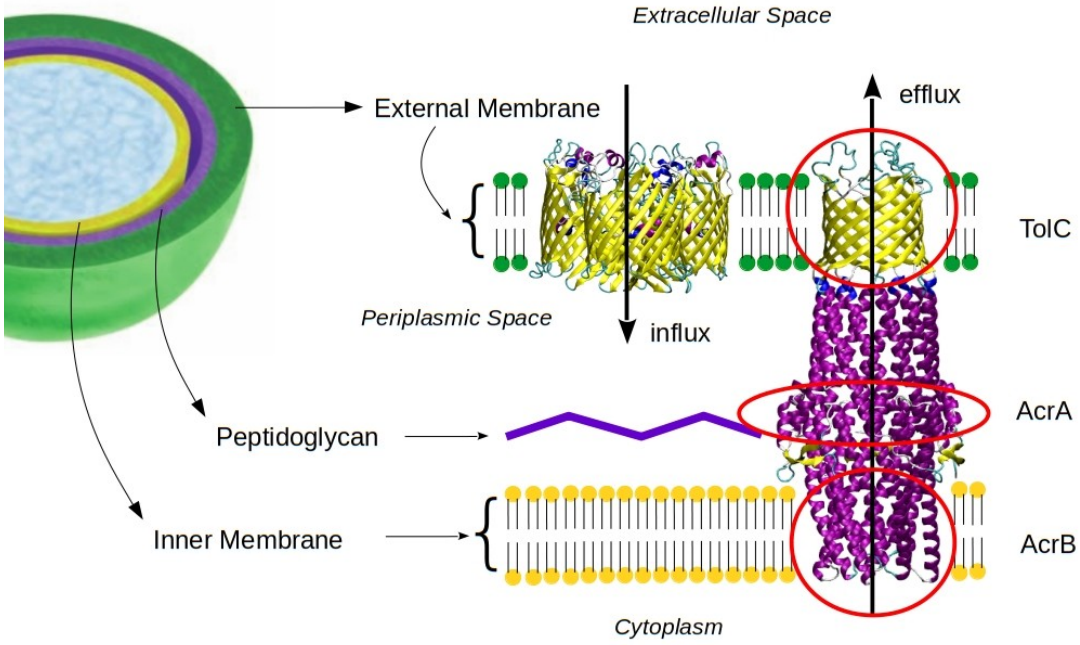

Fig. 1.6: Schematic representation of Gram-Negative cell.

Moreover, β-lactam antibiotics can be subject to degradation, and therefore reduced to ineffectiveness, by a specific family of enzymes known by the name of β-lactamases. Serine β-lactamases hydrolyze the β-lactam ring of antibacterial agents. The enzyme's serine residue first exerts a nucleophilic attack to β-lactam carbonyl group, with the cooperation of a base residue to activate the serine, resulting in the formation of the acyl-enzyme. The, the latter is hydrolyzed (deacylation) by a water molecule in the active site to give a non-β-lactam molecule and to regenerate the active site.

The presence of this family of enzymes that perturb the activity of antibiotics requires the necessity to develop also a class of inhibitors of β-lactamases in parallel to antibiotics development. [7] The most known representative of this class of molecule is the clavulanic acid, a β-lactam β-lactamase inhibitor (fig. 1.7).

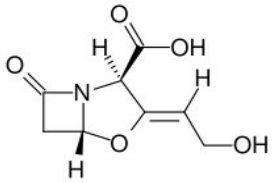

Fig. 1.7: 2D structure of Clavulanic Acid, a β-lactam-β-lactamases inhibitor.

The affinity for β-lactamases of these molecules is larger than antibiotics and so they react in their place. Sulbactam and tazobactam are two other β-lactam-β-lactamases inhibitors investigated in this thesis (fig. 3.9). However, the severe limitation of β-lactam inhibitors is the irreversibility of their action and their specific efficacy towards only one class of enzymes, while being absolutely ineffective towards other classes of degradative enzymes.

For these reasons, new classes of non-β-lactam inhibitors are attracting increasing interest. In this work, avibactam and its derivatives belonging to the group of *diazabicyclooctans* have been investigated. Avibactam is a reversible inhibitor with activity against a wide spectrum of enzymes. The key step is the diacylation, that occurs with closing of the ring instead of hydrolysis. We selected inhibitors with the same scaffold as avibactam, namely, nacubactam, a modificed nacubactam, relebactam and zidebactam (fig. 3.10), in order to understand how side chains and chemical groups can influence the interaction with the porin and, thus, modulate the energetic profile of the permeation process.

Boronic acid is another very recent class of non-β-lactam β-lactamase inhibitors of which studies are in progress. These compounds were described as forming reversible,

dative covalent bonds with serine proteases and inhibiting these enzymes by assuming tetrahedral reaction intermediates. Further study demonstrated that these compounds, when lacking the β-lactam motif, form adducts that resemble the geometry of the tetrahedral transition state of the β-lactamase hydrolytic reaction.

However, the very first step for the action of both the antibiotics and the inhibitors mentioned above is represented by the permeation through the bacterial porins. We focused our attention on this fundamental step, in order to understand the physico-chemical parameters that control the permeation of these drugs through porins.

1.5 Experimental Techniques

The main problem of the permeation process is that a robust and direct method to measure the permeability of different substrates through porins does not exist yet.

In liposome swelling assay experiments (Fig. 1.8), proteins are reconstituted into liposomes and the permeability of the channels is assumed to be proportional to the variation of the optical density of these liposomes over time, in the presence of a suspension of the substrate to study. The method is limited to a comparison of different compounds because we cannot establish how many porins are in the liposome surface.

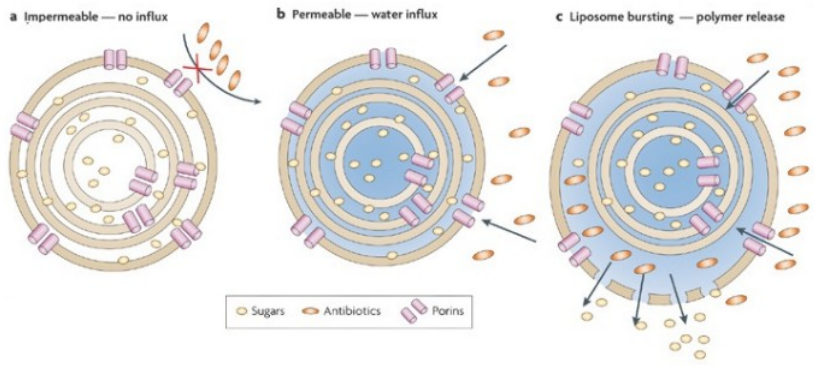

Fig. 1.8: Scheme of a liposome swelling assays experiment. Proteins are added to a solution of lipids and sugars; the lipids will reconstitute into liposomes. the liposomes are then mixed in a solution with different optical density and with the same osmotic pressure. (a) If the proteins are impermeable to the antibiotic, no change in the turbidity of the solution is observed. If the antibiotics permeate in the liposomes (b), they will enlarge and eventually release the sugars, thus reducing the optical density of the medium. Reprinted from [8]

In the literature, until a few years ago, the studies started from the assumption that the CR of general porins works as a binding site for permeating molecules. By increasing the internal concentration, the rate of permeation would increase. The only experimental

technique that allows obtaining the flux of different antibiotics in the channel is represented by electrophysiology (fig. 1.9). [9], [1[10] The technique is based on the reconstruction of a double artificial lipid layer, which separates two cells containing the electrolytic solutions, where porins are reconstituted after insertion in solution. The application of an electric potential difference between the two cells induces an ionic current through the inserted porins. The addition of a certain amount of antibiotic provokes some interruption of the current due to the occupation of the pore (fig. 1.10). The residence times that are measured reflect the protein-substrate affinity.

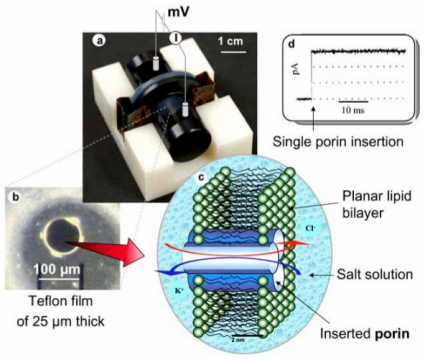

Fig. 1.9: Schematic representation of a typical planar bilayer set-up for ion current recording. ı.a) Two half cells made of Delrine separated by a 25 Îijm Teflon foil with a hole in the center, clamped together ı.b) Microscope picture of the teflon hole.c) Schema of a lipid bilayer with a reconstituted trimeric porin. d) The insertion of a single channel will give raise to a jump in conductance. Reprinted from [11]

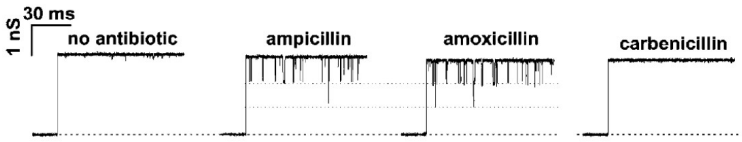

Fig. 1.10: Single-channel ion current trace: current interruption without antibiotics and in presence of Ampicillin, in presence of Amoxicillin and in presence of Carbenicillin. Reprinted from [9]

However, the main limitation of this technique is that we cannot obtain clear information on the dynamics of the system. In fact the substrate, once released from the binding site, supposed near/at the CR, would have the same probability of performing a clear shift over the channel or returning to the starting chamber. Thus it is not possible discriminating between the real translocation of the substrates and the simple interaction with binding sites within the channel without transport (fig. 1.11). Moreover, the difficulty in measuring short temporal changes in the ionic current (they should be larger than 50 μs) induced by substrates requires sophisticated methods of analyzing background noise.

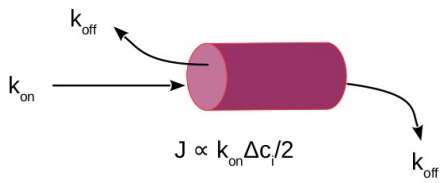

Fig. 1.11: The diffusion model is schematized: the flux into the pore J_{on} is proportional to the concentration gradient of *i*th species c_i and a constant ratio k_{on}.

The absence of further experimental techniques that allow a quantitative analysis combined with the importance of studying the process at the atomic level justify the use of computer simulation techniques.

Through molecular dynamics (MD) simulations it is possible to observe the interactions that would explain the high residence times found through electrophysiology for specific antibiotics. The classical molecular dynamics, however, presents a problem related to time scales: it may take an extremely long time to observe a biological process of major importance, which is shown by the experiments to be on the order of hundreds of microseconds/milliseconds. The sampling technique is of

fundamental importance, especially for those systems where the ergodicity is questioned by the complexity of the hypersurface that describes the energy potential of the system itself. In this context, metadynamics, through the addition of a bias (positive Gaussian potential) at regular intervals, allows the system to accelerate the visit of all possible microstates. Further, the bias used to accelerate the sampling, when integrated and the sign inverted, allow the reconstruction of the free energy profile of the process under investigation. [18]

The research project was aimed at rationalizing the transport of β-lactamase inhibitors through porins of Gram-negative bacteria. Porins from different bacterial species belonging to the same *Enterobacteriaceae* family were compared in order to find possible differences or analogies. Then different substrates were selected in order to understand physico-chemical parameters governing the permeation process and molecule's features that can be optimized to enhance the process. The more general purpose is to predict the permeability of a given substrate, which in turn will be modulated by physico-chemical properties, such as size, shape, dipole, charge distribution and presence of specific substituents. This approach will provide guidelines for a more targeted and efficient drug-design.

Systems of this complexity require very high computational costs. Thanks to the ever increasing computers performance, especially the new architectures of modern GPUs (Graphics Processing Unit) combined with the optimization of accurate methods and software codes, today it is possible to investigate the most interesting biological processes with atomistic details. Further, the development and integration of new databases and / or the expansion of those already available can help enormously in undertaking this kind of studies.

2 Methods

2.1 Molecular Dynamics

Classical *Molecular Dynamics* simulations (MD) allow reproducing at atomic level the temporal evolution of any system under study. This fundamental technique is used to gain atomistic details of molecular processes and thus predict and/or confirm experimental results.

In general, a MD simulation allows monitoring the structural and dynamical properties of the system under investigation, also when composed by different subsystems, like the complex biological machineries. It has allowed the study of numerous phenomena of biological interest, such as stability and conformational changes of proteins, lipids, carbohydrates and nucleic acids, molecular recognition, e.g. in the study of the formation of enzyme-substrate complexes, protein-protein interactions, DNA, biological membranes, metal-organic complexes or transport phenomena through protein channels. In this section, the basic concepts of MD will be briefly recalled; more details can be found in the book by C.J. Cramer. [12]

The energy calculation of any molecular system would require the rigorous resolution of the Schrödinger equation, where the Hamiltonian operator can be written as:

$$\hat{H} = -\sum_i \frac{\hbar^2}{2m_e}\nabla_i^2 - \sum_k \frac{\hbar^2}{2m_k}\nabla_k^2 - \sum_i \sum_k \frac{e^2 Z_k}{r_{ik}} + \sum_{i<j} \frac{e^2}{r_{ij}} + \sum_{k<l} \frac{e^2 Z_k Z_l}{r_{kl}} \qquad 1)$$

where the kinetic energy of both the atomic nuclei and the electrons, together with the potential energy of their interaction are included (*i* e *j* are indices for the electrons, *k* and *l* for the nuclei, $\hbar$ is the Planck constant divided by 2π, m_e is the mass of the electron, m_k that of the nucleus *k*, ∇^2 is the *Laplace operator*, *e* is the charge of the electron, *Z* is the atomic number, and r_{ab} is the distance between the particles *a* and *b)*. In a more compact form, the Hamiltonian is expressed as:

$$\hat{H} = T_e(\mathbf{r}) + T_N(\mathbf{R}) + V_{eN}(\mathbf{r},\mathbf{R}) + V_{ee}(\mathbf{r}) + V_{NN}(\mathbf{R}) \qquad 2)$$

where $T_e(\mathbf{r})$ is the kinetic energy of electrons, $T_N(\mathbf{R})$ is the kinetic energy of nuclei, $V_{eN}(\mathbf{r}, \mathbf{R})$, $V_{ee}(\mathbf{r})$ and $V_{NN}(\mathbf{R})$ are the potential energy terms for the electron-nucleus, electron-electron and nucleus-nucleus Coulombic interactions, respectively. These contributions to the energy of the system are expressed as a function of $\mathbf{r} = (\mathbf{r}_1, \mathbf{r}_2, \ldots, \mathbf{r}_i)$ and $\mathbf{R} = (\mathbf{R}_1, \mathbf{R}_2, \ldots, \mathbf{R}_k)$, electronic and nuclear coordinates, respectively.

To study the temporal evolution of the system would require solving the Schrödinger equation as a function of time:

$$i\hbar \frac{\partial \psi}{\partial t}(\mathbf{r},\mathbf{R},t) = \hat{H}\,\psi(\mathbf{r},\mathbf{R},t) \qquad 3)$$

where $\Psi(\mathbf{r}, \mathbf{R}, t)$ is the wave function that describes the properties of the system, which is dependent on time as well as on the spatial coordinates of electrons and nuclei. The resolution of this equation, also for a system with few atoms and subject to specific constraints for e.g. temperature, pressure and volume, is computationally very expensive, as it presents a very high number of solutions (self-functions) each one corresponding to one of energy states accessible to the system. For this reason, the

rigorous treatment with quantum-mechanical methods is not typically adopted in the field of Biophysics, where the size of the systems under investigation would make the calculation inaccessible with the current technology. This leads to the unavoidable application of some strong approximations.

Since the mass of the atomic nuclei is much greater than that of the electrons, the latter have velocities higher than that of the nuclei. We can therefore consider the electron system as being able to respond instantaneously to changes in the spatial configuration of the nuclei and therefore to remain in its fundamental state for each nuclear configuration. On the basis of this approximation, known as Born-Oppenheimer or adiabatic approximation, it is possible to consider the motion of the electrons as decoupled from that of the nuclei. A drastic simplification of the Schrödinger equation follows through the factoring of the respective eigenfunctions. A further simplification is possible, which is also introduced in the context of the adiabatic approximation, through the classical treatment of the motion of atomic nuclei according to a potential. This is calculated through the use of approximate empirical functions that implicitly take into account electronic effects.

The fundamental purpose of classical MD is therefore to use the potential energy of the system according to the nuclear positions in order to describe its motion and to be able to extrapolate the macroscopic quantities of interest.

MD is based in fact on Newton's second law of motion:

$$\mathbf{F} = m\,\mathbf{a} \qquad 4)$$

where **F** is the force, m is the mass of the particle and **a** is its acceleration. Such "classical" description (based on the laws of classical Physics) implies the definition of

the state of a system composed of N particles in a given instant t, as a function of the position and momentum of each particle constituting the system itself:

$$\mathbf{r}=(x_1, y_1, z_1, x_2, y_2, z_2, \ldots, x_N, y_N, z_N) \qquad 5)$$

$$\mathbf{p}=(p_{x,1}, p_{y,1}, p_{z,1}, p_{x,2}, p_{y,2}, p_{z,2}, \ldots, p_{x,N}, p_{y,N}, p_{z,N}) \quad . \qquad 6)$$

By taking into consideration the generic atom *i*,

$$\mathbf{F}_i=m_i\mathbf{a}_i \qquad \text{where } i=1, 2, 3, \ldots, N. \qquad 7)$$

If the force acting on each atom of the system under investigation at a given instant is known, it will be possible to calculate the corresponding acceleration. The system is therefore left free to evolve under the action of said forces for a certain period of time after which, due to the forces acting on them, the N particles will have changed position. Then, after each pre-set time interval (time-step), the system will be in a new configuration, the new forces will be calculated and the system will be allowed to evolve for a subsequent time interval, iteratively. In the MD, the forces are calculated on the basis of "classical" functions used to describe the different terms of the system's potential energy, whose parameters are typically obtained empirically and/or through accurate quantum-mechanical calculations. In practice, depending on the current system configuration, a set of appropriately parameterized functions allow the calculation of the different contributions to the total potential energy *V* of the system, which describes the interaction energy between the particles in that particular configuration. The

complete set of these functions and parameters constitutes the so-called force-field (paragraph 2.3).

The force **F** can be expressed as the gradient of the potential energy *V*

$$\mathbf{F}_i = -\nabla_i V(\mathbf{r}_1, \mathbf{r}_2, \ldots, \mathbf{r}_N) = -\left(\frac{\partial V}{\partial x_i}, \frac{\partial V}{\partial y_i}, \frac{\partial V}{\partial z_i}\right) \qquad 9)$$

from which it is derived:

$$\mathbf{F}_i = -\nabla_i V(\mathbf{r}_1, \mathbf{r}_2, \ldots, \mathbf{r}_N) = m_i \mathbf{a}_i = m_i \frac{d^2 \mathbf{r}_i}{dt^2} \qquad 10)$$

ultimately, through the integration of the discretized equations of motion it is possible to derive the trajectory followed by the particles, i.e. their positions as a function of time:

$$r(t_1) = r(t_0) + \int_{t_0}^{t_1} \frac{p(t)}{m} dt \qquad \text{where} \quad v = \frac{p}{m} \quad . \qquad 11)$$

Similarly, the expression for the linear moment is derived:

$$p(t_1) = p(t_0) + \int_{t_0}^{t_1} a(t)\, dt \quad . \qquad 12)$$

In order to start a MD simulation, in addition to an appropriate force-field, a set of initial coordinates is necessary for all the atoms of the system to be simulated. These are typically obtained from the molecular structures determined experimentally by X-ray

crystallography and / or NMR spectroscopy. Furthermore, initial velocities have to be assigned to the atoms. These are usually calculated on the basis of the Maxwell-Boltzmann distribution at the desired temperature and then arbitrarily assigned (randomly) to the atoms that compose the system.

2.1.1 Ergodic Hypothesis

A system at the equilibrium in a given thermodynamic state is defined by variables corresponding to specific state functions such as pressure, temperature, number of particles and volume. Statistical mechanics describes the correlation between these macroscopic thermodynamic quantities and the microscopic properties of the system, ie the properties of the constituent particles. A system at equilibrium can be described as the average of N independent microstates. Each microstate represents a particular configuration of the system, which is different from that of all the other microstates but compatible with the macroscopic variables that describe the system in that specific thermodynamic state. A given macroscopic observable G will therefore be equal to the expectation value, $\langle G \rangle$, calculated as average from the set of values obtained for each of the N microstates. In fact, the MD generates a trajectory of the system under investigation and allows monitoring the variation of certain physical quantities as a function of time by recording the system configuration (microscopic state) at given time intervals. At the end of a simulation, it will be possible to obtain the macroscopic quantities by calculating the time average of the observable of interest with respect to the N configurations recorded along the trajectory. Practically, we assume the equality between the calculated average with respect to the microstates of the system identified

by the preservation of certain values assumed by prefixed state functions, $\langle G \rangle$, and the mean of the values obtained for the system under the same conditions during its time evolution, $\langle G \rangle_{Nt}$. This assumption takes the name of *ergodic hypothesis*

$$\lim_{N \to \infty} \langle G \rangle_{N_t} = \langle G \rangle \quad . \qquad 13)$$

If the simulation time is sufficiently long the number of sampled microstates is such that the ergodic hypothesis is satisfied.

The algorithms typically used for MD allow simulating the system by keeping certain macroscopic quantities constant. The set of constant imposed variables during the simulation takes the name of 'statistical ensemble'. The most commonly employed are:

- microcanonic ensemble or NVE: number of particles N, volume V and energy E constants;
- canonical ensemble or NVT: number of particles N, volume V and temperature T constant;
- isothermal-isobaric or NPT ensemble: number of particles N, pressure P and temperature T constant;
- grancanonic ensemble or μVT: constant chemical potential μ, volume V and temperature T.

In this work we worked mainly with the NVT ensemble.

2.2 Enhancing Sampling: Metadynamics

Classical MD simulations present a inherent problem related to the time scale: it may take an extremely long simulation time to observe events whose time scale is known from the experiments to be on the order of milliseconds, like most biological processes. These events, on the time scale accessible to standard classical MD simulation are classified as rare events. The choice of the sampling technique employed to simulate rare events has a fundamental importance especially in systems in which the ergodicity is questioned by the complexity of the hypersurface describing the potential of the system itself.

Metadynamics (METAD) is a powerful technique for enhanced sampling, allowing to sample rare events with quasi-equilibrium molecular dynamics simulations. [12] Further, it allows to reconstruct the free-energy surface as a function of few collective variables (CVs). An external history-dependent bias potential, as function of CVs, added to the Hamiltonian of the system during an MD simulation, allows accelerating sampling in METAD. This potential is written as a sum of Gaussian functions deposited along the system trajectory in the CVs space. Thus, to visit the already sampled configurations more than once is hindered. [15], [16]

Let us consider S as a set of n functions of microscopic coordinates $\boldsymbol{R}$ of the system:

$$S(\boldsymbol{R}) = (S_1(\boldsymbol{R}), \ldots, S_n(\boldsymbol{R})) \quad . \qquad 14)$$

At the time t, the bias potential is:

$$V_G(S,t)=\int_0^t dt'\,\omega\exp\left(-\sum_{i=1}^{d}\frac{\left(S_i(\boldsymbol{R})-S_i(\boldsymbol{R}(t'))\right)^2}{2\,\sigma_i^2}\right) \qquad 15)$$

where ω is an energy rate and σ_i is the width of the Gaussian for the ith CV. The energy rate is constant and it is expressed in terms of a Gaussian height w and Gaussian deposition stride τ_G:

$$\omega=\frac{w}{\tau_G} \quad . \qquad 16)$$

If the system is in the local minimum A, see figure 2.1, in a standard MD simulation, the system is not able to overcome energy barriers much larger than thermal fluctuations, or the probability is extremely low. The Gaussian functions added after a given time t modify the underlying free energy surface of the system and allow it to cross the energy barrier and to pass into a new local minimum more easily.

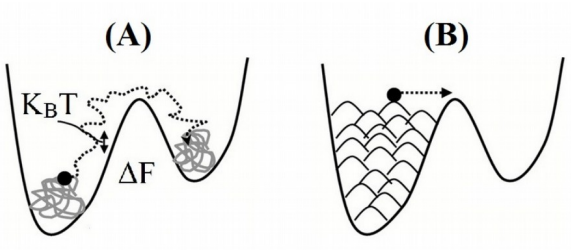

Fig. 2.1: Schematic scheme of the biased potential used in Metadynamics method. A system may require free energy jumps much greater than the average fluctuations in energy at a given temperature (A); In Metadynamics [17, 18, 19] , a history-dependent potential is added discouraging the system from visiting already explored conformations (B). Reprinted from [17]

Metadynamics has some benefits represented by the acceleration of sampling. At variance with umbrella sampling, metadynamics inherently explores the low free-energy regions first. Eventually, the bias potential V_G provides an unbiased estimate of the underlying free energy, under the assumption that in the absence of bias, the stochastic dynamics in the CVs space is memoryless

$$V_G(S, t \to \infty) = -F(S) + C \qquad 17)$$

where C is an irrelevant additional constant and the free energy is defined as:

$$F(S) = -\frac{1}{\beta} \ln\left(\int d\boldsymbol{R}\, \delta(S - S(\boldsymbol{R}))\, \mathrm{e}^{-\beta U(\boldsymbol{R})} \right) \qquad 18)$$

here $\beta=(k_BT)^{-1}$, k_B is the Boltzmann constant, T the temperature of the system and $U(\boldsymbol{R})$ the potential energy function.

Under the above assumption, the error on the reconstructed FES has been proven, both empirically and theoretically, [15], to be:

$$\epsilon \propto \sqrt{\frac{\omega}{D\beta}} \qquad 19)$$

where D is the intrinsic diffusion coefficient in the CVs space. The error in the FES is often estimated by comparison of indipendent runs or block averaging.

Metadynamics simulations are intrinsically parallelizable. Indeed, multiple interacting metadynamics simulations can be performed for exploring and reconstructing the same FES. Each simulation contributes to the overall history-dependent potential. This

implementation, called *Multiple Walkers Metadynamics* [18], leads to a fully linear scaling algorithm that does not need fast and expensive connection between CPUs.

Metadynamics presents two major drawbacks. First of all, in a single run, V_G oscillates around an energy constant value and the potential energy does not converge. At this point, the bias potential overfills the underlying FES and pushes the system toward high-energy regions of the CVs space. Thus, to decide when to stop one simulation is not trivial, especially if the goal is the reconstruction of the FES. To this aim, simulations should be stopped when the motion of the CVs becomes diffusive in the region of interest. The second problem is to identify a proper set of CVs that describe the complex process under investigation.

A solution to the first problem is provided by *Well-tempered metadynamics* (WT-METAD). [19] This is a technique where bias deposition rate decreases over simulation time. This is possible by using the following expression for the history-dependent potential:

$$V(S,t)=k_B\Delta T\ln\left(1+\frac{\omega N(S,t)}{k_B\Delta T}\right) \qquad 20)$$

$$\dot{V}(S,t)=\frac{\omega\delta_{s,s(t)}}{1+\frac{\omega N(S,t)}{k_B\Delta T}}=\omega e^{\frac{-V(S,t)}{k_B\Delta T}}\delta_{S,S(t)} \qquad 21)$$

where $\dot{V}(S,t)$ is the time derivative of the bias potential, $N(S,t)$ is the histogram of the S variables sampled during the simulation, and ΔT is an input parameter with the dimension of a temperature. Replacing $\delta_{S,\,S(t)}$ with a Gaussian, this formulation can be

easily reconnected to standard metadynamics. This set of equations is implemented by rescaling the Gaussian height *w* according to

$$w = \omega \tau_G e^{\frac{V_G(S,t)}{k_B \Delta T}} \qquad 22)$$

Since the histogram $N(S, t)$ grows linearly with simulation time, the rate $\dot{V}(S,t)$ tends to zero as 1/t and the dynamics of all the microscopic variables becomes progressively closer to thermodynamic equilibrium as the simulation proceeds. This is the way to have a rate decrease fast enough for the bias to converge and slow enough for the final result not to depend on the initial condition $V(S,0)$. Moreover, $\dot{V}$ is not uniform in the S space since at a given point, the rate is inversely proportional to the time spent there.

For larger times, $V(S,t)$ varies slowly and the ***R***'s could reach equilibrium, the probability distribution reads

$$P(S,t) \propto e^{-\frac{F(S)-V(S,t)}{k_B(T)}} \qquad 23)$$

and

$$\dot{V}(S,t) = \omega e^{\frac{-V(S,t)}{k_B \Delta T}} P(S,t) = \omega e^{\frac{-V(S,t)}{k_B \Delta T}} \frac{e^{-(F(S)+V(S,t))/T}}{\int dS e^{-(F(S)+V(S,t))/T}} \quad . \qquad 24)$$

This implies an important aspect: the bias potential does not fully compensate the FES, but it converges to

$$V_G(S,t\to\infty)=-\frac{\Delta T}{T+\Delta T}F(S)+C \qquad 25)$$

where C is an immaterial constant. At variance with standard metadynamics, the bias converges to its limiting value in a single run. In the long time limit, the CVs probability distribution becomes

$$P(S,t\to\infty)\propto e^{-\frac{F(S)}{k_B(T+\Delta T)}} \quad . \qquad 26)$$

Using the Eq. 20, the FES can be estimated as

$$\widetilde{F}(S,t)=-\frac{T+\Delta T}{\Delta T}V(S,t)=-(T+\Delta T)\ln\left(1+\frac{\omega N(S,t)}{\Delta T}\right) \quad . \qquad 27)$$

Therefore, for $\Delta T\to 0$, the bias is equal to zero, the Eq. 27 reduces to Eq. 18 so, classical MD is recovered. Whereas in the case of $\Delta T\to\infty$ limit, the deposition rate is constant, from Eq. 27 $\widetilde{F}(S,t)=-V(S,t)$ is found and the standard metadynamics algorithm is recovered. If $\Delta T\to\infty$, the convergence of $V(S,t)$ for $t\to\infty$ cannot be demonstrated using Eq. 24 because of the drawback of metadynamics mentioned above. In intermediate cases, the calculated FES is related to a target temperature T and the tranverse degree of freedom are correctly sampled. However, the S probability distribution is altered corresponding to an temperature $T+\Delta T$ without having to assume adiabatic separation between S and the other variables. [58]

The value of ΔT can be regulated in order to increase the barrier crossing and extent CVs space exploration. Moreover, using a finite value of ΔT the exploration of FES is

confined to a region with energy range of the order $T+\Delta T$ so, the sampling can be limited to the physically interesting regions of S. This method avoids overfilling and might save computational time when a large number of CVs are used.

The Eq. 26 shows that the probability distribution for the CVs can be easily reconstructed but the probability of others degrees of freedom is distorted in a nontrivial way by the introduction of a history-dependent potential.

Reweighting a metadynamics run is important in order to recover the unbiased distribution for variables different than CVs. [40] For this purpose, different techniques have been proposed. Recently, a reweighting scheme [39] in the framework of WT-METAD has been introduced.

If the system can be considered to be in instantaneous equilibrium under the action of internal potential $U(\boldsymbol{R})$ and the bias $V_G(S(\boldsymbol{R}),t)$ at any time the probability distribution in the bias ensemble is related with the canonical Boltzmann distribution:

$$P(\boldsymbol{R},t)=e^{-\beta(V_G(S(\boldsymbol{R}),t)+c(t))}P_B(\boldsymbol{R}) \qquad 28)$$

where $P_B(\boldsymbol{R})=e^{-\beta(U(\boldsymbol{R}))}/Z$ is the Boltzmann distribution and Z the canonical partition function. In the Eq. 28 appears the time-dependent bias offset defined as

$$c(t)=-\frac{1}{\beta}\log\left(\frac{\int dS\, e^{-\beta F(S)}}{\int dS\, e^{-(F(S)+V_G(S,t))}}\right) \quad . \qquad 29)$$

From Eq. 28, to determine the expression of the biased distribution at $t+\Delta t$ is possible:

$$P(\boldsymbol{R},t+\Delta t)=e^{-\beta(\dot{V}_G(S(\boldsymbol{R}),t)+\dot{c}(t))\Delta T}P_B(\boldsymbol{R},t) \quad . \qquad 30)$$

The Eq. 30 assumes adiabatic evolution for the bias potential and in the case of WT-METAD, this become valid as the simulation progresses. Moreover, being

$$\dot{c}(t) = -\int dS \dot{V}_G(S,t) P(S,t) = -\langle \dot{V}_G(S,t) \rangle \qquad 31)$$

it is possible to obtain the evolution of the biased probability during the metadynamics simulation

$$P(\boldsymbol{R}, t+\Delta t) = e^{-\beta(\dot{V}_G(S(\boldsymbol{R}),t) - \langle \dot{V}_G(S,t) \rangle)\Delta t} P(\boldsymbol{R}, t) \quad , \qquad 32)$$

where the average in the exponent is calculated in the biased ensemble.

This technique allows computing expectation values of any variable. Therefore, to use CVs directly related to measurable quantities and thus obtaining a direct comparison with experiments is not necessarily needed.

More precisely, a CV is a function of the microscopic coordinates of the system. To guarantee an effective application of metadynamics they must respect some guidelines. First of all, the CVs should distinguish between the initial and final state and describe all the relevant intermediates. When the potential energy function is projected on a FES, a dimensional reduction has been dispached. To be dynamically meaningful, i.e., to correspond to the reaction coordinate, CVs must respond to stricter conditions.

The second essential prerequisite is that CVs should include all the slow modes of the system. This second prerequisite is essential. Those variables that cannot be satisfactorily sampled in the timescale of the simulation are defined ‘slow’. These variables must be added to the CVs list otherwise the bias potential may not converge to the FES in a reasonable simulation time. The last prerequisite provides for the small

number of CVs in order to avoid exploration of a high-dimensional space, which would increase computational time and would make the analysis of the resulting free energy surface difficult.

The question is how choose a set of CVs to describe the process under investigation. The development of appropriate CVs and the combination of metadynamics with methods that enhance the sampling of transverse coordinates are the two general approaches. The choice of CVs depends on the nature of the specific process studied. Examples of commonly used CVs can be represented by interatomic distances, angles, dihedrals, coordination numbers, radius of gyration, dipole moment, number of hydrogen bonds, beside some "home made" CVs implemented in the algorithm when a specific reaction coordinate is required to study a specific system. Few CVs have shown the potential to be used in a wide number of cases and a really general choice is to use the potential energy of the system as a metadynamics CV. Using potential energy as a CV within well-tempered metadynamics results in the sampling of a well-defined distribution called well-tempered ensemble (WTE). [41] In this ensemble, the average energy is very close to its canonical value but the fluctuations are enhanced in a tunable way, thus improving sampling. Other approaches rely on the identification of the most relevant degrees of freedom by means of standard dynamics and a principal component analysis.

Sometimes finding a small set of CVs is a daunting task. For example, in the case of protein folding, which takes place in a large and complex conformational space and often involves many alternative pathways. In order to study such processes, it is fundamental to enhance sampling along a great number of degrees of freedom besides those that can be targeted by metadynamics. A successful strategy is to combine metadynamics with a *replica exchange method* (REM) [20] such as the *parallel*

tempering algorithm (PT). [21] In PT, multiple copies of the same system at different temperatures are independently simulated. At fixed intervals, an exchange of configurations between two adjacent replicas is attempted. By exchanging with higher temperatures, colder replicas are prevented from being trapped in local minima.

Considering M independent replicas of the system at different temperatures $T1$, ..., T_M. The acceptance probability for the exchange between configuration $\boldsymbol{R}_j$ at temperature T_j and configuration $\boldsymbol{R}_k$ at temperature T_k is the following:

$$p(j \to k) = min\left[1, e^{\Delta_{j,k}}\right] \qquad 33)$$

where $$\Delta_{j,k} = (\beta_i - \beta_k)(U(\boldsymbol{R}_j) - U(\boldsymbol{R}_k)) \qquad 34)$$

When PT is combined with metadynamics, each replica at a different temperature performs a metadynamics that uses the same set of CVs. Indicating with $V_G^{(i)}$ the bias potential acting on the ith replica, the acceptance probability is determined by

$$\begin{aligned}\Delta_{j,k} = &(\beta_i - \beta_k)(U(\boldsymbol{R}_j) - U(\boldsymbol{R}_k)) \\ &+ \beta_j\left[V_G^{(j)}(S(\boldsymbol{R}_j), t) - V_G^{(j)}(S(\boldsymbol{R}_k), t)\right] \\ &+ \beta_k\left[V_G^{(k)}(S(\boldsymbol{R}_k), t) - V_G^{(k)}(S(\boldsymbol{R}_j), t)\right]\end{aligned} \qquad 35)$$

This combination of PT and metadynamics (PT-MetaD) is particularly effective because it compensates for some of the weaknesses of each method. While PT allows the system to cross moderately high free-energy barriers on all degrees of freedom, the effect of neglecting a slow degree of freedom in the CVs plays a less important role and the metadynamics bias potential allows higher barriers on a few selected CVs to be

overcome. One limitation of PT-MetaD approach is the poor scaling with system size. In fact, a sufficient overlap between the potential energy distributions of neighboring replicas is required in order to obtain a significant diffusion in temperature space. Thus, as in standard PT, the number of replicas needed to cover the same temperature range scales as the square root of the number of degrees of freedom, making this approach prohibitively expensive for large systems. In order to overcome these problems, different combinations between metadynamics with other type of REM have been proposed. In *solute tempering*, the parts of the Hamiltonian describing the solute-solvent and solvent-solvent interactions are rescaled across the replicas in such a way that the number of replicas needed scales as the square root of the number of solute degrees of freedom. In PT-WTE, the energy fluctuations can be enhanced in order to guarantee an effective overlap of the energy distributions between neighboring replicas. Moreover, the quantity $\Delta_{j,k}$, that in standard PT determines the swapping probability, is reduced by a tunable parameter, leading to an effective diffusion in the temperature space.

An alternative approach is the bias exchange metadynamics (BE-METAD) [22, 23], where a replica exchange scheme is implemented among N non-interacting replicas of the system, all at the same inverse temperature β and each biased by a different set of collective variable $S^{\alpha}(x)$ with α=1, ..., N. One of benefits is represented of the exchange modality that is not between two adjacent replicas only. Each different replica independently accumulates a history-dependent potential $V_G^{\alpha}(x,t)=V_G(S^{\alpha}(x),t)$ that, after a sufficiently long time, would provide an estimate of the FES as a function of S^{α}. If all the variables are relevant for the process, the convergence of each free energy profile can be extremely slow and hindered by hysteresis.

This method allows the replicas to exchange their configurations. Two replicas *a* and *b* are randomly selected from the N of the system. The exchange move consists of swapping the atomic coordinates x^a and x^b of the two replicas. The two replicas are evolved under the action of two different history-dependent potentials and the probability t accept the move is

$$p_{ab}=min\left(1,\exp\{\beta[V_G^a(x^a,t)+V_G^b(x^b,t)+V_G^a(x^b,t)+V_G^b(x^a,t)]]\}\right) \quad 36)$$

If the move is accepted, the collective variables of replica *a* perform a jump from $S^a(x^a)$ to $S^a(x^b)$, and replica *b* from $S^b(x^b)$ to $S^b(x^a)$. The exchange moves are not introduced for ensuring convergence to any distribution but to increase the capability of each replica to diffuse in the CV space in order to obtain the accuracy of the free energy reconstruction. If each bias is defined in a few CVs at a time, after some accepted exchanges, each configuration is able to explore the space spanned by all the collective variables. This improves the capability of the system to explore the configuration space because on each replica we work on small dimensional space of CVs, thus the sampling is more efficient than with a high number of CVs.

2.3 Force Field

A force fields (ff), from a Molecular Mechanics (MM) point of view, is a set of parameters used to express the potential energy of a system of particles.

Molecular mechanics (MM) and force fields (ff) are based on the Born-Oppenheimer approximation, which asserts the separation of nuclear and electronic motions and therefore the energy of a system can be expressed as a function of the nuclear coordinates only. In ffs, the potential energy of the system is described as a sum of different terms describing bond stretching, angle bending, dihedral angles torsions and nonbonded terms like the electrostatic interactions (Coulomb force) and dispersion interactions and repulsion (van der Waals forces). Functions could be applied to describe a number of similar chemical groups in a molecule.

MM ffs are empirical: the separation of the potential energy in terms with a classic physical interpretation is not strictly correct, as there is no unique way to "translate" quantum mechanical effects into classical mechanics equations.

As mentioned, potential energy models are described by two macro-components: bonded interactions and non-bonded interactions. In case of bonded interactions, the potential energy describing atomic bonds are commonly modelled with harmonic potential functions from classical mechanics:

$$V_{bond} = \frac{1}{2} k_r \left(r_{ij} - r_{ij}^0 \right)^2 \qquad 37)$$

$$V_{angle} = \frac{1}{2} k_\theta \left(\theta_{ijk} - \theta_{ijk}^0 \right)^2 \qquad 38)$$

where r^0_{ij} is the equilibrium distance, θ^0_{ijk} is the equilibrium angle, and k_r and k_θ are the force constants.

Not all MM ffs use torsional potentials; it may be possible to rely upon non-bonded interaction between the atom at the end of each torsion angle (the 1, 4 atoms) to achieve the desired energy profile. However, most force field for organic molecules do use explicit torsional potentials with a contribution from each bonded quartet of atoms A-B-C-D in the system. Torsional potentials are almost always expressed as a cosine series expansion:

$$V_{dihedral} = \sum_{n=0}^{N} \frac{k_\phi}{2} [1 + \cos(n\phi_{ijkl} - \phi^0_{ijkl})] \qquad 39)$$

in which k_φ is referred to the barrier height, the φ^0 is the fase factor and determine where the torsion angle passes its minimum value. For convention φ is the angle between the *ijk* and *jkl* planes as shown in figure 2.1.

It is necessary to incorporate additional terms in order to achieve the desired geometry when three atoms have to be kept in the same plane. A common way to achieve this is to use an out-of-plane bending term. This term can be treated as an improper torsion angle. Also this potential can be described by an harmonic function among four atoms (i, j, k and l) as reported:

$$V_{improper} = k_\omega (1 - \cos 2\omega_{ijkl}) \qquad 40)$$

where k_ω is the harmonic constant and ω_{ijkl} is the equilibrium improper angle.

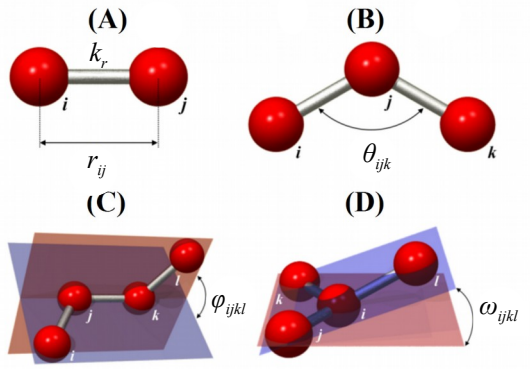

Fig. 2.1: Types of interactions between bonded atoms. (A) bond stretch, (B) bond torsion, (C) proper dihedral and (D) improper dihedral. Reprinted from [57].

The non-bonded interactions term encloses all the interactions between atoms that are not directly linked via chemical bonds, therefore repulsion, dispersion and electrostatics. Lennard-Jones functions, Eq. 41, describe the Van der Waals interaction (repulsion and dispersion). The Lennard-Jones potential between the atoms *i* and *j*, at distance r_{ij} is:

$$V_{LJ} = 4\epsilon_{ij}\left[\left(\frac{\sigma_{ij}}{r_{ij}}\right)^{12} - \left(\frac{\sigma_{ij}}{r_{ij}}\right)^{6}\right] \qquad 41)$$

where ε_{ij} is the depth of the potential well, σ_{ij} is the distance relative to the minimum potential and r_{ij} is the distance between atoms considered. Point charges fixed on the nuclei are used to describe the electrostatic potential. The electrostatic interactions between two molecules (or between different parts of the same molecule) is then calculated as a sum of interactions between pairs of point charges, using Coulomb's law:

$$V_c = \sum_{i=1}^{N_A} \sum_{j=1}^{N_B} \frac{q_i q_j}{4 \pi \epsilon_0 r_{ij}} \qquad 42)$$

where N_A and N_B are the number of point charges, ε_0 is the vacuum dielectric constant, q_i and q_j are respectively the charge of the *i*-th and *j*-the atoms and r_{ij} the distance between the two atoms *i* and *j*.

In Fig. covalent-bond stretching, angle bending, proper and improper dihedral angles are represented.

An external contribution to the potential energy is the restraint term required in some simulations to impose restraints on the time evolution of the system.

Therefore, in general the expression used for the potential energy of molecular systems, like simple organic molecules and biological macromolecules is:

$$\begin{aligned} V_{tot} = & \sum_{bond} \frac{k_r}{2} (r_{ij} - r_{ij}^0)^2 + \sum_{angle} \frac{k_\theta}{2} (\theta_{ij} - \theta_{ij}^0)^2 \\ & + \sum_{dihedrals} \frac{k_\phi}{2} [1 + \cos(n \phi_{ijkl} - \phi_{ijkl}^0)] + \sum_{improper} k_\omega (1 - \cos 2 \omega_{ijkl}) \\ & + \sum_{i=1}^{N_A} \sum_{j=i+1}^{N_B} \left\{ 4 \epsilon_{ij} \left[\left(\frac{\sigma_{ij}}{r_{ij}} \right)^{12} - \left(\frac{\sigma_{ij}}{r_{ij}} \right)^{6} \right] + \frac{q_i q_j}{4 \pi \epsilon_0 r_{ij}} \right\} \end{aligned} \qquad 43)$$

It has to be noted that there is not explicit term for hydrogen bonding. In all the most common force fields, biologically important hydrogen bonds are handled by the combination of the LJ and the Coulomb terms. Most ffs only include interaction sites for bonded and non-bonded interactions at the location of the atomic nuclei. This model is generally very accurate to reproduce hydrogen bond energies and geometries, although it can lead to deviations from QM results with respect to the angular

dependence of hydrogen bonding energy. The most popular force-fields for molecular dynamics simulations of proteins are AMBER, GROMOS, CHARMM and OPLS-AA. [24, 25, 26, 27] In this work Amber ff has been used. Amber uses computed QM electrostatic potential surfaces as the target data for partial charge determination. Thus, Amber partial charges aim to reproduce molecules' gas-phase electrostatic potentials.

In the particular case of biological systems, water, of course, plays a key role. Many of the concepts considered so far are used to examine the empirical models that have been developed and proposed in the literature to describe water that, nevertheless, represents one of the most challenging systems to be accurately modelled. Water models can be divided into three types. In the simple interaction-site models, each water molecule has a rigid geometry and their interactions are described using Coulombic and Lennard-Jones expressions. Flexible models allow conformational changes. The polarization and many-body effects have been also included into more sophisticated models. The simple water models use three or five interaction sites and a rigid water geometry. The TIP3P and SPC models use a total of three sites for the electrostatic interactions; the partial positive charges on hydrogen atoms are exactly balanced by an appropriate negative charge locate on the oxygen atom. The van der Waals interaction between two water molecules is computed using a Lennard-Jones function with a single interaction point per molecule centered on the oxygen atom; no van der Waals interactions involving the hydrogen atoms are calculated. The parameterization is usually done by calculating properties through MD or MC simulations. The most popular models are TIP3P, SPC, SPC/E, BF, TIP4P. [29] - [33] In this work TIP3P has been adopted to reach the desired accuracy but avoiding more computationally expensive flexible and polarizable models.

2.4 Energy Minimization

The preliminary phase consists in the minimization of the energy for which the algorithm known as steepest descent has been used, with an initial step-size h_0 of 0.01 nm. After defining the position vector **r** of the $3N$ coordinates, the force **F** acting on each particle is calculated as the negative gradient of the potential energy V. The new positions are then obtained according to

$$\mathbf{r}_{n+1} = \mathbf{r}_n + \frac{\mathbf{F}_n}{max(|\mathbf{F}_n|)} h_n \qquad 41)$$

where, h_n represents the maximum displacement, $\mathbf{F}_n$ is the force and max($|\mathbf{F}_n|$) represents the largest of the absolute values of the force components. The new potential, and therefore the new forces, are calculated for the new positions. If $V_n + 1 < V_n$ the new positions are accepted and $h_n + 1 = 1.2h_n$. If instead $V_n + 1 \geq V_n$ the new positions are rejected and $h_n = 0.2h_n$. The minimization is interrupted when it comes to convergence, i.e. when the value of max($|\mathbf{F}_n|$) is less than 10.0 $kJmol^{-1}nm^{-1}$, or when 1000 steps of minimization are performed.

2.5 Algorithm (Brief Overview)

The computational cost increases with the size of the system, i.e. the number of particles and parameters involved. Clearly, the simulation 'box' must be kept as small as possible. The simple fact, however, to define a 'box' implies that our simulation will suffer from artifacts due to the limited size of the simulated system. For all those particles that are sufficiently close to the boundaries of the 'box', all the energy contributions will not be calculated correctly, since beyond the boundary there is nothing. Furthermore, it may happen that some molecules or part of molecules tend to move out of the 'box' during the simulation. The typical way to circumvent these problems is the application of the so-called periodic boundary conditions (PBC). In practice, the simulation box is treated as the unitary cell of a crystalline system, which should be flanked by an exact copy on each side of the box. These copies are called 'images'. During the simulation, only the properties of the 'box' are calculated, recorded and propagated, exploiting the images only for the atoms otherwise missing their neighboring molecules in the radius of interest. When a particle crosses one side of the 'box', it reappears on the opposite side with the same speed. The PBC method allows also to calculate precisely the electrostatic contribution at long range, via the Ewald sum and some related algorithm.

The non-bonded interactions like electrostatic interactions have been calculated by Particle Mesh Ewald algorithm. [15] In the Ewald summation the interaction potential is separated into two terms:

$$V(\mathbf{r}) = V_{sr}(\mathbf{r}) + V_{lr}(\mathbf{r}) \qquad 44)$$

where $V_{sr}(\mathbf{r})$ represents short range interactions whose sum quickly converges in real space and $V_{lr}(\mathbf{r})$ represents long range interactions whose sum quickly converges in Fourier (reciprocal) space. The particle mesh Ewald summation replaces the direct summation of interaction energies between point particles:

$$E_{tot} = \sum_{i,j} V(\mathbf{r}_j - \mathbf{r}_i) = E_{sr} + E_{lr} \qquad 45)$$

where $E_{sr} = \sum_{i,j} V_{sr}(\mathbf{r}_j - \mathbf{r}_i)$ is the short-ranged potential in real space (particle part) and $E_{lr} = \sum_{\mathbf{k}} \widetilde{V}_{lr}(\mathbf{k}) |\widetilde{\rho}(\mathbf{k})|^2$ is a summation in Fourier space of the long-ranged part. Here $\tilde{V}_{lr}(\mathbf{k})$ and $\widetilde{\rho}(\mathbf{k})$ represent respectively the Fourier transforms of the potential and the charge density (Ewald part). Since both summations converge quickly in their respective spaces, they may be truncated with little loss of accuracy and great improvement in required computational time.

During the first equilibration step, using the NAMD software, the pressure was kept constant with the *Berendsen Algorithm*. [16] The Berendsen barostat adds an extra term to the equations of motion which affects the pressure change:

$$\left(\frac{dP}{dt}\right)_{bath} = \frac{P_0 - P}{\tau_P} \qquad 46)$$

where P_0 is the reference pressure, i.e. the pressure of the external pressure "bath", and P is the instantaneous pressure. τ_P is a time constant. Within this scheme, box sizes are rescaled at every step. Assuming the system is isotropic and within a cubic box the scaling factor is given by

$$\mu = 1 - \frac{\beta \Delta t}{3 \tau_P}(P_0 - P) \qquad 47)$$

where β is the isothermal compressibility.

After equilibration, the production run has been performed in NVT ensemble.

The ACEMD software uses the *Velocity Verlet* algorithm [14]] to integrate the equations of motion, which allows to explicitly change positions and speeds:

$$\mathbf{r}_i(t+\delta t) = \mathbf{r}_i(t)\mathbf{v}_i(t)\delta t\left(\delta t^2 \frac{\mathbf{F}_i(t)}{2m_i}\right) \qquad 48)$$

$$\mathbf{v}_i(t+\delta t) = \mathbf{v}_i(t) + \delta t^2\left(\frac{\mathbf{F}_i(t) + \mathbf{F}_i(t+\delta t)}{2m_i}\right) \qquad 49)$$

Since they are a way of directly getting the position and velocity at the end of the time step from the position and velocity of previous steps, they provide an easy way of grafting stochastic collisions into the algorithm. The effect of a stochastic collision is merely to change the value of $v_i(t)$ just before $r_i(t+dt)$ is calculated.

The temperature (T) was kept constant during the simulation by using the *Langevin thermostat* [14] which mimics the coupling of the system of interest to an external thermal bath. Here the Newton's equations of motion are modified by:

$$\dot{r_i} = v_i = \frac{p_i}{m_i} \qquad 50)$$

$$\dot{p}_i = \mathbf{F}_i - \zeta_i \mathbf{p}_i + \sigma \dot{\mathbf{f}}_i \qquad 51)$$

where $\zeta = \frac{k_B T}{D}$ *52)*

where $\mathbf{F}_i$ is the force acting on the atom i due to the interaction potential, ζ_i is a friction coefficient, related to diffusion coefficient D, and $\dot{\mathbf{f}}_i$ is a 'random force' with the coefficient σ_i that governs the strength of the random force, related to the friction coefficient ζ_i through *fluctuation-dissipation theorem*:

$$\sigma = \sqrt{2 \zeta_i K_B T} \qquad 53)$$

Langevin dynamics is identical to classical Hamiltonian in the limit of vanishing γ_i.

2.6 Computational Details: Molecular Dynamics Simulations

We started from the OmpF structure (PDB ID: 2OMF; 2.4Å resolution) previously simulated. [3] The system was simulated at neutral pH with all amino acid residues in their charged state but the residue E296, which was protonated. [43] The OmpF trimer was embedded in a pre-equilibrated POPC (1 palmitoyl-2-oleoyl-sn-glycero-3-phosphocholine) bilayer of 259 lipids. The system was oriented in order to center the protein at the origin of the coordinate system and align the channel diffusion axis along the z axis, hence z positive values refers to the extracellular vestibule (EV) and z negative values refers to the periplasmic vestibule (PV). Using the NAMD software [36], the system was equilibrated in the gas-phase in order to force lipids to adhere the hydrophobic regions of the porins. After 1 ps of energy minimization (*conjugate gradients*) a slow heating from 10 K to 300 K in NPT ensemble was performed. The system was solvated with ~17000 water molecules and the total number of atoms was ~100k in a box with size 11x11x9 nm (Fig. 2.2). A suitable number of potassium and chloride ions were added to have a concentration of 0.2 M KCl. An excess of K^+ was required to neutralize the total negative charge of the trimer (-33 e).

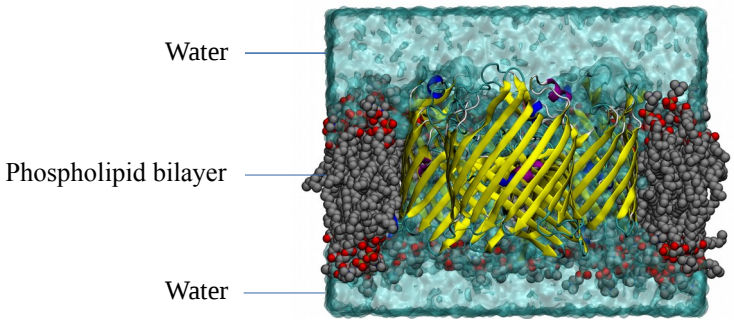

Fig. 2.2: OmpF (yellow structure) solvated system section.

After 1 ps of energy minimization (*conjugate gradients*), a slow heating from 10 to 300 K was carried out for 1 ns with positional restraints on the Cα protein along three dimensions and on the lipids phosphorus atoms along z only, allowing movement on xy plane. After releasing the constraints, an equilibration stage of 4 ns in the NPT ensemble at 1.0 bar and 300 K was performed. Finally, 400 ns MD simulations were performed in the NVT ensemble without restraints. Only the last 300 ns were used for the analysis. Production run in the NVT ensemble was performed using the ACEMD code [37] compiled for GPUs, with a tome step of 4fs. The Langevin thermostat (300 K) was used with 0.1 ps damping time and the particle mesh Ewald (PME) [34] method with 9 Å cut-off for electrostatic interactions. The Amber99sb-ildn force field [44] parameters were used for OmpF, the General Amber Force Field (GAFFlipid) for POPC, and the TIP3P [29] model for waters. The same procedure was carried out for all the orthologues under study in order to compare their physico-chemical feature (paragraph 3.1). In table 2.1 are reported which residue has been protonated, for analogy with OmpF, and the relative value of pKa found using the PROPKA server [45], fixing the pH at a neutral value.

Tab. 2.1: Protonated residues based on pKa values.

protein	**residue**	**pKa**
OmpF	E 296	10.04
OmpC	D 299	9.58
Omp35	E 102	11.33
Omp36	D 307	9.66
OmpK35	E 102	Analogy with OmpF
OmpK36	D 297	9.97
OmpE35	D 235	Analogy with OmpF
OmpE36	D 295	Analogy with OmpC

For all the known-substrate under investigation, the Gaff-force field parameters were obtained from http://www.dsf.unica.it/~gmalloci/abdb/. [46] For the molecules that were not available in the antimicrobial database of the group, we used the Marvin Chemaxon suite [47] to draw the molecule and find the most populated protonation/charge states at physiological pH=7.4. We used the Gaussian09 package [48, 49] to perform ground-state geometry optimization of the main tautomer in implicit solvent (Polarizable Continuum Model, solvent=water), by applying the *Density Functional Theory* (DFT). [50] We used the hybrid exchange-correlation functional B3LYP [50] and the Gaussian basis-set 6-31G(d,p) to expand the molecular orbitals. Atomic partial charges were calculated using Gaussian then generated through the two-step restrained electrostatic potential (RESP) method implemented in the Antechamber package. All the molecules are reported in figure 3.11 with the indication of the parameters source, whether database or new parametrization. Each inhibitor was placed above the first monomer in the EV about 20 Å away from the constriction region (CR) in the final configuration from the OmpF simulation. Substrates permeation was investigated using well-tempered metadynamics simulations with Plumed 2.2 plug-in [39] within the ACEMD software. [37] As explaned in paragraph 2.2 this method consists in adding Gaussian weight factors that are periodically rescaled providing a convergence parameter to monitor during the metadynamics simulation. [16, 19]

A first step of normal metadynamics simulation of inhibitor permeation was performed until the first effective translocation through the protein constriction region (CR) was observed. Then, four configurations were selected, two with the inhibitor located in the extracellular vestibule (EV), and two in the periplasmic vestibule (PV). Correspondingly, four multiple-walkers [18] were set to extend the well-tempered metadynamics reconstruction of the free-energy surface (FES).

The substrates 'position z' defined as the difference of the z coordinate between the center of mass (com) of the substrate and that of the porin first monomer (on the basis of Cαs) and the 'orientation Φ' of substrate's dipole moment (the z component) were used as biased collective variables. Each walker was run for at least 450 ns that correspond to a total simulation time of 1.8 μs. During the metadynamics, the energy biases were added every 5.0 ps to each collective variable (initial height 1.0 kcal/mol; σ=5 degree and 0.4 Å for orientation and position, respectively). Well tempered ΔT was 4800 K (bias factor=16x300K). Each walker adds its own biases, but it also reads those added by the other walkers, thus accelerating the sampling of the whole space. The one-dimensional free energy surfaces of inhibitors translocation were obtained by integrating out the collective variable orientation. [18]

2.6.1 Conductance

We performed Molecular dynamics simulations to analyze the permeation of ions in the presence of avibactam (**III**). In order to investigate the ion conductance through the trimeric porin, an external electric field was applied using the built-in plugin in ACEMD. [37] A constant force is applied at each charged atom in the system. A representative configuration of the avibactam inhibitor from the minimum found in FES near the constriction region was taken out from meta dynamics trajectories; 100 steps of energy minimization were performed followed by 10 ns of standard MD simulation equilibration step. Starting from last coordinates obtained, two different 50 ns simulations were run with the external electric field and used as further equilibration step: the first one corresponds to an applied potential of 200 mV and the second one

corresponds to an applied potential of -200 mV. Finally, the last configuration obtained by both trajectories was used as the starting point to run 5 independent simulations for each applied potential. Each simulation was run for 100 ns. In order to compare the calculated conductance for the systems described above with respect to the case without any substrate, an external electric field corresponding to an applied potential of either 200 mV and -200 mV was applied to the system in the absence od substrate. For each case, the first 100 ns MD simulation were used as equilibration step, then 5 independent steps of 100 ns MD simulations were run for both the applied potential, see Table S2 in the paper on chapter 3.2.

3 Results and Discussion

3.1 Structural and Electrostatic in Silico Characterization of OmpF/OmpC Orthologues

The primary focus for this work was to analyze the physico-chemical features of different porins from different bacteria species belonging to the family of *Enterobacteriaceae* (fig. 3.1). The main features (internal pore radius, charged residues distribution, internal electric field, etc.) can be obtained on the basis of their 3D-structure. These properties are key to understand their transport mechanism.

The structures obtained by X-ray diffraction show the same beta-barrel arrangement for all the porins, comprising 16 strands with an internal hourglass shape due to the folding of the loop L3 that forms the so-called constriction region (CR).

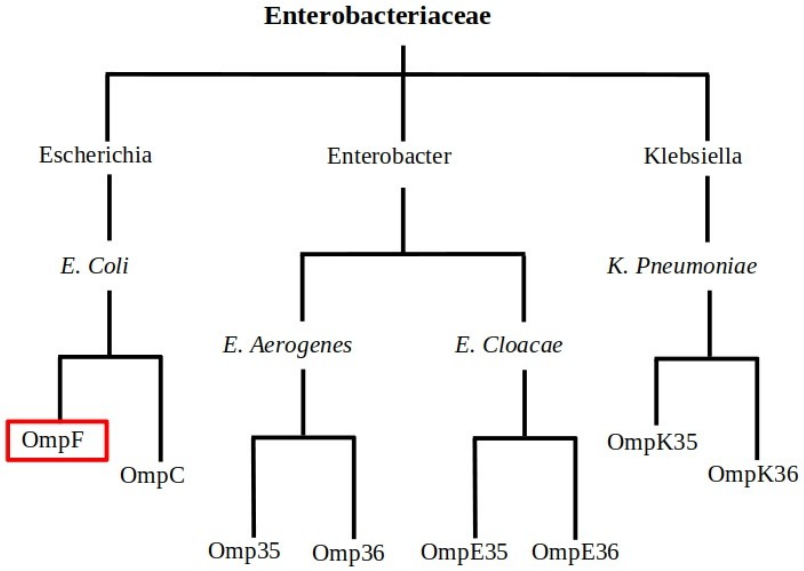

Fig. 3.1: Genealogical tree of *Enterobacteriaceae* family of bacteria: the family is divided into genera with their respective species. For each species, the corresponding general porins are reported.

3.1.2 Structural Analysis

The structural analysis of porins is the first step to determine potential differences in how proteins interact with a given substrate. We started performing a multiple structural alignment, on the basis of one monomer, of the primary sequence. We considered OmpF from *E. Coli* as the reference and we compared its orthologues: Omp35 from *E. Aerogenes*, OmpK35 from *K. Pneumoniae*, OmpE35 from *E. Cloacae*, on the one hand, while we considered OmpC from *E. Coli* as the reference and we compared its ortologues Omp36 from *E. Aerogenes*, OmpK36 from *K. Pneumoniae*, OmpE36 from *E. Cloacae*, on the other (Fig. 3.2: a, b).

The most evident differences are located in external loops, in particular the insertion in loop L1 of OmpF and in loop L5 of Omp36 as shown in fig. 3.2. Conversely, the loop L3 is found to be strictly conserved especially the important negatively charged residues D113, E117 and D121 of OmpF and D105, E109 and D113 of OmpC. These are very important because they face a series of positively charged residues of the barrel in the CR, thus characterizing the latter with a marked charge segregation. Such positively charged residues are commonly referred to as the basic ladder and they are also conserved across the orthologues investigated here, comprising residues K16, R42, R82 and R132 in the OmpF, and K16, R37, R74 and R124 in the OmpC. Using OmpF residues numeration as a reference, a very important difference is found at position 80, right above the basic ladder on the extracellular side. Such difference allows to distinguish the investigated porins into two main groups: the OmpF-like porins present a K residue, while this is substituted by a tryptophan in the OmpC-like porins. Another important difference is found at position 167, which is located again above the basic ladder in the extracellular vestibule. All the OmpF-like porins but OmpE35 have an

arginine in this position, while all the OmpC-like and OmpE35 have a neutral residue, as shown in table 3.1. This difference is very important because all porins have a K or R residue in the adjacent position 168, thus the 167 increases the positive charge density in the region in only three out of the 8 porins under investigation.

a) OmpF-like

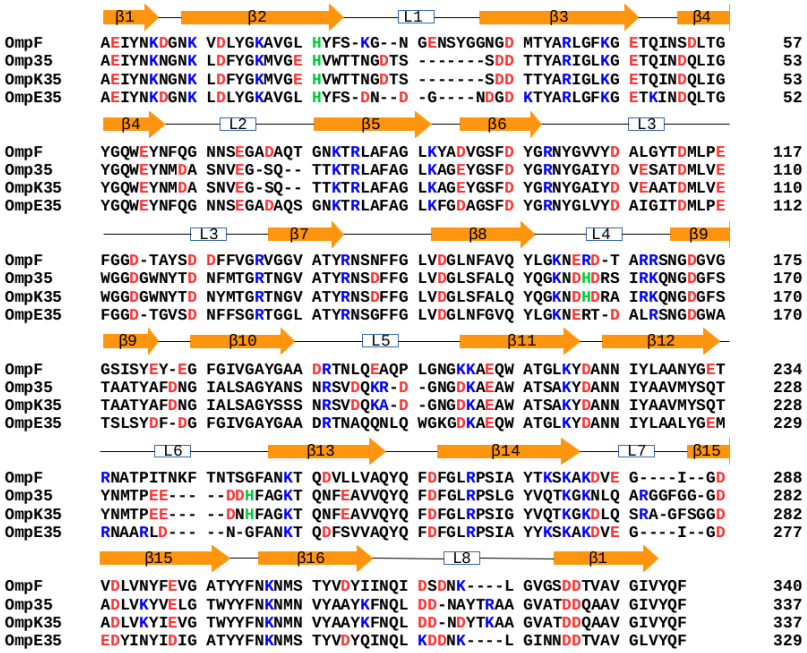

b) OmpC-like

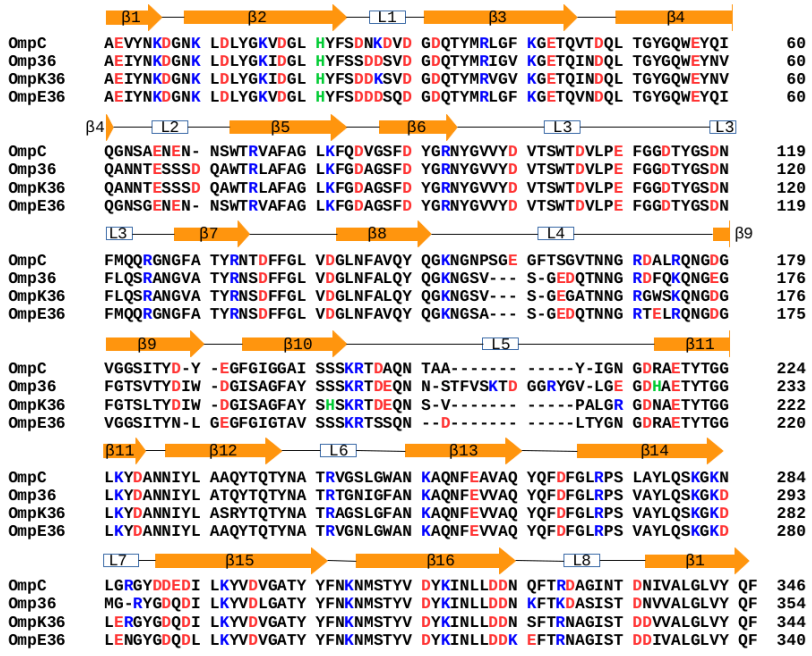

Fig. 3.2: Multiple-structure alignment of first monomer of a) OmpF and its orthologues Omp35, OmpK35 and OmpE35 and b) OmpC and its orthologues Omp36, OmpK36 and OmpE36. Negatively charged residues are highlighted in red, positively charged residues are highlighted in blue and histidine residues are highlighted in green. The secondary structure of porins, β-strands and loops, are reported.

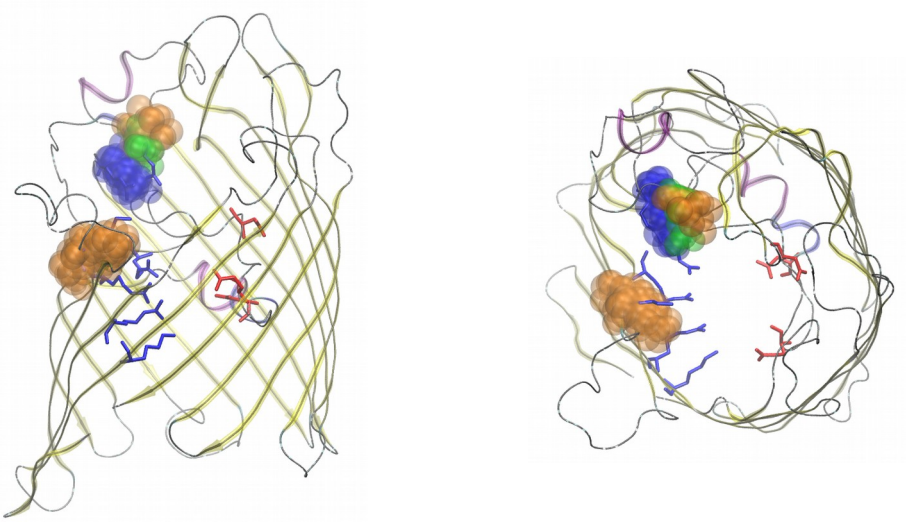

Fig. 3.3: Ompf 3D structure is represented as its secondary structure. The residues of basic ladder and loop L3 defining CR are shown with graphical representation licorice, the residues in position 80, 167 and 168 of all orthologues are shown with graphical representation van der Waals. Positively charged residues are represented in blue, negatively charged residues are represented in red, hydrophobic residues are represented in orange and hydrophilic residues are represented in green.

Tab. 3.1: Main differences in structural alignment among orthologues.

Residue n.	80	167	168
OmpF	K	R	R
Omp35	K	R	K
OmpK35	K	R	K
OmpE35	K	L	R
OmpC	W	L	R
Omp36	W	Q	K
OmpK36	W	S	K
OmpE36	W	L	R

In order to understand “a priori” how the steric hindrance can limit the permeation of a generic substrate, we calculated the cross section radius of the lumen as a function of the z coordinate, i.e. along the main axis of the channel. The comparison among the radius profile obtained from the simulations performed at different ionic strength did not show any significant difference across the two groups. The ions appeared to not influence the intrinsic structure of these porins. Figure 3.4 shows the results obtained for all the orthologues at 200 mM KCl. In table 3.2 the time-average minimum values of the radius observed in the CR are reported. [51] Although difference is not dramatic, in general, OmpC-like are slightly smaller than OmpF-like porins. The shaded area in Fig.3.4 represents the standard deviation of the radius among the three monomers, showing that the latter are absolutely comparable in any case. Finally, by taking into account both charged residues conservation and the radius profile, we concluded that actually the two most studied porins, OmpF and OmpC, could be used as a model for all the OmpF-like orthologues and OmpC-like orthologues, respectively, in all successive investigations.

Tab. 3.2: the time-average minimum values of the radius observed in the CR. [51]

	OmpF	Omp35	OmpK35	OmpE35	OmpC	Omp36	OmpK36	OmpE36
r (Å)	3.1±1.1	3.6±1.7	3.6±1.4	3.1±1.3	2.8±1.1	3.0±1.3	2.8±1.4	3.1±1.6

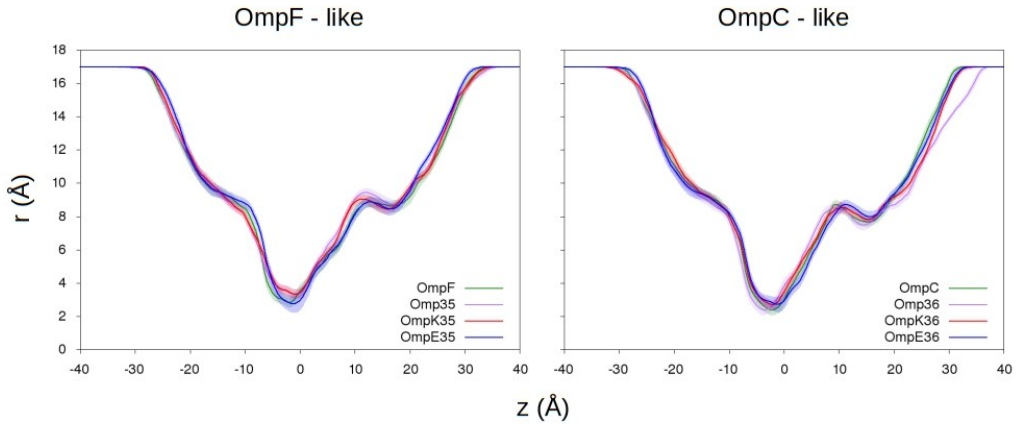

Fig. 3.4: Comparison among averaged time radius as a function of z coordinate of OmpF-like orthologues and OmpC-like orthologues. The fluctuations of the radius size among three monomers was defined by standard deviation represented with shaded regions.

3.1.3 Free Energy of Ion Permeation

All the investigated porins are negatively charged and slightly cation selective. The selectivity to ions is defined as the ratio between the permeability to positive ions over permeability to negative ions (P_{K^+}/P_{cl^-}). From the reference [51], in table 3.3 selectivity values determined from experimental single-channel electrophysiology are reported.

Tab. 3.3: Selectivity values obtained through experimental single-channel electrophysiology. [51]

	OmpF	Omp35	OmpK35	OmpE35	OmpC	Omp36	OmpK36	OmpE36
P_{K^+}/P_{Cl^-}	1.33	1.72	1.36	1.42	2.20	2.22	1.68	2.13

In general, the higher negative charge of OmpC-like porins correlates with a higher selectivity than OmpF-like porins. In order to understand structural features governing the transport of ions, the free energy profile of ion permeation has been calculated. The density of ions averaged during the time simulation has been calculated along the z axes of diffusion dividing the space inside a cylinder of radius 17 Å in windows of 1 Å along z. Starting from the ion density, the free energy profile as a function of z is calculated using the following equation

$$\Delta G = -k_B T \ln\left(\frac{\rho_i}{\rho_{bulk}}\right) \qquad 55)$$

The average over the three monomers are reported in figure 3.5 and the standard deviation is represented with the shaded regions. The large selectivity for K^+ ions in OmpC-like porins could be explained considering the deeper minimum around z=0 and the smallest energy barrier that ions have to overcome. As far as the permeation of Cl^-

ions is concerned, differences between the two groups are more evident. The height of the energy barrier that Cl^- ions have to overcome is comparable. However, in OmpF-like porins, we have an energy minimum between 0 and 6 Å for Cl- that might explain the different permeability. This is due to the presence of a lysine residue at position 80 in OmpF-like porins able to increase the affinity for negative ions. Overall, differences across the orthologue proteins belonging to the same group is negligible. As already mentioned, also this analysis shows that OmpF and OmpC can be used as models for the respective group of orthologues across the family of *Enterobacteriaceae*.

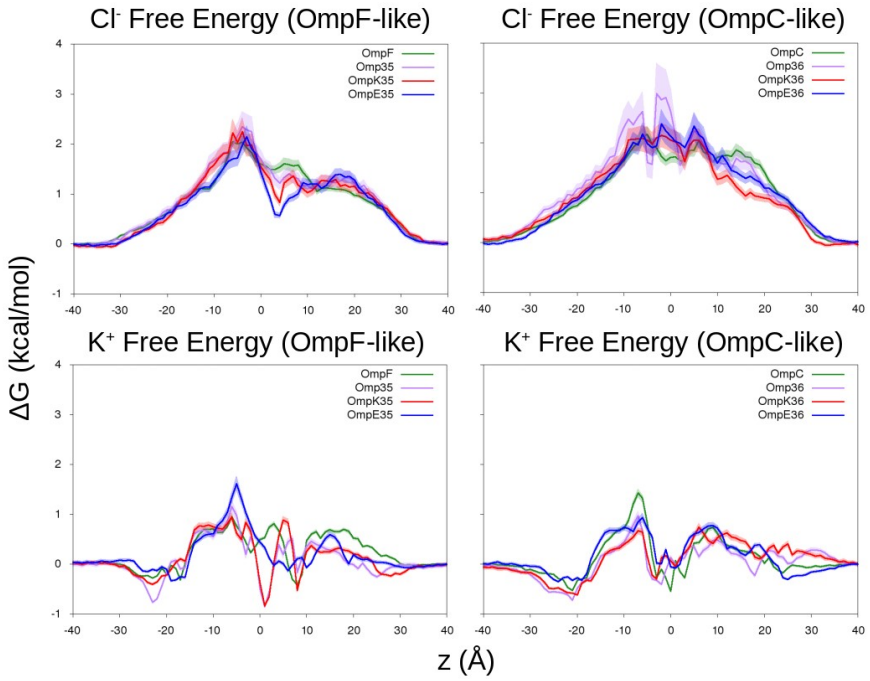

Fig. 3.5: The free energy profile of K^+ and Cl^- permeation was calculated as a function of z coordinate using equation 49 starting from the ion density. The fluctuations of the radius size among three monomers was defined by standard deviation represented with shaded regions.

3.1.4 Charge Distribution

The main aim of this work is to understand how β-lactamase inhibitors and similar compounds are passively transported through OmpF/OmpC porins and their orthologues across the family of *Enterobacteriaceae*. Interactions and, as a consequence, permeability of charged substrates like ions, metabolites, antibiotics or inhibitors, clearly depends strongly on the charge distribution inside the lumen and not simply by the net charge of the porin. In other words, specific interactions are expected to play a major role. The charge distribution also modulates the internal electric field of the pore (cap. 1).

In order to characterize how the distribution of charged residues changes along the z axes, a first comparison has been made by dividing the pore into three macro-regions: the extracellular vestibule, the constriction region and the periplasmic vestibule. The value of the net charge was obtained from the algebraic sum of the charged residues in these three regions (fig. 3.6).

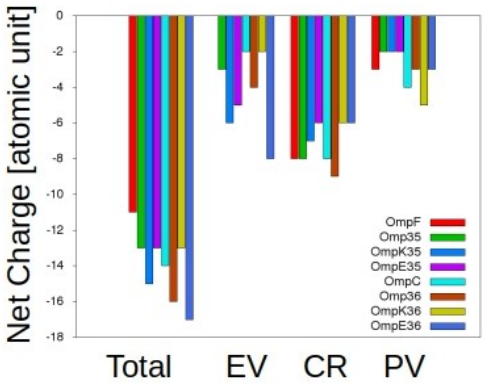

Fig. 3.6: The net charge of the first monomer centered of their center of mass. of OmpF and its orthologues and OmpC and its othologues. In the histogram are reported total charge, charge of extracellular vestibule (EV, z>10 Å), charge of constriction region (CR, -10 Å <z<10 Å), and charge of periplasmic vestibule (PV, z<-10 Å).

The EV shows the largest differences in net charge among the orthologues. This is mostly due to the differences in the primary sequence and to the insertions in the external loops, as mentioned above. The EV region, which is rich in long loops, is important for the first interaction with the substrate. The mobility and the charge of these loops have the task to attract or reject substrates approaching the porin.

The CR is the most conserved macro-region of the channel, and this is not surprising since it represents the main filter to the passive diffusion of ions and metabolites so it is hardly modified across the different species, at least within the *Enterobacteriaceae* family. It shows, in general, a higher net negative charge with respect to the other macro-regions except for the OmpE36. The CR is the steric bottleneck for the permeation process and its charge distribution is crucial for interaction with substrates that have to cross the region. As explained in the introduction, the CR shows the most intense value of transversal electric field that can impose the alignment of the substrates endowed with a strong dipole moment.

In the PV region, all the orthologues have the lowest negative charge with only slight differences, suggesting that this region has a minor influence in the overall permeation process.

In order to characterize the charge distribution of the protein deeper at the atomic level, the three macro-regions were divided into narrower windows along the z axes. Windows with a thickness of 6 Å and with 1 Å of overlap between two adjacent slices were selected (fig. 3.7). For each slice, the xy-distribution of positively and negatively charged residues was calculated from the coordinates recorded along the MD trajectories (fig. 3.8). The bi-dimensional histogram reports the ΔP_{xy} parameter calculated as the difference between the xy-distribution of the positively and the negatively charged residues for each section / z-window.

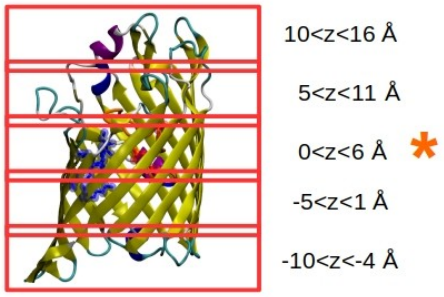

Fig. 3.7: Windows with a thickness of 6 Å and with 1 Å of overlap between two adjacent slices of protein. The orange asterisk highlights the section were the most relevant differences in the charge distribution are located.

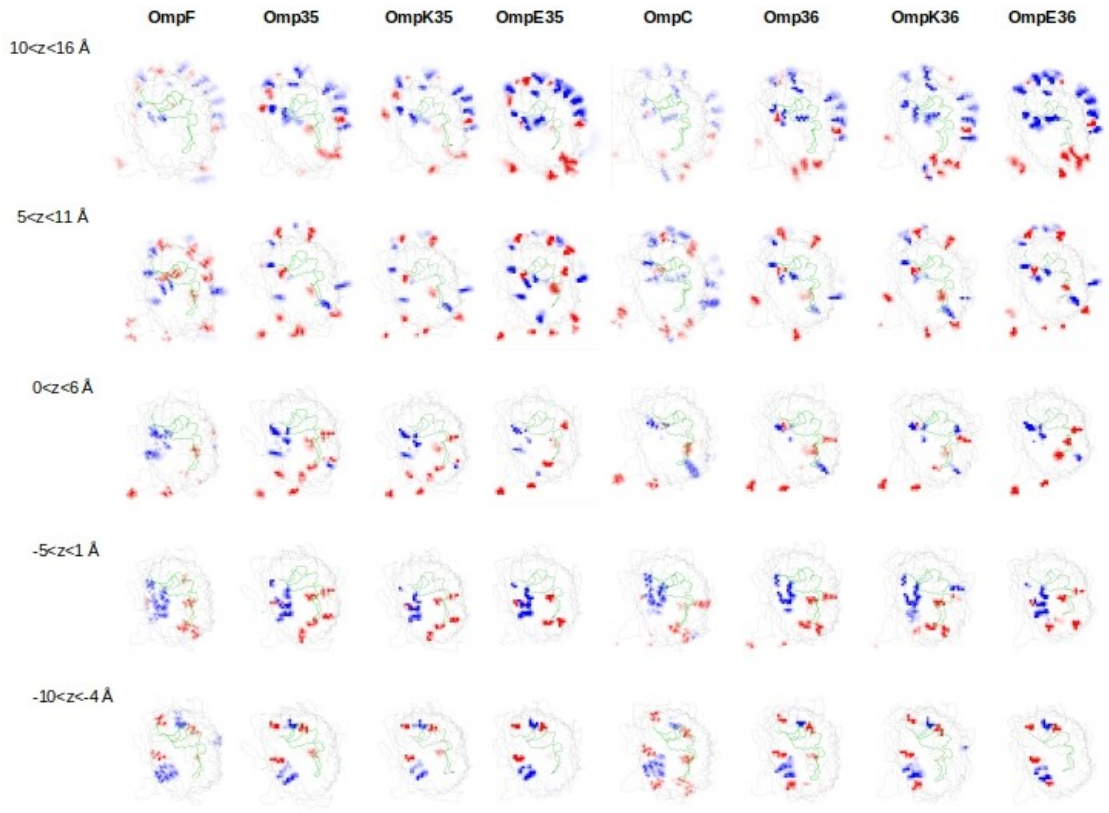

Fig. 3.8: The difference between the distribution of positive residues (blue) and negative residues (red) on xy-plane was calculated for OmpF, Omp35, OmpK35, OmpE35, OmpC, Omp36, OmpK36 and OmpE36. All monomers are centered in their center of mass.

The most relevant difference in the charge distribution is located at level of window with 0<z<6 Å. Here, as already seen previously, the K80 residue is conserved only for OmpF-like orthologues (fig. 3.9). This region was already called the ‘preorientation region’ and it allows to distinguish the porin-type and it is responsible of the change in the transversal electric-field right before the CR. As a consequence, it is responsible of the reorientation of the dipolar substrates when approaching the CR coming from the EV. On the other hand, all of the other z-windows resulted to be more comparable with only small negligible differences when OmpF-like and OmpC-like porins are compared one another.

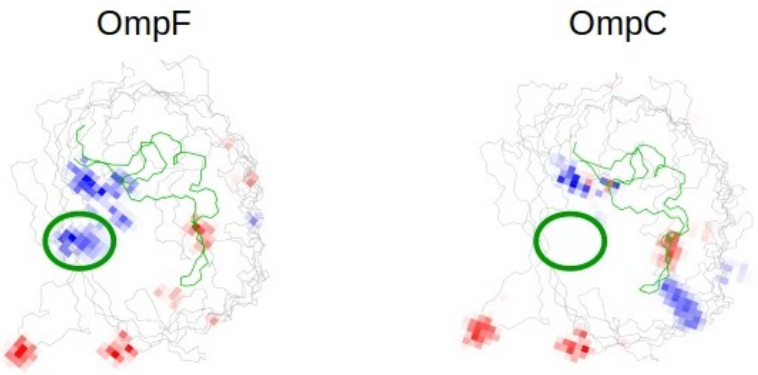

Fig. 3.9: Cross section 0<z<6 Å onto xy-plane of OmpF (right) and OmpC (left). The green circle highlight the K80 residue conserved only on OmpF-like. More differences are located on the opposite side of K80: OmpF-like shows a low negative charge instead OmpC-like show a hight positive charge.

3.2 General Method to Determine the Flux of Charged Molecules through Nanopores Applied to β-Lactamase Inhibitors and OmpF

As explained in the introduction, one of the few experimental techniques that allows to estimate the flow of substrates through the protein channels is represented by electrophysiology [14]. This technique, however, is limited by the impossibility of discriminating between the actual translocation of the drug and the interaction with possible binding/affinity sites within the channel to finally exit back on the same side of the channel. In addition, sometimes it is very difficult to observe small changes in the ionic current induced by small/fast substrates, thus requiring sophisticated methods of background noise analysis. In this regard, a large part of this thesis has seen the use of Molecular Dynamics and Well-tempered Metadynamics simulations to provide more details, at the atomic level, on the interactions between the substrates and the protein channels. We combined simulation with electrophysiology to understand better a new experimental methodology for measuring the permeability of charged substrates. This method relies on the Nernst potential and on the calculation of the reversal potential. [6] Since OmpF is cation selective, by preparing OmpF with a gradient concentration of ions between the CIS and TRANS compartment, it is possible to measure a positive ion current through the electrophysiology apparatus. By applying a (reversal) potential that nullify the current, it is possible to evaluate the permeability ratio between the positive and negative ions in solution. Thus, when a ionic molecular species is inserted instead of one of the two monoatomic ions, eventually we can evaluate the permeability of such molecule with respect to the other ion (bionic condition). The focus was on the quantification of the permeability coefficient of three anionic β-lactamase inhibitors, avibactam, sulbactam e tazobactam (fig. 3.10), through OmpF measured with respect to

the permeability of of K^+/Na^+ in bionic conditions, and in addition Cl^- ions in trionic condition.

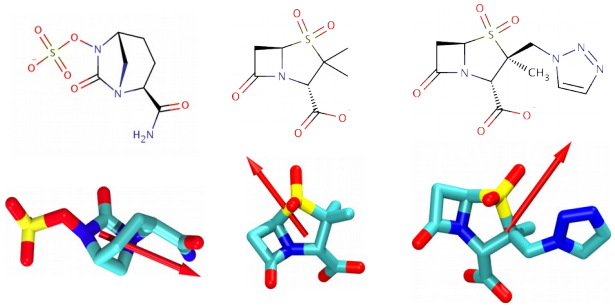

Fig. 3.10: 2D and 3D structures (with relative dipole) of the three β-lactamase inhibitors studied; from left to right: avibactam (**III**), sulbactam (**I**), tazobactam (**II**).

Our contribution to this work was related to the need of deeply understanding the origin of the rapid permeation of the inhibitors. During this work, all-atom MD simulations were performed to reconstruct the permeation free energy of avibactam and the two ions K^+ and Cl^- independently and, by using a diffusion model, their relative permeability was calculated. The free energy for two monoatomic ions was evaluated from the relative ion density with the formula 49. Permeation free-energy surface of avibactam through OmpF was obtained by using WMETAD with multiple walkers (paragraph 2.2) to accelerate the evolution of the avibactam molecule inside of the pore.

The results related to this part of the research are reported in the following paper. [52]

THE JOURNAL OF PHYSICAL CHEMISTRY Letters

Letter

pubs.acs.org/JPCL

General Method to Determine the Flux of Charged Molecules through Nanopores Applied to β-Lactamase Inhibitors and OmpF

Ishan Ghai,[†] Alessandro Pira,[‡] Mariano Andrea Scorciapino,[§] Igor Bodrenko,[‡] Lorraine Benier,[†] Matteo Ceccarelli,[‡] Mathias Winterhalter,[†] and Richard Wagner*[,†]

[†]Department of Life Sciences and Chemistry, Jacobs University Bremen, 28719 Bremen, Germany

[‡]Department of Physics, University of Cagliari, Cagliari 09124, Italy

[§]Department of Biomedical Sciences, University of Cagliari, Cagliari 09124, Italy

Supporting Information

ABSTRACT: A major challenge in the discovery of the new antibiotics against Gram-negative bacteria is to achieve sufficiently fast permeation in order to avoid high doses causing toxic side effects. So far, suitable assays for quantifying the uptake of charged antibiotics into bacteria are lacking. We apply an electrophysiological zero-current assay using concentration gradients of β-lactamase inhibitors combined with single-channel conductance to quantify their flux rates through OmpF. Molecular dynamic simulations provide in addition details on the interactions between the nanopore wall and the charged solutes. In particular, the interaction barrier for three β-lactamase inhibitors is surprisingly as low as 3−5 kcal/mol and only slightly above the diffusion barrier of ions such as chloride. Within our macroscopic constant field model, we determine that at a zero-membrane potential a concentration gradient of 10 μM of avibactam, sulbactam, or tazobactam can create flux rates of roughly 620 molecules/s per OmpF trimer.

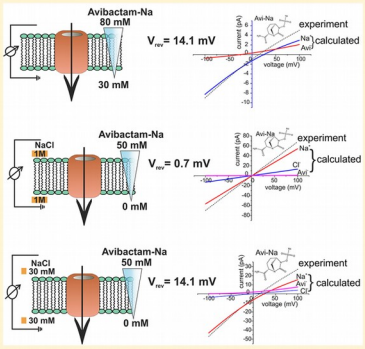

Sensing of individual molecules has become an important analytical tool for biochemistry, biophysics, and chemistry, leading to development of next-generation bioanalytical and diagnostic tools.[1−3] Among single-molecule techniques, sensing with nanopores is a fast-growing field with its most prominent application of high-throughput sensing of nucleic acids.[3,4] In nanopore sensing, individual molecules pass through a nanoscale pore, thereby producing detectable changes in ionic currents.[5]

Gram-negative bacteria have a complex cell envelope comprising an outer and an inner membrane that delimit the periplasm from the extracellular environment. The outer membrane contains numerous protein channels, called porins. These nanopores facilitate the chemical potential-driven flux of small hydrophilic substances.[6] Porins are considered to be the main entry pathway for polar antibiotics, such as cephalosporins, penicillins, carbapenems, and fluoroquinolones, as well as for charged β-lactamase inhibitors.

In order to design the next generation of antibiotic molecules that will be able to overcome the membrane barrier more effectively, it is desirable to quantify the flux of individual solutes through nanopores present in the barrier.[6,7] Currently, the lack of such an assay is a substantial bottleneck for optimization of new molecules with respect to permeability and, ultimately, their antimicrobial activity against intact bacterial cells.[8] In order to support the urgent search for new antibiotics, the European Union and the EFPIA financed the "New Drugs for Bad Bugs" platform (www.ND4BB.eu). Within this platform, "Translocation" is devoted to find the causes for the low permeability.

Recently, we investigated the permeation of antibiotics through channels by analyzing the ion current fluctuations induced by the presence of substrates expected to permeate. Unfortunately, most small antimicrobial molecules do not produce easily detectable changes in the ion currents while passing the nanopore and require an extended current event or sophisticated current noise analysis methods.[5,7] Here we present an approach to characterize transport of charged molecules even if they do not produce detectable changes in the nanopore current fluctuations.

The measurement of the ion selectivity of a membrane pore is an established method to obtain the relative permeability in terms of fluxes of the ions present in solution. However, in order to determine turnover numbers of the individual permeating ions, knowledge of their single-channel conductances is also required.[7−11] Here we describe an approach to quantify the permeation of three charged β-lactamase inhibitors, namely, avibactam, sulbactam, and tazobactam (Figure S1), through the OmpF porin from *Escherichia coli*. Moreover, we show that the macroscopic turnover number obtained experimentally can be complemented with all-atom molecular dynamics (MD) modeling, providing atomic details on the selectivity and the energetics of transport. Our results

Received: January 10, 2017
Accepted: February 27, 2017
Published: February 27, 2017

DOI: 10.1021/acs.jpclett.7b00062
J. Phys. Chem. Lett. 2017, 8, 1295−1301

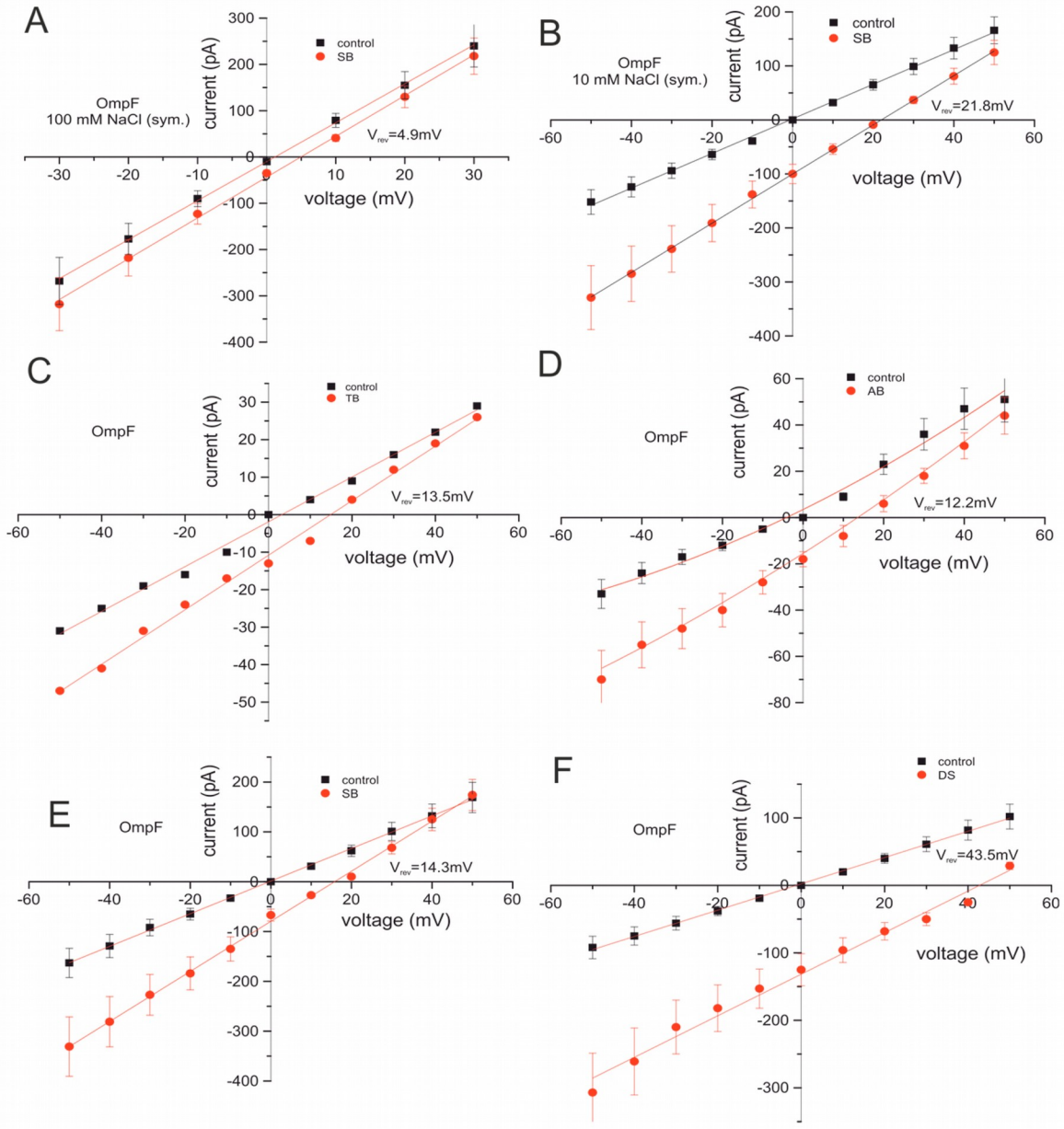

Figure 1. Selected $I-V$ curves from bilayers containing one or many reconstituted OmpF channels with different β-lactamase inhibitors under bi- or tri-ionic conditions. The cis side refers to the electrical ground. (A) Symmetrical 100 mM NaCl (cis/trans) in the absence (control) and presence of additional 50 mM Na-sulbactam (cis); about 17 channels. (B) Symmetrical 10 mM NaCl (cis/trans) and additional 50 mM Na-sulbactam (cis); 55 channels. (C) Bi-ionic recordings with symmetrical 30 mM Na-tazobactam (7 cis/trans) as a control and additional 50 mM Na-tazobactam on cis (80/30 mM Na-tazobactam cis/trans); 2 channels. (D) Same as (C) with Na-avibactam; 3 channels. (E) Same as (C) and (D) with Na-sulbactam; 8 channels. (F) Control measurement bi-ionic recordings with symmetrical 10 mM Na-dextran sulfate (cis/trans) as the control and additional 50 mM Na-dextran sulfate on cis (60/10 mM Na-dextran sulfate cis/trans). Note that ion concentration values refer to the monomer of polydextran and that each monomer sulfate group carries three Na^+ and, thus, additional 30 mM Na^+ (see the Supporting Information).

show that the OmpF nanopore is highly permeable for the above-mentioned β-lactamase inhibitors. MD simulations reveal how these inhibitors find favorable interactions along a series of cationic residues inside of the pore, just above the constriction region, with a rather low barrier to penetrate, between 3 and 5 kcal/mol, without blocking the channel for the passage of ions, thus invisible to standard electrophysiology measurements.

Single-Channel Recording under Symmetric Conditions: Bi- and Tri-ionic Potential. In order to obtain information on permeation of β-lactamase inhibitors through OmpF, we reconstituted trimeric OmpF into a planar lipid bilayer. The channel revealed a conductance of G_{trimer} = 960 ± 100 pS (100 mM NaCl, cis/trans) in agreement with previous publications (see also Supporting Information Figure S4A,B).[12,13] The addition of Na-avibactam to the cis side (Figure S4A) or both sides of the channel (details not shown) did not cause any significant concentration-dependent changes in channel gating. Similar results were obtained from this type of experiments for sulbactam-Na and tazobactam-Na (details not shown). Therefore, this category of experiments is not suitable to gain detailed information on possible transport modes of these β-lactamase inhibitors through OmpF.

DOI: 10.1021/acs.jpclett.7b00062
J. Phys. Chem. Lett. 2017, 8, 1295−1301

In the second series of experiments, we measured OmpF conductance under symmetrical bi-ionic conditions at low symmetrical concentration (30 mM, cis/trans, Figures S5−S8) by using the sodium salts of the β-lactamase inhibitors. The results of these measurements and the corresponding MD calculations are summarized in Table S1. Surprisingly, replacing the chloride ion by the large β-lactamase inhibitor anions did change the conductance (G^{NaCl}_{trimer} = 270 ± 60 pS) only within the experimental error.

Single-Channel Recording under Asymmetric Conditions: Bi- and Tri-ionic Potential. In order to gain information on the permeability of OmpF for the β-lactamase inhibitor anions, we applied an alternative experimental approach based on the Goldman−Hodgkin−Katz (GHK) current equation.[9−11] We followed a previous suggestion to analyze the selectivity of the OmpF containing artificial bilayer membranes under bi- and tri-ionic conditions on both sites of the planar bilayer.[5,11,12] Because ion fluxes are also created by concentration gradients, the GHK current equation allows calculation of the relative ion permeability by macroscopic GHK theory using the chemical potential created by the different electrophoretic mobility of the ions themselves.[9] Starting from the GHK current equation for a given composition of ions in solution, the voltage-dependent total ion current $I(V)$ crossing a membrane channel is given by the sum of the individual ion currents $I_x(V)$[9]

$$I(V) = \sum I_x(V) \tag{1}$$

and specifically in our case the main contributors are Na^+, Cl^-, and the inhibitor (inh^-)

$$\sum I(V) = I_{Na^+}(V) + I_{Cl^-}(V) + I_{inh^-}(V) \tag{2}$$

with

$$I_x(V, P_x, z, c_{cis}, c_{trans}) = P_x z^2 \frac{VF^2}{RT} \cdot \frac{\left(c_{x,cis} - c_{x,trans} \exp\left(\frac{-zFV}{RT}\right)\right)}{1 - \exp\left(\frac{-zFV}{RT}\right)} \tag{3}$$

where V is the transmembrane voltage, P_x the permeability for the ion x, z the valency, F = 9.6 × 10^4 As mol^{-1} the Faraday constant, and R = 8.3 J mol^{-1} K^{-1} the gas constant. In the experimental input, $c_{x,cis}$ and $c_{x,trans}$ are the ion concentrations on the two sites of the membrane.

In the experiments described below, the total current $I(V)$ was measured at particular bi- or tri-ionic conditions in the cis and trans compartments separated by an OmpF-containing bilayer as a function of transmembrane voltages applied. With respect to antibiotics, it is worth mentioning that the typical solubility (on the order of few mM) is a challenge in particular for electrophysiological measurements, especially when this is combined with the availability of only small amounts as antibiotic candidates during test periods typically come from small-scale synthesis of noncommercial products. To circumvent this issue, we applied an experimental setup where an OmpF-containing membrane bathed in symmetrical low NaCl concentration (cis/trans) was supplemented with a low concentration of the Na^+ salt of β-lactamase inhibitor on one side only (tri-ionic conditions) and ion channel currents were measured before and after addition of the β-lactamase inhibitor (see the Supporting Information for details). Furthermore, for calibration purposes, we employed also asymmetric bi-ionic conditions by using the sodium salts of the β-lactamase inhibitors on both sides of the membrane containing OmpF channels. Measurements of the current vs voltage ($I-V$) curves with different β-lactamase inhibitors under both bi- and tri-ionic conditions were performed as described in the Supporting Information. Representative $I-V$ plots are shown in (Figure 1).

The different slopes of the $I-V$ curves shown in Figure1 are due to a different number of channels incorporated into the respective bilayers (see also Figures S5−S8). Nevertheless, reversal potentials are independent of the number of channels. The measured V_{rev} for the investigated β-lactamase anions suggested that they can pass the OmpF pore to a remarkable extent. The corresponding permeability ratios P_{inh^-}/P_{Na^+} were calculated as described in detail in the Supporting Information. As a negative control, we used the Na^+ salt of the large branched polysaccharide, polydextran sulfate (average $\overline{Mw}$ ≅ 8 kDa, r_{Stokes} > 2.5 nm), because the large anion is expected not to permeate the OmpF pore (Figure 1F). With a Na-dextran-sulfate gradient of 60/10 mM (cis/trans), we obtained V_{rev} = 43 ± 3.4 mV. This value of V_{rev} is, within experimental error, identical to the Nernst potential (defined as the equilibrium potential that appears if only one type of ion permeates) of V_{Nernst} = 44.8 mV calculated for Na^+ ions, which clearly shows that the large anionic polymer cannot permeate through OmpF. In Table 1, calculated permeability ratios obtained under bi-ionic conditions are listed for the three β-lactamase inhibitors and sodium chloride.

Table 1. Bi-ionic Permeability Ratios of the β-Lactamase Inhibitors (P_{anion^-}/P_{Na^+}) for the Current Flux through OmpF

	β-lactamase inhibitor	P_{anion^-}/P_{Na^+}
OmpF Escherichia coli (DB EGT69961.1)	avibactam-Na	0.32
	sulbactam-Na	0.25
	tazobactam-Na	0.28
	NaCl	0.25

If we accept the GHK assumptions, that is, cations and anions move independently through the channel, we can use single-pore conductance and the obtained relative permeability ratio P_{anion^-}/P_{Na^+} to separate the individual contributions of cations and anions to the total current determined in a single experiment.[12−15] Using the measured $\overline{G}_{monomer}$ ≅ 90 pS for avibactam-Na (Table S1) at 30 mM (cis/trans) and the selectivity of $P_{avibactam^-}/P_{Na^+}$ = 0.32, we calculated the contribution of the anionic avibactam to the total current at V_m = 100 mV using eq 2 at the given concentration gradient of $\Delta c_{cis/trans}$ = 50 mM (Figure S3). With this, the turnover number of avibactam could be calculated. As reported in the Supporting Information in detail, by extrapolating linearly from mM to low 10 μM concentrations, we obtained a turnover rate of n ≅ 600 molecules/s (per trimer) at a concentration gradient of Δc = 10 μM and at zero membrane potential.

To investigate the robustness of our approach, we also tested the permeability of sulbactam-Na and tazobactam-Na through the OmpF pore under tri-ionic conditions (see the Supporting Information for details). The measured V_{rev} and permeability ratios calculated (as described in the Supporting Information) are listed in Table 2.

The permeability ratio for Na-sulbactam under bi-ionic conditions (Table 1) was P_{SB^-}/P_{Na^+} = 0.25, which compares with the tri-ionic values of P_{SB^-}/P_{Na^+} = 0.3 (10 mM NaCl background) and P_{SB^-}/P_{Na^+} = 0.55 (100 mM NaCl back-

DOI: 10.1021/acs.jpclett.7b00062
J. Phys. Chem. Lett. 2017, 8, 1295−1301

Table 2. Permeability of Sulbactam-Na and Tazobactam-Na through the OmpF Pore under Tri-ionic Conditions

β-lactamase inhibitor	NaCl [mM] (cis/trans)	inhibitor [mM] (cis)	V_{rev} [mV] (exp)	P_{Na^+} / P_{Cl^-}/ P_{inh^-} (calc)[a]
sulbactam-Na	10	50	21 ± 6	4:1:1.2
	100	50	5 ± 2	4:1:2.2
tazobactam-Na	10	50	20 ± 4	4:1:2.2

[a]The permeability ratio of P_{Na^+}/P_{Cl^-} = 4:1 for OmpF was determined independently under bi-ionic conditions and was fixed during fitting of V_{rev} (tri-ionic).

ground). However, the permeability ratio for Na-tazobactam under bi-ionic conditions (Table 2) was P_{TB^-}/P_{Na^+} = 0.28, which compares with the tri-ionic value P_{TB^-}/P_{Na^+} = 0.45 (at 30 mM Na Cl background).

The significant differences obtained between permeability ratios at different symmetrical NaCl concentrations show that the GHK theory assumption of completely independent ion movements through the channel are not met, especially at higher NaCl background concentrations. Nevertheless, the parameters obtained under bi-ionic and tri-ionic conditions with lower NaCl concentrations are within a reasonable range and show that our experimental approach combined with macroscopic GHK theory can be applied to gain explicit information on the fluxes of the β-lactam inhibitor anions through different porins, otherwise hard to measure directly.

Molecular Simulations. In order to understand the origin of the rapid permeation of the inhibitors, we investigated their energetics by using molecular modeling, focusing in particular on avibactam. We performed all-atom MD simulations to reconstruct the permeation free energy of avibactam and the two ions independently, and by using a diffusion model, we calculated their relative permeability. For the two ions, we evaluated the free energy from the relative ion density with the formula $\Delta G_{(Z)} = k_B \cdot \ln d_{(Z)}/d_{bulk}$.[21] Standard MD simulations (600 ns) at a concentration of 200 mM NaCl were performed to gain the required meaningful exploration of the OmpF interior.

Permeation free-energy of avibactam through OmpF was obtained by using well-tempered metadynamics with multiple walkers to accelerate the evolution of a single avibactam molecule inside of the pore. In Figure 2, we show the reconstructed free energy of avibactam with respect to the two biased coordinates, the position of its center of mass with respect to the axis of diffusion Z, and orientation of its dipole moment along the same axis Z. A preferred interaction was found in the region right above the constriction region, the so-called preorientation region, between 3 and 8 Å from the center (purple in Figure 2) as well as deeper in the constriction region (orange in Figure 2) down to the saddle point (green in Figure 2). The translocation path is characterized by avibactam aligning its dipole to the transversal electric field[17,18] and, at the same time, direct interactions (i) with the positive residues of the basic ladder (R167, R168, R82, K16) by the sulfate group and (ii) the negatively charged residues of the loop L3 (D121, E117, D113) by its NH_2 group. It is worth mentioning that the deepest energy minimum (purple in Figure 2) does not correspond to current blockage by avibactam (see Figure S10).

Permeation of avibactam was confirmed by simulating the system under the same bi-ionic conditions as those applied in the experiments, that is, 30 mM avibactam-Na. We applied an external electric field of 700 mV. This relatively large voltage is

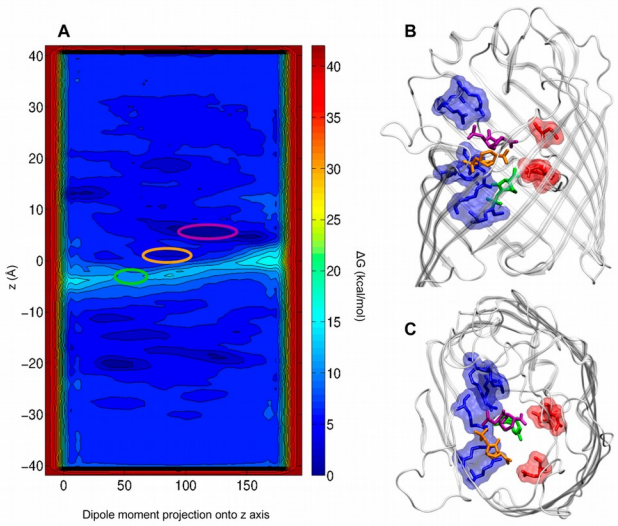

Figure 2. (A) Two-dimensional free energy of permeation for avibactam as reconstructed from metadynamics simulations. (B) Side view and (C) top view of the avibactam inside of OmpF in the two lowest minima near the constriction region and at the transition state.

typically applied in simulations to have permeation in a reasonable time.[13,17,18] In Figure 3, we report two reactive paths followed by avibactam projected onto the free-energy surface obtained before. As we can see, reactive trajectories visit several states before crossing the constriction region, where avibactam overcomes the energy barrier exactly through the saddle point identified.

In order to compare the energetics of avibactam with that of ions, in Figure 4 we show the free energy projected only along the axis of diffusion Z. Avibactam has to cross a central barrier of about 3.5 kcal/mol to be compared with 2 kcal/mol for chloride and less than 1 kcal/mol for sodium. The other two inhibitors have a barrier slightly higher than that of avibactam (see Figure S9).

We estimated the channel conductance for the different species and their permeability ratio (Table 3) by using independent 100 ns standard MD simulations performed at an applied membrane potential of V_m = 200 mV with avibactam only starting from the preorientation minimum. Five independent trajectories showed that avibactam stayed in the preorientation region when a positive voltage was applied, probably pushed by the external voltage on the one hand but not able to cross the constriction region barrier on the other, at least in the limited time of 100 ns. In this stable configuration, avibactam occupied the chloride path while affecting the cations' path only to a marginal extent (Figure S10). By calculating the permeability ratio cations/anions, we could highlight an enhanced cation selectivity in the presence of avibactam, probably due to its negative charge coordinating the positive ladder inside of the channel, allowing easier permeation for cations (Tables 3 and 4). It seems that the decreased anion conductivity, due to avibactam physically occupying the anions' path (Figure S10), was compensated by the increased cation permeation (Table 4).

On the basis of the energy profiles, the permeability ratio can be evaluated in linear regime with the formula:

DOI: 10.1021/acs.jpclett.7b00062
J. Phys. Chem. Lett. 2017, 8, 1295−1301

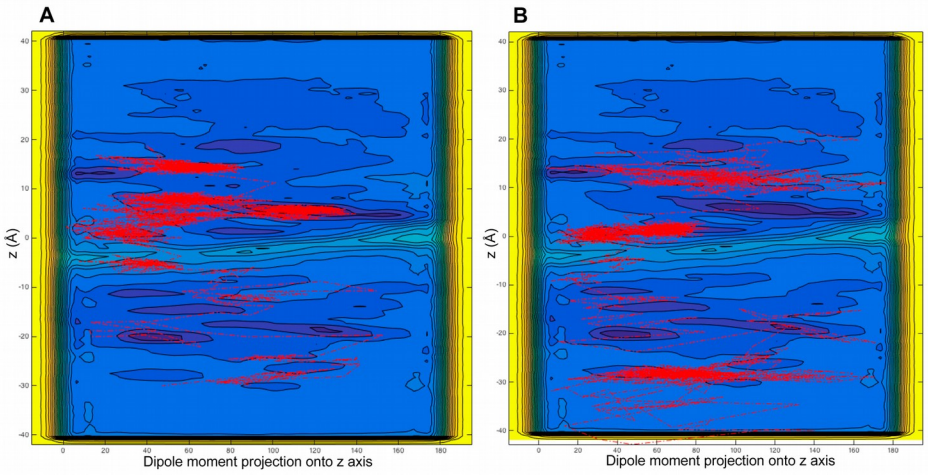

Figure 3. Translocation path of avibactam molecules with an external electric field in bi-ionic conditions (Na-avibactam 30 mM) inside of OmpF projected on the free-energy surface: (A) 300 K and 700 mV; (B) 310 K and 700 mV.

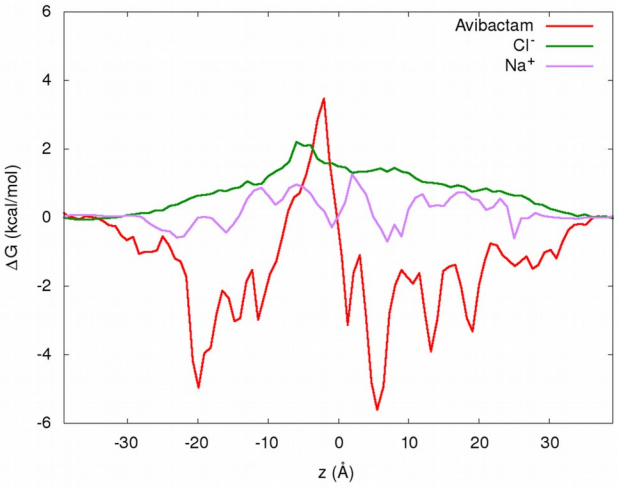

Figure 4. Free-energy surface of avibactam from Figure S9 projected along the Z axis of diffusion and, for a comparison with free energies of $Cl^-$and Na^+ ions, calculated using their relative densities with respect to the bulk.

Table 3. Conductance and Permeability Coefficients Obtained from the Diffusion Model[a]

ion	G [pS]/mM	permeability/P^+
Na^+	7.2	1
Cl^-	1.9	0.26
avibactam(−)	2.2	0.31

[a]Conductance values are calculated at 30 mM concentration and normalized to 1 mM. The permeability ratio to Na^+ is shown in the right column. The free energies used were those of Figure 4.

$$P = \left[\int_0^L \frac{\exp\left(\frac{U(Z)}{kT}\right)}{D(Z)}\,dZ\right]^{-1} \tag{4}$$

Here, $U(Z)$ is the potential of mean force (the free energies of Figure 4) for the ion/molecule at position Z (normalized as follows, $U(0) = 0$), $D(Z)$ is the local diffusion constant inside of the OmpF, and L is the geometrical length of the channel.

Table 4. Conductance Values Obtained from the Diffusion Model in the Linear Regime with a Mean-Field Potential Approach

ion	G [pS]/mM	permeability/P^+
Diffusion Model with Calculated Free Energies at 200 mM		
K^+	7	1
Cl^-	2.3	0.3
avibactam(−)	2.2	0.3
tazobactam(−)	0.6	0.09
sulbactam(−)	0.25	0.04
MD Simulations with External Electric Field (200 mM and 200 mV, 5 trajectories 100 ns)		
K^+	3.3 ± 0.3	1
Cl^-	1.1 ± 0.2	0.3
K^+ with one avibactam bound	4.1 ± 0.5	1
Cl^- with one avibactam bound	0.8 ± 0.2	0.2

Then, the channel conductance for ion type i at the symmetric condition, in the small-voltage limit, reads

$$G_i = P_i q_i^2 c_i \frac{F^2}{RT} S_c \tag{5}$$

where P_i, q_i, and c_i are the permeability coefficient (nm/ns), the charge in atomic units, and the molar concentration, respectively, for the ions; F is Faraday's constant, R is the ideal gas constant, and S_c is the geometric cross section at the mouth of the channel, corresponding to a radius of 16 Å for a single OmpF monomer. For the sake of simplicity and assuming the order-of-magnitude accuracy of the estimation, we have also set the local diffusion constant inside of OmpF equal to an effective constant value, $D(Z) = D_{eff} = 1$ nm^2/ns, for all of the ions, which is smaller than the bulk diffusion of ions (about 3.0 nm^2/ns). Of note, due to the exponential dependence in eq 4, the main contribution to the permeability coefficient comes from differences in the free energy $U(Z)$.

We have shown that recording nanopore I–V curves under asymmetric conditions and fitting the results with the GHK equation gives readily the zero-current potential and thus allows the calculation of the relative permeability for the ions present in solution. In particular, with nanometer sized pores at low mM concentrations of current carrier electrolytes like NaCl, the nanopore permeability of large charged solute molecules like

DOI: 10.1021/acs.jpclett.7b00062
J. Phys. Chem. Lett. 2017, 8, 1295−1301

the β-lactamase inhibitor anions of avibactam, sulbactam, and tazobactam can be screened under tri-ionic conditions using low mM to μM concentrations of the charged large solute molecules. Besides the principal difficulties underlying the GHK constant field theory, which assumes independent movement of the ions through the pores (see refs 9−11, 16 for a detailed discussion), we have demonstrated that the methodology can be used to obtain semiquantitative measures for permeation of charged drugs through nanopores. The method presented can, after a suitable miniaturization and parallelization, serve as a basis for a simple, fast, and sensitive permeability screen of nanopores for charged molecules. As detailed in the Supporting Information for two limiting cases, the sensitivity of the method may be estimated: under bi-ionic conditions, where one of the ions species corresponds to the large molecule in question, a 1.1-fold gradient with down to μM concentration is a realistic lower-resolution limit. Using tri-ionic conditions, at 1 mM carrier electrolyte, a charged compound concentration of 250 μM (cis or trans) would be sufficient to unambiguously detect whether the large ion is permeant or not.

Further dissection of the flux requires calculation of the individual contribution of each ion species to the total flux passing the single channel. Despite the principal difficulties underlying the GHK constant field theory, using this approach, the experimental $I-V$ curves can be divided into the fluxes of the individual ions, which then allows a semiquantitative estimation of turnover numbers for each of the ions. Comparing our bi-ionic and tri-ionic measurements at low concentrations and the respective GHK analysis supports the coarse qualitative consistency of the data, which sanctions our conclusions to be qualitatively valid.

Surprisingly, single-channel conductance of the three investigated inhibitors through OmpF is of the same order of magnitude as with NaCl (see Table S1), indicating an unpredicted high permeability. MD simulations showed that avibactam permeates OmpF by crossing a central barrier, which is due to steric constriction (Figure 4), despite the fact that avibactam is significantly larger than the chloride ion (minimal radius for avibactam is 3.5 Å compared to 1.8 Å for chloride). Different from chloride, avibactam has favorable interactions at the constriction region. Through the alignment of its molecular electric dipole (~13 D) to the transversal electric field generated by the charged residues of OmpF,[17−19] avibactam partially compensates the steric barrier.[20] As shown in Figure 2, the permeation of avibactam is then guided by the diffusion of its sulfate group along the basic ladder while the NH_2 remains in contact with the loop L3. However, the barrier for the chloride, though smaller, is very broad and extends throughout the channel, whereas the barrier for avibactam extends less than 10 Å, only across the constriction region. Mean-field theory clearly expresses the weight of the two parameters of the barrier, height and width, through the integral in eq 4. In the case of avibactam, the higher free-energy barrier is compensated by a smaller width, thus leading overall to a permeability comparable to that of chloride. On the other hand, steric contribution to the central diffusion barrier is negligible in the case of chloride; the extremely broad but low barrier is due to unfavorable desolvation inside of OmpF and electrostatic repulsion with the negative central region.

Homologues of the three major trimeric *E. coli* porins OmpF, OmpC, and PhoE are also found in many other Gram-negative bacteria, such as *P. aeruginosa* and *A. baumannii*.[22] This family of β-barrel membrane pores shares a high degree of structural similarity.[23] Therefore, it is to be expected that our results showing that *E. coli* OmpF has a very high permeability to β-lactamase inhibitors also apply to the homologous OmpF porins from *P. aeruginosa* and *A. baumannii*. In particular, OprF from *P. aeruginosa*, where the high conductance state revealed a larger pore diameter than that of *E. coli* OmpF,[24] is expected to display also high permeability for the three β-lactamase inhibitors. Generally, our results show that the low uptake of β-lactamase inhibitors observed in many cases by OmpF expressing bacteria cannot be attributed to a low transport capacity of OmpF for these compounds. It is interesting to transform the turnover number into a permeability constant P [cm/s]. However, the number of OmpF species in the outer cell wall depends on the growth condition and cell type and cannot be generalized. To give a rough number, we estimate *E. coli* to have about 10^5 OmpF copies and estimate the cell surface to be around 10^{-11} m^2, which results in a permeability constant of about $P = 10^{-1}$ cm/s for a bacterial cell. Obviously, this value is unexpectedly high and about 2 orders above the water permeability across the lipid membrane. One reason for the high permeability might be the absence of LPS. Rather, additional regulatory processes are likely to control the permeation of the β-lactamase inhibitors through the pore of OmpF presumably at the level of protein−protein interactions.

■ ASSOCIATED CONTENT

Supporting Information

The Supporting Information is available free of charge on the ACS Publications website at DOI: 10.1021/acs.jpclett.7b00062.

Planar lipid bilayer and electrical recording, electrophysiological permeation assay method outline, calculation of the avibactam anion turnover through OmpF, extended analysis of single-channel currents of OmpF in the presence of β-lactamase inhibitors, molecular dynamics calculations, and methods (PDF)

■ AUTHOR INFORMATION

Corresponding Author

*E-mail: ri.wagner@jacobs-university.de.

ORCID

Mariano Andrea Scorciapino: 0000-0001-7502-7265
Matteo Ceccarelli: 0000-0003-4272-902X
Richard Wagner: 0000-0001-5472-8097

Author Contributions

M.W. and R.W initiated the idea of reversal potential measurements and supervised I.G. in the work. I.G. performed all of the experiments and analyzed the data with input from M.W. and R.W. L.B. purified the protein. A.P., M.A.S., I.B., and M.C. performed molecular dynamics calculations. I.G., M.W. R.W, and M.C. were involved in writing of the manuscript.

Notes

The authors declare no competing financial interest.

■ ACKNOWLEDGMENTS

The research leading to these results was conducted as part of the TRANSLOCATION consortium and has received support from the Innovative Medicines Initiatives Joint Undertaking under Grant Agreement N°115525, resources which are composed of financial contribution from the European Union's seventh framework program (FP7/2007-2013) and EFPIA companies in kind contribution.

DOI: 10.1021/acs.jpclett.7b00062
J. Phys. Chem. Lett. 2017, 8, 1295−1301

REFERENCES

(1) Edel, J.; Oh, S. H. From Nanopores to Nanochannels. *Analyst* **2015**, *140*, 4732.

(2) Albrecht, T.; Edel, J. B.; Winterhalter, M. New Developments in Nanopore Research from Fundamentals to Applications. *J. Phys.: Condens. Matter* **2010**, *22*, 450301.

(3) Howorka, S.; Siwy, Z. Nanopore analytics: sensing of single molecules. *Chem. Soc. Rev.* **2009**, *38*, 2360−2384.

(4) Deamer, D.; Akeson, M.; Branton, D. Three decades of nanopore sequencing. *Nat. Biotechnol.* **2016**, *34* (5), 518−524.

(5) Hajjar, E.; Mahendran, K. R.; Kumar, A.; Bessonov, A.; Petrescu, M.; Weingart, H.; Ruggerone, P.; Winterhalter, M.; Ceccarelli, M. Bridging Timescales and Length Scales: From Macroscopic Flux to the Molecular Mechanism of Antibiotic Diffusion through Porins. *Biophys. J.* **2010**, *98*, 569−575.

(6) Nikaido, H. Molecular basis of bacterial outer membrane permeability revisited. *Microbiology and molecular biology reviews* **2003**, *67* (4), 593−656.

(7) Payne, D. J.; Gwynn, M. N.; Holmes, D. J.; Pompliano, D. L. Drugs for bad bugs: confronting the challenges of antibacterial discovery. *Nat. Rev. Drug Discovery* **2007**, *6* (1), 29−40.

(8) Stavenger, R. A.; Winterhalter, M. TRANSLOCATION project: how to get good drugs into bad bugs. *Sci. Transl. Med.* **2014**, *6* (228), 228ed7−228ed.

(9) Hille, B. *Ionic Channels of Excitable Membranes*; Sinauer Associates, Inc.: Sunderland, MA, 2001; Vol. 3.

(10) Harsman, A.; Schock, A.; Hemmis, B.; Wahl, V.; Jeshen, I.; Bartsch, P.; Schlereth, A.; Pertl-Obermeyer, H.; Goetze, T. A.; Soll, J.; et al. OEP40, a Regulated Glucose-permeable β-Barrel Solute Channel in the Chloroplast Outer Envelope Membrane. *J. Biol. Chem.* **2016**, *291* (34), 17848−17860.

(11) Wagner, R.; Schmedt, D.; Hanhart, P.; Walter, C.; Meisinger, C.; Bartsch, P. Mitochondrial Protein Import Channels. *Electrophysiology of Unconventional Channels and Pores*; Springer, 2015; pp 33−58.

(12) Danelon, C.; Suenaga, A.; Winterhalter, M.; Yamato, I. Molecular Origin of the Cation Selectivity in OmpF Porin. Single Channel Conductances versus Free Energy Calculation. *Biophys. Chem.* **2003**, *104*, 591.

(13) López, M. L.; García-Giménez, E.; Aguilella, V. M.; Alcaraz, A. Critical assessment of OmpF channel selectivity: merging information from different experimental protocols. *J. Phys.: Condens. Matter* **2010**, *22* (45), 454106.

(14) Syganow, A.; Von Kitzing, E. (In) validity of the constant field and constant currents assumptions in theories of ion transport. *Biophys. J.* **1999**, *76* (2), 768−781.

(15) Corry, B.; Kuyucak, S.; Chung, S.-H. Tests of Continuum Theories as Models of Ion Channels. II. Poisson−Nernst−Planck Theory versus Brownian Dynamics. *Biophys. J.* **2000**, *78* (5), 2364−2381.

(16) Moy, G.; Corry, B.; Kuyucak, S.; Chung, S.-H. Tests of continuum theories as models of ion channels. I. Poisson− Boltzmann theory versus Brownian dynamics. *Biophys. J.* **2000**, *78* (5), 2349−2363.

(17) Acosta-Gutierrez, S.; Scorciapino, M. A.; Bodrenko, I.; Ceccarelli, M. Filtering with Electric Field: the Case of E. Coli Porins. *J. Phys. Chem. Lett.* **2015**, *6*, 1807−1812.

(18) Acosta-Gutierrez, S.; Bodrenko, I.; Scorciapino, M. A.; Ceccarelli, M. Macroscopic Electric Field Inside Water-Filled Biological Nanopores. *Phys. Chem. Chem. Phys.* **2016**, *18*, 8855−8864.

(19) Kumar, A.; Hajjar, E.; Ruggerone, P.; Ceccarelli, M. Structural and dynamical properties of the porins OmpF and OmpC: insights from molecular simulations. *J. Phys.: Condens. Matter* **2010**, *22*, 454125.

(20) Scorciapino, M. A.; Acosta-Gutierrez, S.; D'Agostino; Malloci; Samanta; Bodrenko; Ceccarelli; Benkerrou, D. Rationalizing the Permeation of Polar Antibiotics into Gram-negative Bacteria. *J. Phys.: Condens. Matter* **2017**, *29*, 113001.

(21) Amodeo, G. F.; Scorciapino, M. A.; Messina, A.; De Pinto, V.; Ceccarelli, M. Charged Residues Distribution Modulates Selectivity of the Open State of Human Isoforms of the Voltage Dependent Anion-Selective Channel. *PLoS One* **2014**, *9*, e103879.

(22) Pages, J. M.; James, C. E.; Winterhalter, M. The Porin and the Permeating Antibiotic: a Selective Diffusion Barrier in Gram-Negative Bacteria. *Nat. Rev. Microbiol.* **2008**, *6*, 893−903.

(23) Masi, M. Structure, Function and Regulation of Outer Membrane Proteins Involved in Drug Transport in Enterobactericeae: the OmpF/C−TolC case. *Open Microbiol. J.* **2013**, *7*, 22−33.

(24) Nestorovich, E. M.; Sugawara, E.; Nikaido, H.; Bezrukov, S. M. Pseudomonas Aeruginosa Porin OprF Properties of the Channel. *J. Biol. Chem.* **2006**, *281*, 16230−16237.

DOI: 10.1021/acs.jpclett.7b00062
J. Phys. Chem. Lett. 2017, 8, 1295−1301

A General Method to Determine the Flux of Charged Molecules through Nanopores Applied to ß-Lactamase Inhibitors and OmpF

Supplemental Information

Ishan Ghai,[1] Alessandro Pira,[2] Mariano Andrea Scorciapino,[3] Igor Bodrenko,[2] Lorraine Benier,[1] Matteo Ceccarelli,[2] Mathias Winterhalter,[1] Richard Wagner[1]*

[1]Department of Life Sciences and Chemistry, Jacobs University Bremen, 28719 Bremen, Germany

[2]Department of Physics, University of Cagliari, Cagliari, Italy.

*Corresponding author E-mail: ri.wagner@jacobs-university.de

SUPPORTING INFORMATION

Content:

Materials and Methods

Materials:

Avibactam Sodium. was a gift from AstraZeneca USA, Sulbactam and Tazobactam sodium was obtained from Cayman chemicals USA, Dextran sulfate sodium pharma grade molecular weight 8000 g/mol and Sodium chloride was obtained from Sigma Aldrich Germany, 1,2-diphytanoyl-sn-glycero-3-phosphocholine was procured from Avanti Polar Lipids (Alabaster, AL) and all other chemicals used were procured from AppliChem,

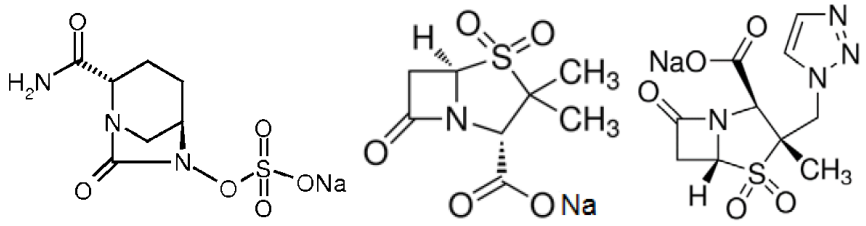

A). Avibactam Na B). Sulbactam Na C). Tazobactam Na

Figure S1. A). Avibactam Sodium, Molecular weight 288 Da. Molecular Formula $C_7H_{10}N_3NaO_6S$. B). Sulbactam Sodium, Molecular weight 255.5 Da. Molecular Formula $C_8H_{10}NNaO_5S$. C). Tazobactam sodium, Molecular weight 322.5 Da. Molecular Formula $C_{10}H_{11}N_4NaO_5S$.

Methods:

Planar Lipid Bilayer and Electrical Recording:

Planar lipid bilayer according to Montal and Mueller were formed as described in detail[1] Briefly, an aperture in a Teflon septum with a diameter of 80–120 μm was prepainted with hexadecane dissolved in n-hexane at 1-3% (v/v) and the chambers were dried for 20-25 min, in-order to remove the solvent. Bilayers were made with 1,2- diphytanoyl-sn-glycerophosphocholine at a concentration of 5 mg/ml in n-pentane. Stock solutions of the outer membrane porin OmpF (0.3-0.5μl 2mg-3mg protein/ml) was added to the cis side for all the measurements. Standard Ag/AgCl or calomel electrodes were used to detect the ionic current. Note that under asymmetric condition we used either homemade salt bridges or commercial calomel electrodes (Metronom). The cis side electrode of the cell was grounded, whereas the trans side electrode was connected to the headstage of an Axopatch 700B amplifier, used for the conductance measurements in the voltage clamp mode. Signals were filtered by an on board low pass Bessel filter at 10 kHz and recorded onto a computer hard drive with a sampling frequency of 50 kHz. Analysis of the current recordings was performed using Clampfit (Axon Instruments). The current voltage relation of the individual experiments was calculated from single averaged currents at the given voltage. All the experiments were repeated three times minimum. Standard solutions contained HEPES 1mM, pH 6, salts and the ß-lactamase-inhibitors at the concentrations given in the (Tables S1). The relative permeability of cations vs inhibitor anions in the bi-ionic case ($P_{Na^+}/P_{inhibitor^-}$) and in the tri-ionic case ($P_{Na^+}/P_{Cl^-}/P_{inhibitor^-}$) were obtained by fitting of the experimental I-V-curves with the Goldman-Hodgkin-Katz current equation[2] but see below for more details.

OmpF conductance under symmetrical low salt bi-ionic conditions

	Inhibitor/salt 30mM (cis/trans)	$\bar{G}_{trimer}$ **(pS) trimer**
OmpF	Avibactam-Na	270 pS ± 60 (n=15)
	Sulbactam-Na	240 pS ± 40 (n=27)
	Tazobactam-Na	240 pS ± 50 (n=36)
	NaCl	270 ± 60 (n=40)
	100 mM NaCl (cis/trans)	960 ±250 (n=10)
OmpF Simulations	NaCl	190± 30 (n=4x200ns)

Table S1: Experimental and calculated conductance of an OmpF-trimer at low ionic strength under bi-ionic conditions, beside the indicted inhibitor or salt concentrations the buffer contained 20 mM HEPES pH 6. Calculated conductance of an OmpF-trimer at corresponding low ionic strength under bi-ionic conditions. V=100 mV and 200 mV respectively for MD modeling.

Electrophysiological permeation assay: Method-Outline

We are interested in obtaining information on the selectivity of the membrane transport of charged antibiotics which are however mostly available in limited quantities and therefore can only be used in trace amounts or lower mM concentrations. To resolve this issue, we apply an experimental setup where a combination of symmetric salt at low concentrations on both sites of the membrane are supplemented with low concentrations of an antibiotic at one site of the membrane (tri-ionic conditions). This setup allows with large pore channels for single channel currents in the range $\ll 100\ pA$ which however can be experimentally resolved.

Assuming single channel recording from a bilayer with an arbitrary channel having the following arbitrary properties:

Permeability: $P_{Na^+} = 4;\ P_{Cl^-} = -1.0;\ P_{AB^-} = 1.0;$

Cation: $z_{Na^+} = 1;\ c_{Na^+cis} = 60\ mM;\ c_{Na\ trans} = 10\ mM$

Anion: $z_{Cl^-} = -1.0;\ c_{Cl^-cis} = 10mM;\ c_{Cl^-trans} = 10mM$

Effector: $z_{AB} = -1.0;\ c_{AB^-cis} = 50mM;\ c_{AB^-trans} = 00mM$

Zero current potential: $V_{rev} = 21.0\ mV\ (experimental\ value)$

Considering that the assumptions of the GHK-theory are valid and the ion fluxes considered to be independent [2] we can calculate the expected current voltage relation for the above membrane channel for any combination of the bi -or tri-ionic concentrations (see Figure S2):

1. $I_{Na^+}(V) = I(V, P_{Na^+}, z_{Na^+}, c_{Na^+cis}, c_{Na^+trans})$,
2. $I_{CL^-}(V) = I(V, P_{Cl^-}, z_{Cl^-}, c_{Cl^-cis}, c_{Cl^-trans})$
3. $I_{AB^-}(V) = I(V, P_{AB^-}, z_{AB^-}, c_{AB^-cis}, c_{AB^-trans})$
4. $\sum I(V) = I_{Na^+}(V) + I_{Cl^-}(V) + I_{AB^-}(V)$

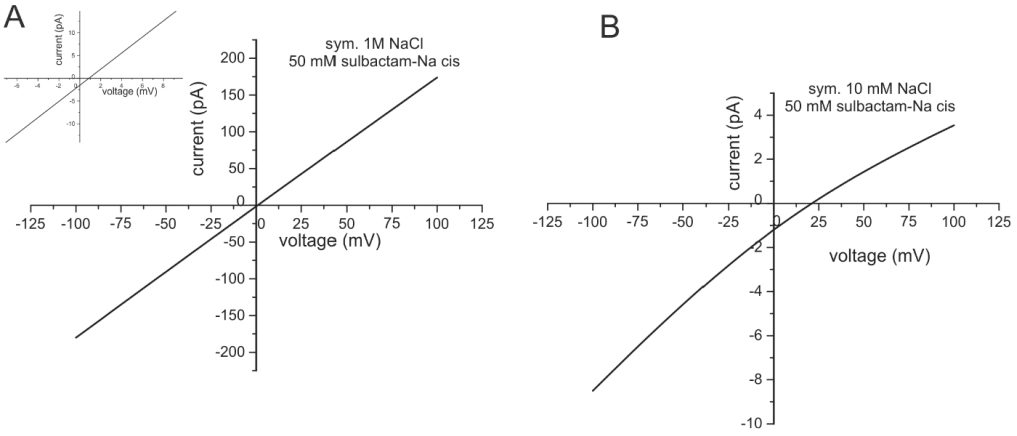

***Figure S2**: (A) Example for a calculated i-v curve for an arbitrary channel with the above detailed properties with 1M NaCl (cis/trans and cis 50 mM of a charged antibiotic AB with a net charge of -$z_{SB} = -1$. (right)(V_{rev}=0.7mV.) (B) Same as left but with 10 mM NaCl (cis/trans) (V_{rev}=21.3mV)*

For many antibiotic, the solubility is rather limited. As seems in (Figure S2 (A)) 1M NaCl (cis/trans) will mask the change in the reversal potential induced by a 50-mM antibiotic gradient. For an antibiotic concentration of 50 mM (cis) and the conditions above but with 10 mM NaCl (cis/trans) we calculate a $V_{rev} = 21.3\ mV$ a value which can easily be resolved. Straight forward, if under the above described experimental conditions the relative permeability of a channel for the small ions e.g. (P_{K^+}/P_{Cl^-}) are known and the reversal potential in the additional presence of the antibiotic at a single side has been experimentally

determined it is possible to calculate the relative permeability for the 3 ions ($P_{Na^+} : P_{Cl^-} : P_{AB^-}$) according to the GHK current equation (equation 4) [2].

Sensitivity Limits

Bi-ionic case: In this case V_{rev} is only dependent on the concentration gradient and (P_{cation^+}/P_{anion^-}). However, it is important to note that calomel electrodes are required for the experimental set up since no chloride ions are present in solution.

Considering the case of sulbactam-Na (Figure 1E, Table 2) we observed $V_{rev} = 14{,}3$ (gradient: $\Delta c_{(cis)/trans)}(\frac{80mM}{30mM}) = 2.67$). With the value for $\frac{(P_{Na^+}}{P_{sulbactam^-}} = 4{:}1$ from (Table 2) and an realistic experimental resolution of $\Delta V_{rev} = 1{,}5\ mV$ we end at limiting gradient of Δc =1:1.1.

Tri-ionic Case: In this case classical Ag^+/AgCl electrodes can be used and the reversal potential depends on the concentration of the carrier ions and the concentration of the sulbactam anion at either side of the membrane. Considering again the tri-ionic case of sulbactam-Na (Figure 1B, Table 2) $c_{(cis)} = 50mM$, with 10mM NaCl cis/trans and the experimental $V_{rev} = 21.8$. Taking the permeability values given in (Table 3) but with 1mM NaCl (cis/trans) a concentration of $c_{(cis)} = 250\mu M$ would result in $\Delta V_{rev} = 1{,}5\ mV$ the experimental resolution limit.

Calculation of the Avibactam-anion turnover through OmpF

In order to calculate the turnover number of the avibactam anion through the OmpF pore we used the following data:

(Figure S3A): At a cis/trans 80/30 mM Na-Avibactam gradient: $\frac{P_{avibactam^-}}{P_{Na^+}} = 0.25$ (Table2). Single pore conductance: G_{sp}=90 pS (Avibactam sym. 30mM, cis/trans) (Table 1).

(Figure S3B): At a cis/trans 10/1 µM Na-Avibactam gradient: $\frac{P_{avibactam^-}}{P_{Na^+}} = 0.25$. Single pore conductance $\overline{G}_{sp} = 5.6 \cdot 10^{-2}\ pS$. This value was obtained from a Hill plot of the concentration dependence of the OmpF channel conductance for avibactam-Na extrapolated to 10µM avibactam-Na (details not shown).

Using equation (1-4 main text) the relative contributions of the avibactam anion and the Na^+ cation to the total current can be calculated for a single pore and the currents normalized to

the respective $\bar{G}_{sp}$ give the corresponding current voltage relations at the specified ionic conditions (Figure S3A,B).

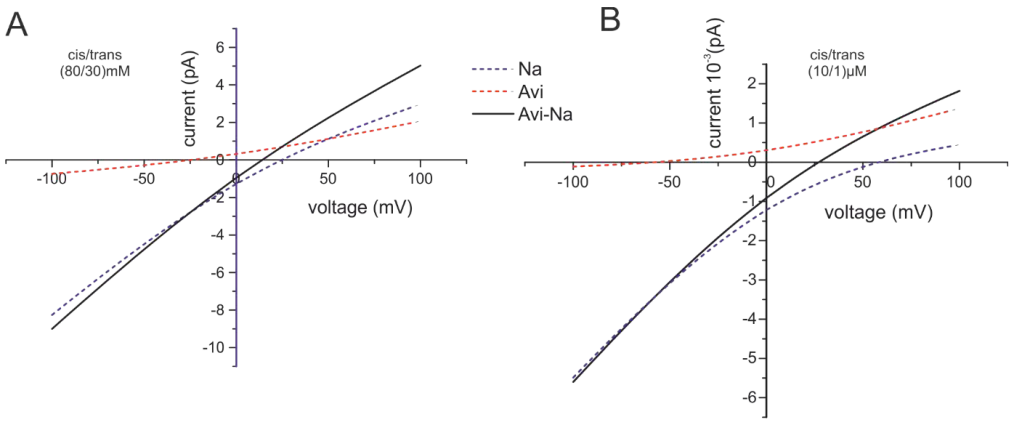

Figure S3: (A) Calculated current voltage relation according to equation (1-4 main text) for a single OmpF channel pore in 80/30 mM Na-Avibactam, using the experimental determined values for $\frac{P_{AB^-}}{P_{Na^+}}$ and $\bar{G}_{trimer}$. Dissected current contributions of the avibactam anion (red dots) and the sodium cation (blue dots). (B) Same as (A) but for 10/1 µM avibactam-Na (cis/trans)

For the avibactam anion current at V_m = 0 mV (Figure S3B) we obtain i = 0.001 pA (trimer) the anion flux through a single OmpF pore at the given gradient of Δc=10:1 can be calculated as follows:

$$5. \qquad n = \frac{i \cdot N_A}{F} = \frac{0.001/3 \cdot 10^{-12} \cdot 6.022 \cdot 10^{23}}{964853} = 208\ molecules/s$$

Extended analysis of single channel currents of OmpF in the presence of ß-lactamase-inhibitors

Addition of 10 mM Na-Avibactam (cis) to a bilayer containing a single trimeric OmpF channel did not cause any significant change in the channel gating frequencies and current amplitudes (Fig S4 A and B). OmpF gating with 30 mM (cis/trans) Tazobactam (Figure S7) and Sulbactam (Figure S6) shows, even at 10 kHz time resolution, no significant detectable gating events while the channels remained in the fully open states. Statistical analysis of current traces showed in the case of Avibactam distinct spaced current amplitude patterns of cumulative fast events (see Figure S4E) which presumably are representative for non-

complete time resolved fast gating transitions. Frequency analysis of the electrical current recordings did not give any additional information on the channel gating in the presence of Tazobactam-Na. While OmpF current recordings with 30 mM (cis/trans) Sulbactam showed only rare detectable gating events and all channel pores remained in the fully open states, thus the OmpF channel recordings in the presence of the ß-lactamase inhibitors do not directly provide information on the fluxes of these compounds through the channel. Therefore, from these types of measurements no enlightenment on the permeability of the ß-lactamase anions through OmpF can be obtained.

The three applied ß-lactamase inhibitors showed different effects on the OmpF channel currents.

Since single channel incorporation into the planar bilayer is, particularly at low ionic strength, hardly to achieve we used bilayers containing multiple copies of the trimeric OmpF to analyze the channel properties of single OmpF pores in the presence of the ß-lactamase inhibitors under bi-ionic conditions.

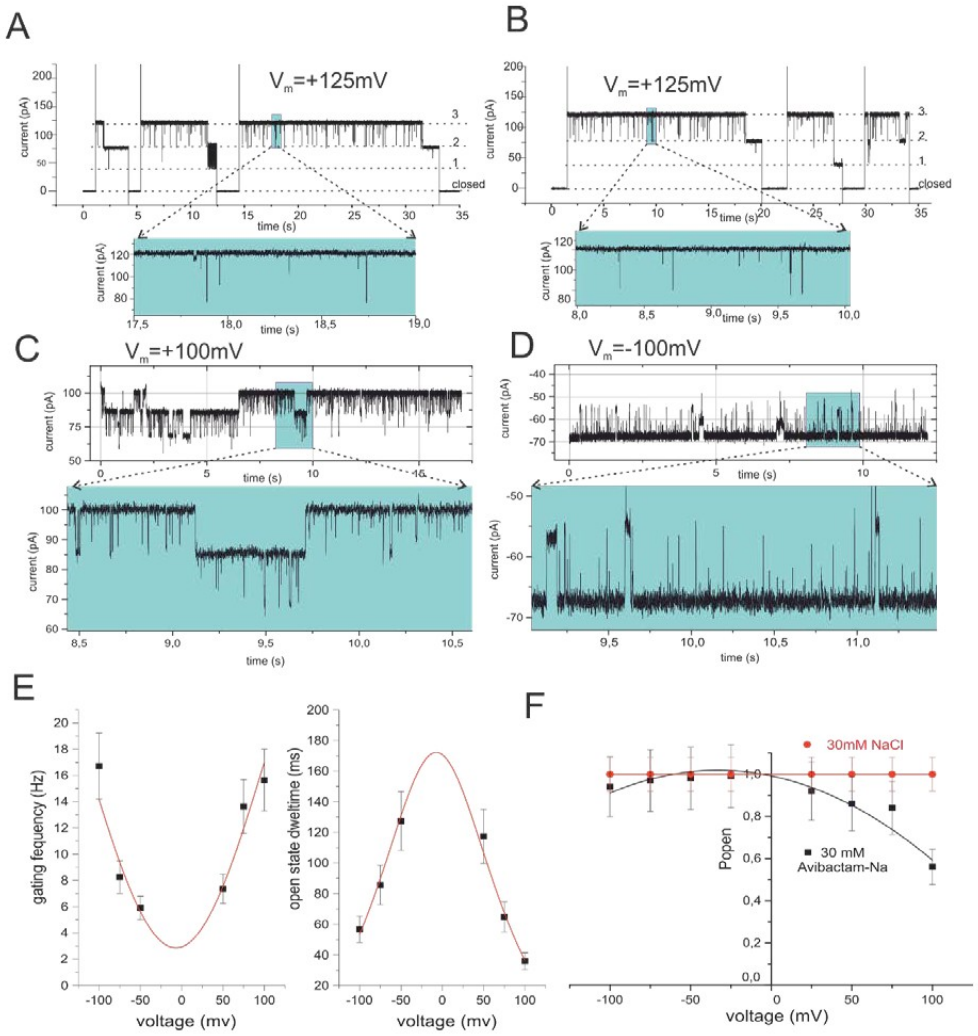

Figure S4: (A, B) Single channel current recording from a bilayer with a single active OmpF channel in 100mM NaCl cis/trans, 20mM HEPES pH 6,0 and applied voltage of V_m=+125mV in absence (A) and presence of 20 mM Na-Avibactam added on cis sides (B). C and D show current recording from a bilayer containing 3 active trimeric OmpF channels in 30mM Na-Avibactam cis/trans, 1mM HEPES pH 6,0 and applied voltage of V_m=+100mV (C) and V_m=-100mV (D). (E) Gating frequency (left) and open state dwell times (right) calculated from current recordings of OmpF containing bilayers in 30mM Na-Avibactam cis/trans, 1mM HEPES pH 6,0, at the indicated V_m (data are mean of 3 independent recordings). (F) Open

probability of a single OmpF channel pore in symmetrically 30/30 mM NaCl (cycles) and 30/30 mM Na-Avibactam, 1mM HEPES pH 6,0..

Avibactam (Figure S5)

Gating of OmpF in the presence Avibactam reveals rare longer closing events in the ms time range mainly at higher V_m and for only parts of the trimeric OmpF pores (Figure S4 E, F). However, the frequency and inter events closing event times occurred random and were neither dependent on the membrane potential nor on the Na-Avibactam concentration. The analysis of the single pore currents (Figure S4 A-F) and the current voltage relation (Figure S5C) revealed that the bilayer contained 4 active trimeric OmpF channels. While the single channel pore conductance in the presence of symmetrical 30 mM Na-Avibactam was G_{sp} = 90 pS (Figure S5E). The effected trimeric OmpF channel remained mainly in the three pores open state even at higher V_m and the channel open probability in the presence of avibactam decreased slightly at higher positive voltages when the Avibactam anion was forced to enter the pore (Figure4F).

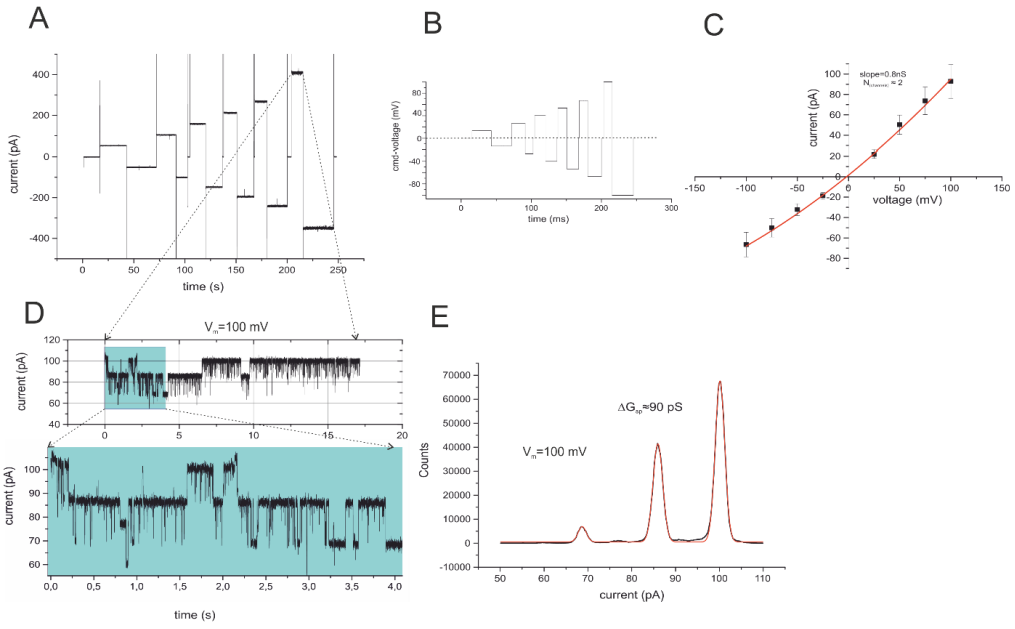

Figure S5: Current recordings from a bilayer containing three active trimeric OmpF channels in the presence of symmetrical 30 mM Na-Avibactam (A): Current recordings of OmpF with symmetrical 30 mM Na-Avibactam. (B) Timeline of the applied voltage steps. (C) Current voltage relation obtained from (A). (D) Expansion of

the current trace at Vm=100 mV (from A). (E) Current amplitude histogram at V_m=100 mV (from A).

Sulbactam (Figure S6)

Current recordings from OmpF containing bilayers in the presence of symmetrical 30mM Na-Sulbactam show almost no detectable gating events and the channels remained in the fully open states (Figure S6 A,D). The analysis of the single pore currents (Figure S6D) and the current voltage relation (Figure S6C) revealed that the bilayer contained 9 active trimeric OmpF channels. While the sing channel pore conductance in the presence of symmetrical 30 mM Na-Avibactam was $G_{sp} = 80$ pS (Figure S5E).

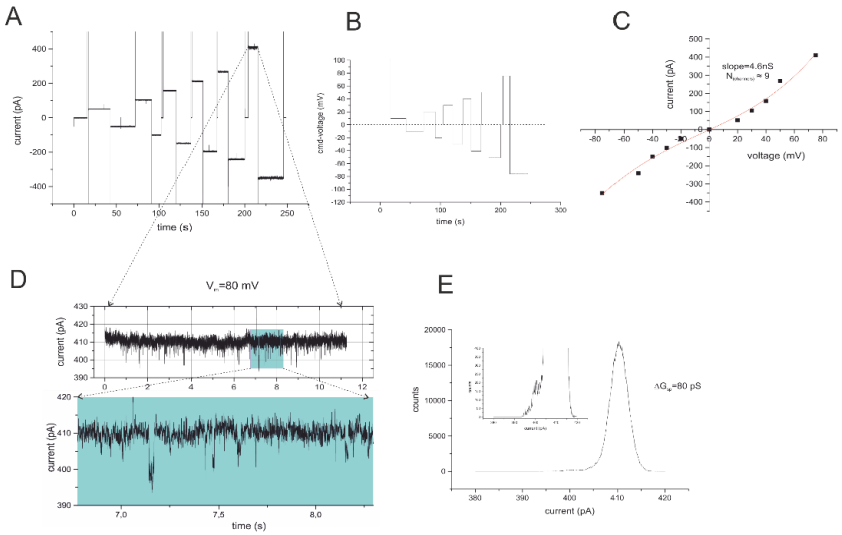

Figure S6: Current recordings from a bilayer containing nine active trimeric OmpF channels in the presence of symmetrical 30 mM Na- Sulbactam

(A): Current recordings of OmpF with symmetrical 30 mM Na-Sulbactam. (B) Timeline of the applied voltage steps. (C) Current voltage relation obtained from (A). (D) Expansion of the current trace at Vm=100 mV (from A). (E) Current amplitude histogram at V_m=100 mV (from A)

Tazobactam (Figure S7)

Current recordings from OmpF containing bilayers in the presence of symmetrical 30mM Na-Tazobactam did not show clearly resolvable 10 kHz gating events of single pores and the channels remain in the fully open states (Figure S7A, C). However statistical histogram analysis of current traces (Figure S7F) shows distinct spacing patterns of cumulative fast current amplitude events which presumably are representative for non-complete resolved fast gating transitions. Frequency analysis unfortunately does not provide any additional information. The analysis of the distinct spacing patterns of cumulative fast current amplitude events (Figure S7F) and the current voltage relation (Figure S7D) revealed that the bilayer contained 5 active trimeric OmpF channels. While the single channel pore conductance in the presence of symmetrical 30 mM Na-Tazobactam was $G_{sp} = 80$ pS (Figure S7F).

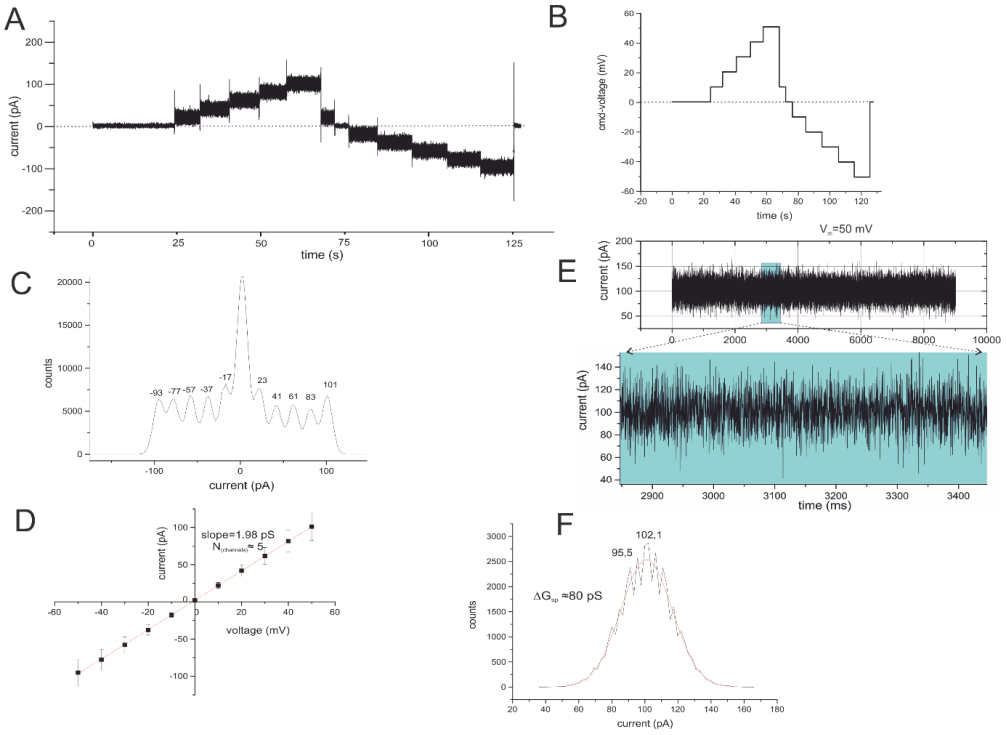

Figure S7: Current recordings from a bilayer containing five active trimeric OmpF channels in the presence of symmetrical 30 mM Na-Tazobactam

(A): Current recordings of OmpF with symmetrical 30 mM Na-Tazobactam. (B) Timeline of the applied voltage steps. (C) All voltage-current amplitude histogram

from (A). (D) Current voltage relation obtained from (A). (E) Expansion of the current trace at V_m=80 mV (from A). (F) Current amplitude histogram at V_m=80 mV (from A).

NaCl (Figure S8)

Current recordings from OmpF containing bilayers in the presence of symmetrical 30mM NaCl show clearly detectable gating events (Figure S10 A, B). The analysis of the single pore currents (Figure S8 A) with the current voltage relation (data not shown) and the current histogram for single pore gating (Figure S8 B) revealed that the bilayer contained 11 active trimeric OmpF channels. While the single channel pore conductance in the presence of symmetrical 30 mM NaCl was $G_{sp} = 88$ pS (Figure S8 B).

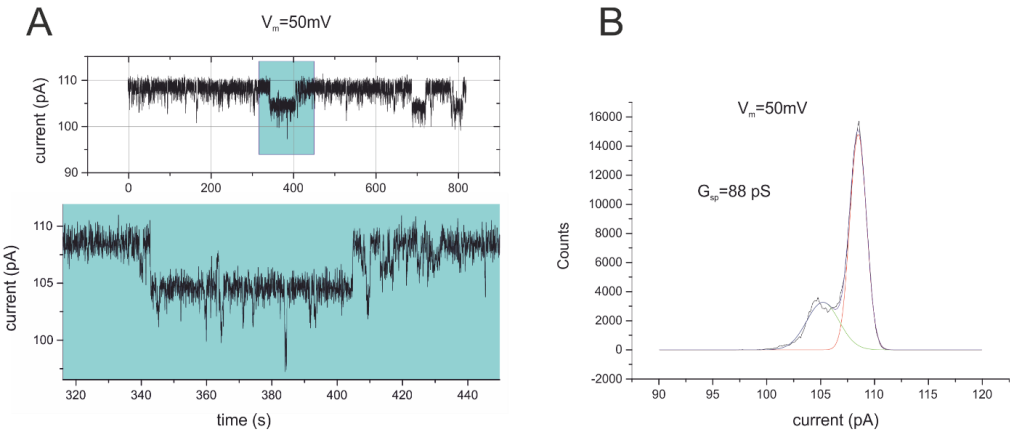

Figure S8: Current recordings from a bilayer containing 11 active trimeric OmpF channels in the presence of symmetrical 30 mM NaCl (A): Current recordings of OmpF with symmetrical 30 mM NaCl. (B) Current amplitude histogram at V_m=50 mV (from A).

Methods: Molecular dynamics simulations

We started from the OmpF structure (PDB ID: 2OMF; 2.4Å resolution) simulated in reference[3]. Briefly, the system was simulated in condition of neutral pH with all amino acid residues in their charged state but for the E296, which was protonated[4]. The OmpF trimer was embedded in a pre-equilibrated POPC (1-palmitoyl-2-oleoyl-sn-glycero-3-phosphocholine) bilayer of 259 lipids. The system was oriented in order to center the protein at the origin of the coordinate system and align the channel along the Z-axis where Z positive values refers to the extracellular vestibule (EV) and Z negative values refers to the periplasmic vestibule (PV).

Thus, the system was equilibrated in vacuum to fill in the gaps. Finally, the system was solvated with ~17000 water molecules and the total number of atoms was ~100k in a box with edges size 11, 11 and 9 nm. A number of potassium and chloride ions were added to have a 0.2 M KCl solution. An excess of K^+ was required to neutralize the negative charges of the trimer (-33 e).

After 1 ps of energy minimization (conjugate gradients), a slow heating from 10 to 300 K was carried out for 1 ns with positional restraints on the Cα protein along three dimensions and on the lipids phosphorus atoms along z only, allowing movement on XY plane. After releasing the constraints, an equilibration stage follows for 4 ns in the NPT ensemble at 1.0 bar and 300 K. Finally, 400 ns MD simulations were performed in the NVT ensemble after the elimination of the protein restraints. Only the last 300 ns were used for the analysis.

Production run in the NVT ensemble was performed through the ACEMD code[5] compiled for GPUs, by rescaling hydrogen mass to 4 au and increasing the time-step up to 4.0 fs. The Langevin thermostat (300 K) was used with 0.1 ps damping time and the particle mesh Ewald (PME) method with 9 Å cut-off for electrostatic interactions. The Amber99sb-ildn force field parameters were used for OmpF, the General Amber Force Field (GAFFlipid) for POPC[6], and the TIP3P model for waters[7]. For Avibactam we used the GAFF approach as described in ref [8]. The three inhibitors were placed above the first monomer in the EV about 20 Å away the constriction region (CR) in the final configuration from the OmpF simulation.

Substrates permeation was investigated using well-tempered meta dynamics simulations with Plumed 2.2 plug-in[9] within the ACEMD software[5]. This method consists in adding Gaussian weight factors that are periodically rescaled providing a convergence parameter to monitor during the meta dynamics simulation[10,11].

A first step of normal metadynamics simulation of inhibitor permeation was performed until the first effective translocation through the protein constriction region (CR) was observed. Then, four configurations were selected, two with the inhibitor located in the extracellular vestibule (EV), and two in the periplasmic vestibule (PV). Correspondingly, four multiple-walkers[12] were set to extend the well-tempered metadynamics reconstruction of the free-energy surface (FES).

The substrates 'position Z' defined as the difference of the z-coordinate between the center of mass (com) of the substrate and that of the porin first monomer (related to Cα) and the 'orientation Φ' of substrate molecular dipole moment related to z component were used as

biased collective variables. Each walker was run for at least 4x450 ns that correspond to a total simulation time of 1.8 μs. During the metadynamics, energy biases were added every 5.0 ps to each collective variable (initial height 1.0 kcal/mol; Δ=5 degree and 0.4 Å for orientation and position, respectively). Well-tempered ΔT was 4800 K (bias factor = 16). Each walker adds its own biases, but it also reads those added by the other walkers, thus accelerating the sampling of the whole space. The one-dimensional free energy surfaces of inhibitors of (Figure. S9) were obtained integrating out the collective variable orientation.

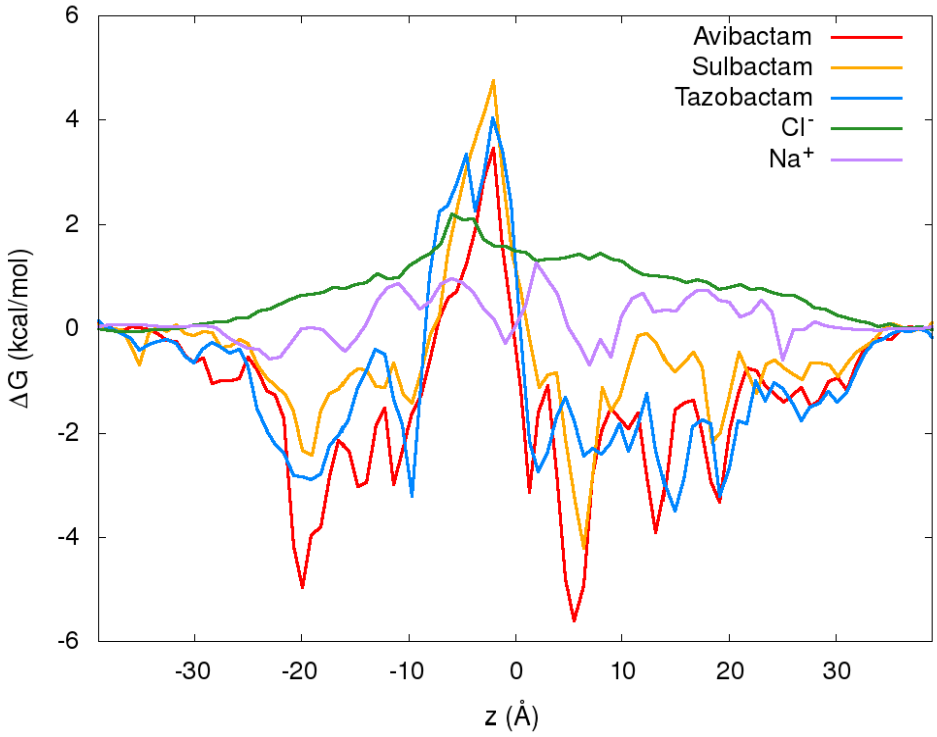

Figure S9: FES reconstructed with metadynamics simulation for the three inhibitors through OmpF, by using two collective variables, namely, molecular dipole orientation and z-coordinate (position along the channel axis). We showed the FES only along the Z coordinate for a comparison with the free energy of ions, calculated with their relative density with respect to the bulk, 200 mM.

Molecular dynamics simulations on the permeation of ions in presence of avibactam

In order to investigate the ion conductance through the trimeric porin, an external electric field was applied using the in-built plugin in ACEMD[5]. A constant force is applied at each atom in the system having a point charge. A representative configuration of the avibactam inhibitor from the minimum found in FES near the constriction region was taken out from

meta dynamics trajectories; 100 steps of energy minimization were performed followed by 10 ns of standard MD simulation equilibration step. Starting from last coordinates obtained by the simulation just described, two different 50 ns simulations were run with external electric field and used as further equilibration step: the first one corresponds to an applied potential of 200 mV and the second one corresponds to an applied potential of -200 mV. Finally, final configurations obtained by both trajectories were used as starting point to run 5 independent simulations for each applied potential. Each simulation was run for 100 ns.

In order to compare the calculated conductance for the systems described above with respect to the case without substrate, an external electric field corresponding to an applied potential of 200 mV and -200 mV were applied to the "empty" system. For each case the first 100 ns MD simulation were used as equilibration step, then 5 independent steps of 100 ns MD simulations were run for both selected applied potential, see (Table S2).

	Without Avibactam			**With Avibactam**		
Empty	**G(pS)**	**K^+/Cl^-**	**Ratio**	**G(pS)**	**K^+/Cl^-**	**Ratio**
1	**830**	**70/36**	**2.0**	**930**	**98/14**	**7.0**
2	**1000**	**96/31**	**3.1**	**970**	**100/22**	**4.6**
3	**860**	**86/24**	**3.4**	**1160**	**107/28**	**3.8**
4	**860**	**78/27**	**2.9**	**870**	**94/19**	**5.0**
5	**830**	**82/27**	**3.0**	**1010**	**101/25**	**4.1**
Average	**880±70**		**2.9**	**990 ±100**		**4.9**
Average K+	**660±70**			**820±60**		
Average Cl-	**210±30**			**170±40**		

Table S2: Conductance and potassium/chloride ratio for the independent standard OmpF MD simulations in presence of 200 mM KCl, without and with avibactam, at 200mV external potential.

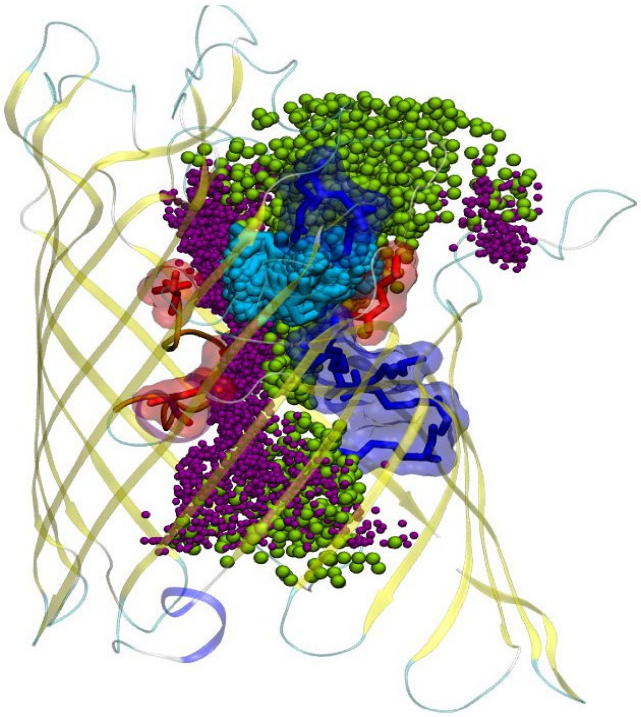

Figure. S10: Avibactam (cyan) at positive voltages blocks the chloride path by superimposing to them (green) without affecting the potassium path (violet). The position of avibactam corresponds to the purple minimum of Figure. 2.

References

1. Montal, M. & Mueller, P. Formation of Bimolecular Membranes from Lipid Monolayers and a Study of their ElectricalProperties. Proceedings of the National Academy of Sciences **69,** 3561–3566 (1972).
2. Hille, B. Ionic Channels of Excitable Membranes, Sinauer Ass. Inc., Sunderland, Ma 01375 (2001)
3. Acosta-Gutierrez, S., Scorciapino, M. A., Bodrenko, I. & Ceccarelli, M. Filtering with Electric Field: The Case of E. coli Porins. J Phys Chem Lett **6,** 1807–1812 (2015).
4. Varma, S., Chiu, S.-W. & Jakobsson, E. The Influence of Amino Acid Protonation States on Molecular Dynamics Simulations of the Bacterial Porin OmpF. Biophys J **90,** 112–123 (2006).
5. Harvey, M. J., Giupponi, G. & De Fabritiis, G. ACEMD: Accelerating Biomolecular Dynamics in the Microsecond Time Scale. J Chem Theory Comput **5,** 1632–1639 (2009).
6. Lindorff-Larsen, K. et al. Improved Side-Chain Torsion Potentials for the Amber ff99SB Protein Force Feld. Proteins **78,** 1950–1958 (2010).
7. Jorgensen, W. L., Chandrasekhar, J., Madura, J. D., Impey, R. W. & Klein, M. L. Comparison of Simple PotentialFunctions forSimulating Liquid Water. J Chem Phys **79,** 926 (1983).
8. Malloci, G. et al. A Database of Force-Field Parameters, Dynamics, and Properties of

Antimicrobial Compounds. Molecules **20,** 13997–14021 (2015).
9. Bonomi, M., Barducci, A. & Parrinello, M. Reconstructing the Equilibrium Boltzmann Distribution from Well-Tempered Metadynamics. Journal of Computational Chemistry **30,** 1615–1621 (2009).
10. Barducci, A., Bussi, G. & Parrinello, M. Well-Tempered Metadynamics: A Smoothly Converging and Tunable Free-Energy Method. Phys Rev Lett **100,** 1–4 (2008).
11. Laio, A. & Parrinello, M. Escaping free-energy minima. Proc. Natl. Acad. Sci. U.S.A. **99,** 12562–12566 (2002).
12. Raiteri, P., Laio, A., Gervasio, F. L., Micheletti, C. & Parrinello, M. Efficient Reconstruction of Complex free Energy Landscapes by Multiple Walkers Metadynamics. The Journal of Physical Chemistry. B, Condensed Matter, Materials, Surfaces, Interfaces & Biophysical **110,** 3533–3539 (2006).

3.3 Physico-Chemical Features of Substrates

After the analysis aimed at comparing the physico-chemical properties of the different porins (paragraph 3.1), a new challenge has been undertaken with the aim of understanding how differences in chemical structure of the substrates play a role in the translocation process through porins. Molecular physico-chemical features like net charge, dipole moment, minimal projection area (mpa) and van der Waals volume, together with their structural flexibility, that modulates these observables, could be parameters that allow predicting substrates behavior into protein channels. Following the protocol described in the paragraph 2.6, the β-lactamase inhibitors reported in figure 3.11 were analyzed and the above mentioned physico-chemical properties were calculated. Dipole moments and van der Waals volumes were obtained from their equilibrium structure derived by quantum mechanics calculations (QM). The first observable, the dipole moment, was calculated using Hartree-Fock method (HF) with Gaussian basis set 6-31G*; the second quantity, the van der Waals volume, was calculated at DFT level using Gaussian basis set 6-31G**; the averaged mpa was obtained after 1 μs of MD simulations of each inhibitor in water. The results are reported in table 3.4.

I Sulbactam (from database)

II Tazobactam (from database)

III Avibactam (from database)

IV Nacubactam (parametrized)

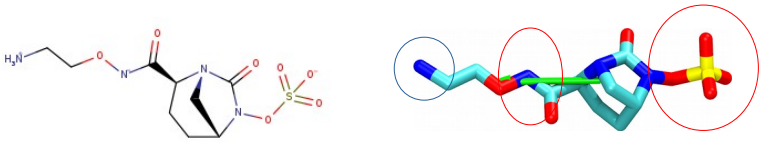

V Nacubactam modified (parametrized)

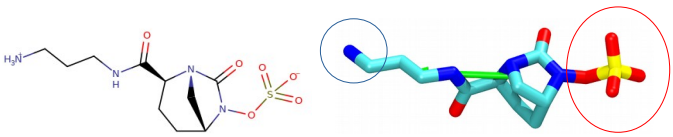

VI Relebactam (parametrized)

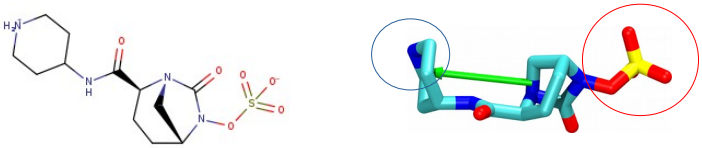

VII Zidebactam (parametrized)

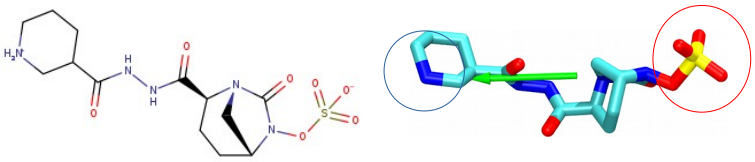

Fig. 3.11: 2D and 3D structure of β-lactamase inhibitors under study. In 3D structures, negatively charged group are circled of red and positively charged group are circled of blue. Derivation is reported.

In general, the selected inhibitors are characterized by a mpa higher than the average cross section area of all the porins. For this reason, it is clear that, during the permeation, the entropic contribution to the total free energy of the process will be remarkable. For this reason, the dipole moment plays a key role for the translocation. As seen in the chapter 1.3, if the inhibitor were able to reorient its dipole along the electric field, the energy cost would decrease (fig. 1.4). An optimal combination of these two observables would enhance the diffusion of the molecule into the channel increasing the probability to cross the OM. All the inhibitors share the presence of charged functional groups that are used to interact with protein's residues. Zwitterionic molecules are expected to interact with the residues inside the channel more favorably than negatively charged molecules, because they are able to establish interactions with both the loop L3 and the basic ladder.

As shown in the figure 3.11, only **I** e **II** are β-lactam β-lactamase inhibitors. These two inhibitors are negatively charged because of presence of the carboxilic group which is deprotoned at physiological pH. However, in this work, more attention has been devoted to the class of non-β-lactam inhibitors called *diazobicyclooctans*. Molecules **IV**, **V**, **VI**, **VII**, in particular, share the same scaffold of **III** [(2S,5R)-2-carbamoyl-7-oxo-1,6-diazabicyclo[3.2.1]octan-6-yl] hydrogen sulfate, with change in their "side chain" bonded to the N atom of the amidic group in position 2. The negative charge is due to the sulfate group, while the positive charge is due to protonated amino group in compound **IV** and **V,** to the protonated N of piperidinyl group in compound **VI** and **VII**. In particular, the derivative **V** was modified in silico by changing the atom O on the third position of the side chain of compound **IV** with an aliphatic C. This modification allowed to obtain a molecule very similar to nacubactam but zwitterionic instead of being negatively charged.

Tab. 3.4: Physico-chemical properties of β-lactamase inhibitors under study. The substrate are reported in ascending order by dipole moment.

	Net Charge (Coulomb)	Dipole Moment (Debye) HF/6-31G*	Minimal Projection Area ($Å^2$) 1 μs MD	Volume of van der Waals ($Å^3$) DFT/6-31G**
Sulbactam (**I**)	-1 *e*	5.5	44±3	182.4
Tazobactam (**II**)	-1 *e*	8.0	40±1	229.8
Avibactam (**III**)	-1 *e*	13.3	35±1	197.5
Nacubactam (**IV**)	-1 *e*	44.4	40±3	258.4
Nacubactam Modified (**V**)	0 (zwitterionic)	53.3	42±3	265.5
Relebactam (**VI**)	0 (zwitterionic)	43.1	46±3	288.6
Zidebactam (**VII**)	0 (zwitterionic)	56.9	44±3	319.9

3.4 Minimum Energy Path of Diazobicyclooctans in their Permeation Process

In the previous paragraph, the derivatives of avibactam were introduced. In this work, one of the main objective was to compare the free energy landscape related to each β-lactamase inhibitor for permeation through OmpF. The free energy profile of this process was reconstructed with WT-METAD by the integration and sign inversion of the Gaussian functions added during a simulation, as explained in the paragraph 2.2. The FES obtained for all the molecules while translocating through OmpF are shown in figure 3.12 together with simulation time. The 'position z' of the molecule along the permeation axes is reported on the y-axes: CR is located into the z-window between 0 and -5 Å. The 'orientation Φ' of molecule's dipole moment is reported on x-axes (it is worth of reminding that dipole goes from negative to positive charge): values below 90° correspond to dipoles pointing upwards (EV, positive group up), values higher than 90° correspond to dipoles pointing downwards (PV, negative group up). The region between -10 Å <z< +10 Å is the most important inside the pore, which is rich of energy minima along the minimum free energy path. Conformers extracted from energy minima were studied in order to determine the structural details involved in protein-molecule interactions with the purpose to understand physico-chemical parameters that might be modified allowing optimizing their interactions and consecutively their translocation into porins. All the inhibitors show the highest free energy values in the restricted central region (CR), in agreement with similar investigations reported in the literature. [3], [53] Further, similarities among FESs concern the range 0 Å <z< 5 Å (preorientation region) where a minimum energy is present for all molecules. [3] Also, the minimum energy paths are similar except relebactam, which does not need to rotate its dipole moment towards PV. More details are reported below. Finally, free energy

profile in both EV and PV regions is almost similar and does not give relevant information.

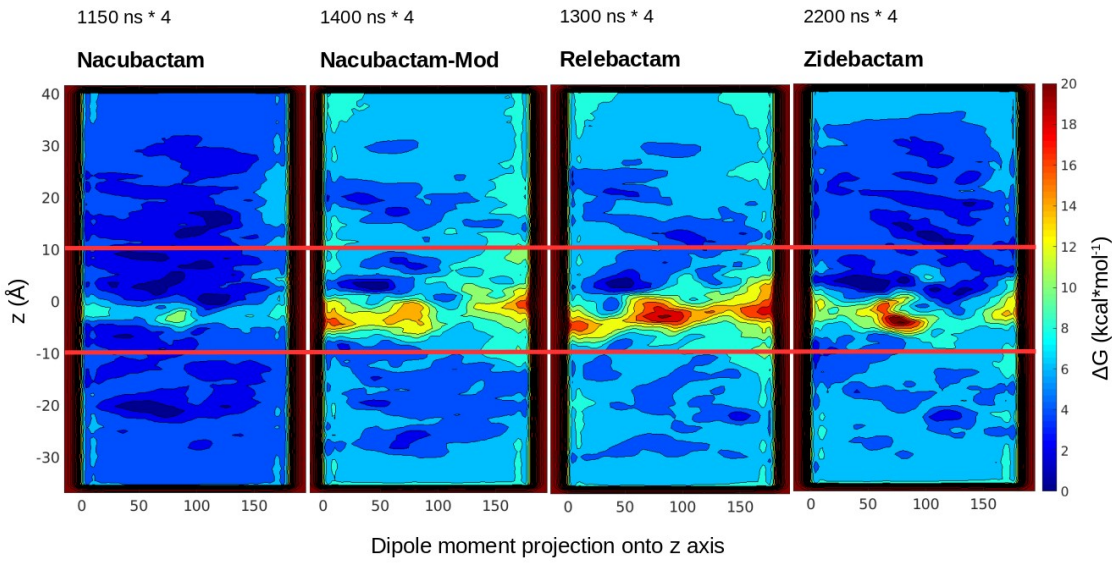

Fig. 3.12: Free-energy surfaces (FES) obtained from WT-METAD simulation as a function of the 'position z' of the molecule along the permeation axes, reported on the y-axes, and the 'orientation Φ' of molecule's dipole moment, reported on x-axes. The red lines delimit the area with preorientation region and constriction region (-10 Å <z< 10 Å).

Preliminary conclusions can be drawn by considering the values in table 3.4 and the one-dimensional free energy profiles reported in figure 3.13, from which the height of main energy barriers can be compared. In the case of **IV** and **V** the two barriers are comparable with a height of ~ 2 kcal/mol. The structural change of molecule **V**, from negative to zwitterionic, allowed to obtain a higher dipole moment with respect the dipole moment of molecule **IV**, though the slightly larger dimensions of **V**, in terms of mpa and van der Waals volume. The more favorable electrostatic compensates the larger dimensions, obtaining a slightly lower barrier. The same interpretation can be applied to **VI** and **VII**. The former (relebactam) has to overcome a higher energy barrier

(~ 4 kcal/mol) due to its larger mpa associated to its relatively small dipole moment; the latter (zidebactam), despite the large van der Waals volume, show a mpa smaller than that of **VI** due to its flexibility, and the large value of dipole moment allow to lower the energy barrier.

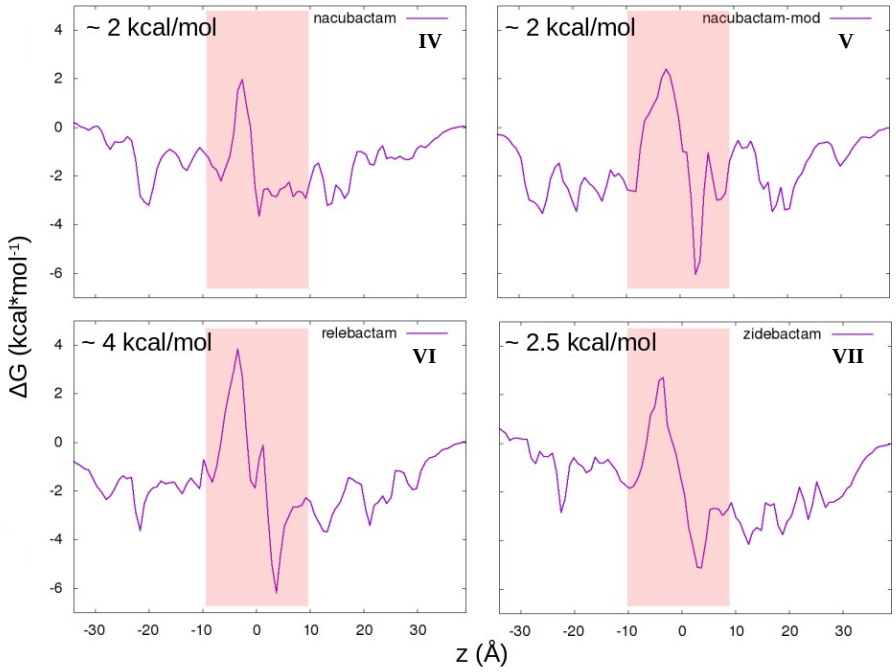

Fig. 3.13: One-dimensional free energy profiles of β-lactamase inhibitors under analysis. The color filled section delimit the area with preorientation region and constriction region (-10 Å <z< 10 Å).

The conformer extracted from energy minima has been analyzed more in detail, as mentioned above. Each trajectory, obtained from WT-METAD simulations, was aligned on the basis of the first monomer of the porin using a reference template. Then, the representative structure for each basin was obtained through a cluster analysis based on "positional" root mean square deviation (rmsd) using CPPTRAJ software with a cutoff of 2 Å. The representative structure of the most numerous cluster was used to extract the pose of the corresponding minimum. Then, the dipole moment of that pose was

computed in order to observe its interaction with the internal transversal electric field of the channel. In fact, the channel electrostatics might force dipolar molecules to adopt a preferential orientation while permeating through the channel. Such a preferential orientation was found to change along the channel, imposing a kind of "choreography" for molecules passing through it.

In order to get a more detailed description of the reorientations executed by the four inhibitors inside the channel, a statistical analysis of the polar coordinates of their electric dipole was performed as reported in reference. [53] The distribution of the azimuth angles and the altitude angle (defined as reported in fig. 3.14), were calculated for consecutive 2.5 Å cross-sections along the channel axis. The altitude angle is one of the two CV and, thus, was biased during metadynamics simulations, thus for a correct analysis it was reweighted. The azimuth and the altitude of waters' net dipole (used as a probe in order to quantifying the inner electric field) were used as a reference (the azimuth found in the cross-section with the highest waters order was used as angular reference and thus placed to zero). The reference waters are represented by a green vertical segment in the plots. The results are shown in the next section for all the inhibitors under investigation.

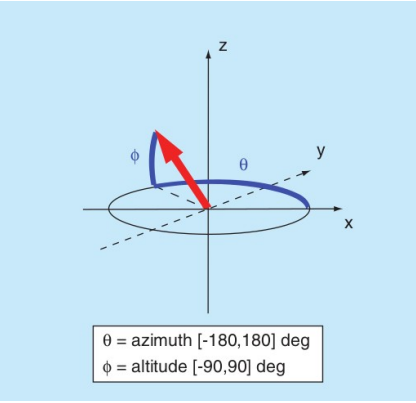

Fig. 3.14: Electric dipoles orientation was analyzed in terms of polar coordinates as defined. Reprinted from [53].

3.4.1 Nacubactam

As reported in similar studies [3; 53], in the case of OmpF the preorientation region plays a key role for drug's permeation reorienting the azimuth orientation of the dipole moment of the molecule involved in the process. In the case of nacubactam this effect is not so important. In fig. 3.15 b) it is possible to observe a slight reorientation of dipole on the xy-plane during the passage from preorientation region (structures purple and orange) to CR (structure green). The distributions of azimuth angle of nacubactam's dipole in each Z region are shown in figure 3.15. A good agreement of the dipole direction with respect to the tranversal component of internal electric field is observed until the exit from CR towards PV (-7.5 Å <z< 5 Å). About the altitude angle at the mouth of CR (structure from violet to orange) the dipole changes its orientation. Starting from the region at -2.5 Å <z< 0.0 Å the molecule needs to point its dipole towards the PV region in order to cross the channel. Dipoles do not match with z component of electric field because this component is less strong than the transversal one.

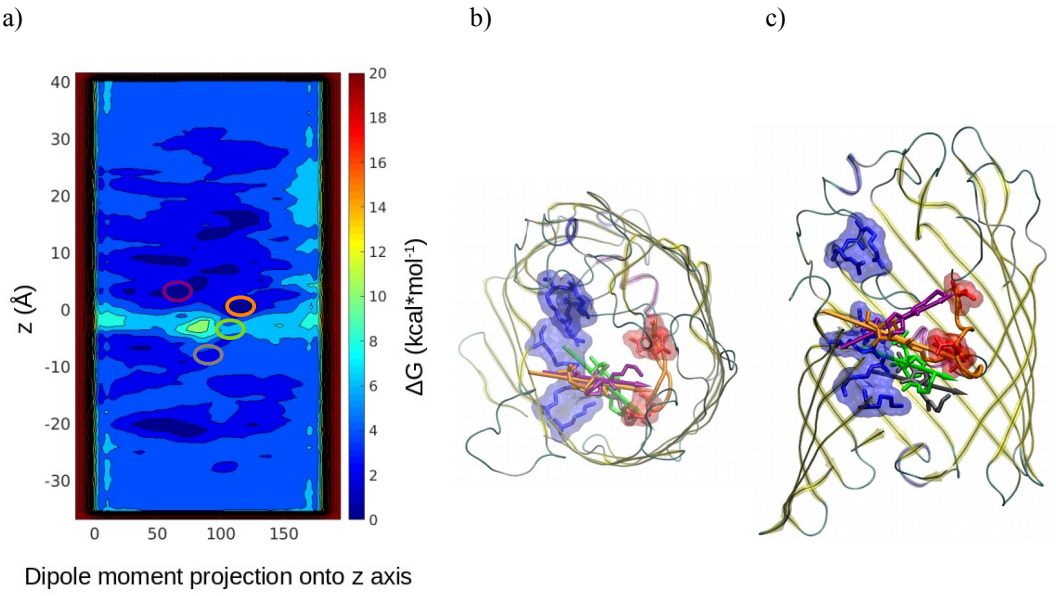

Fig. 3.15: Free-energy surfaces (FES) of nacubactam obtained from WT-METAD simulation as a function of the 'position z' of the molecule along the permeation axes, reported on the y-axes, and the 'orientation Φ' of molecule's dipole moment, reported on x-axes. The colored circles show the basin from which the conformations that describe the minimum energy path were extracted; b) top view and c) side view of sequence of nacubactam translocation through OmpF, structure colors are correlated with circle colors in a)

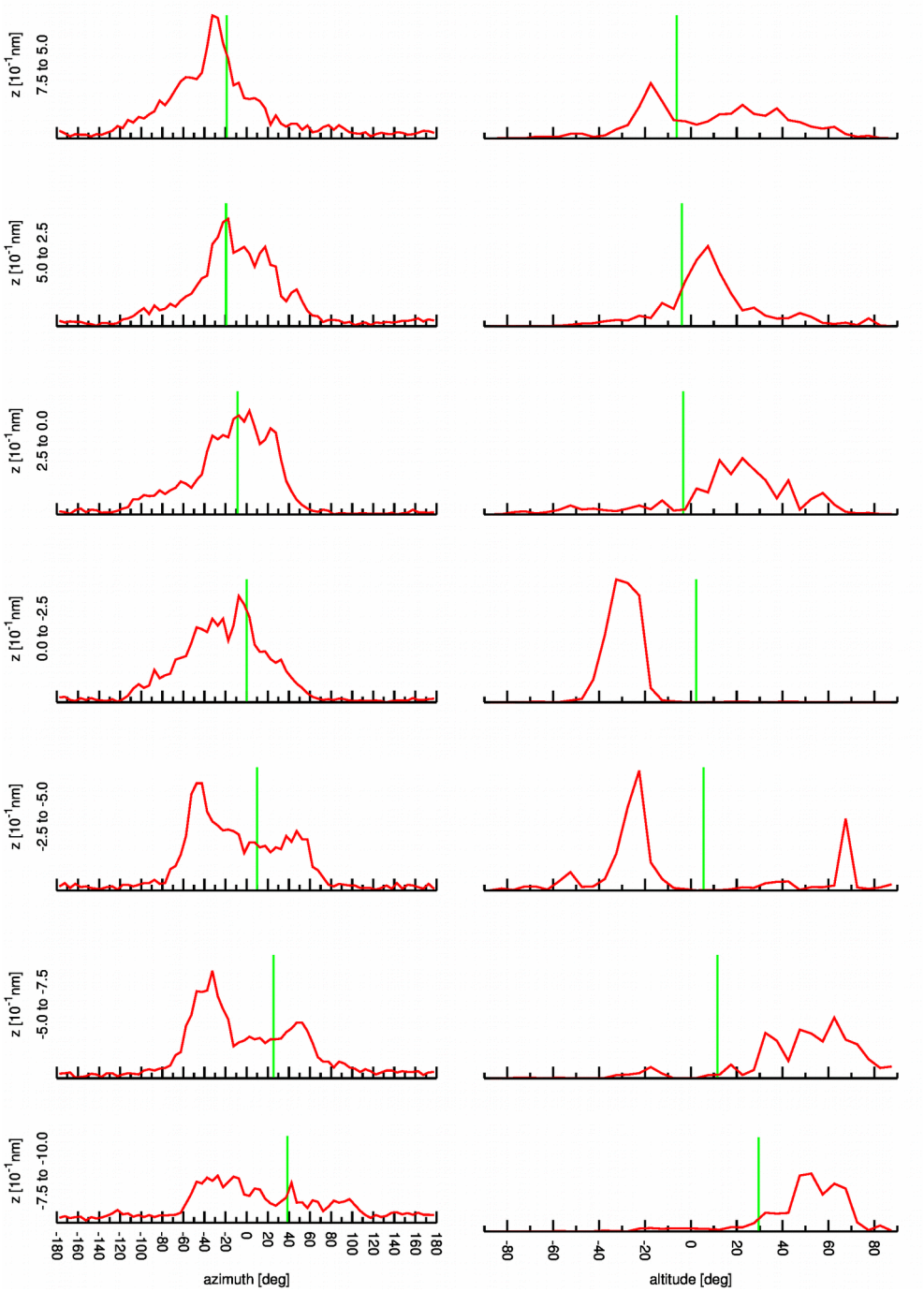

Fig. 3.16: The distribution of the azimuth and altitude angle of nacubactam's electric dipole is shown for 2.5 Å cross-sections along the channel axis of the OmpF porin. The cross-section (+10.0 Å < z < +7.5 Å) is in the preorientation region, the cross-section (0.0 Å < z < -2.5 Å) is in the constriction region of the pore. The green lines are used as a reference for the azimuth and altitude of the waters' net dipole in the same channel cross-section, calculated in the absence of antibiotic.

3.4.2 Nacubactam Modified

The nacubactam modified shows a perfect alignment with the transversal field in the preorientation region (cyan structure) and a reorientation of its dipole before the entry into CR (figure 3.17 b, structures purple and orange). Figure 3.18 shows, furthermore, a slight misalignment between azimuth angle of dipole distribution and water reference restored into the CR. In order to pass through the pore, also Nacubactam must point its dipole towards PV region. The reorientation of its dipole along z component is reflected by altitude angle distribution of dipoles shown in figure 3.18.

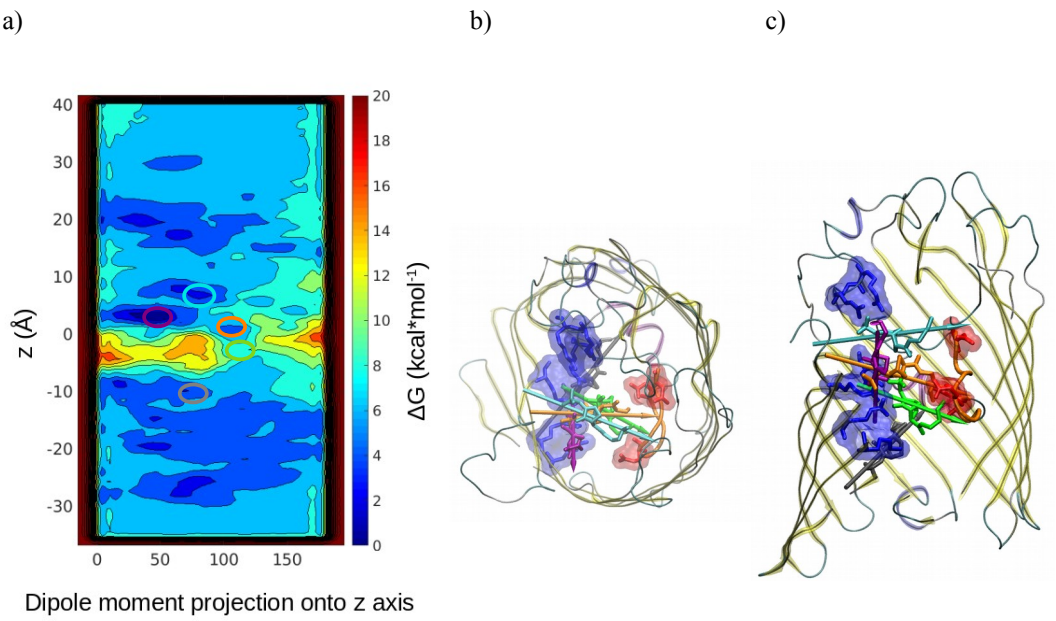

Fig 3.17: Free-energy surfaces (FES) of nacubactam modified obtained from WT-METAD simulation as a function of the 'position z' of the molecule along the permeation axes, reported on the y-axes, and the 'orientation Φ' of molecule's dipole moment, reported on x-axes. The colored circles show the basin from which the conformations that describe the minimum energy path were extracted; b) top view and c) side view of sequence of nacubactam modified translocation through OmpF, structure colors are correlated with circle colors in a).

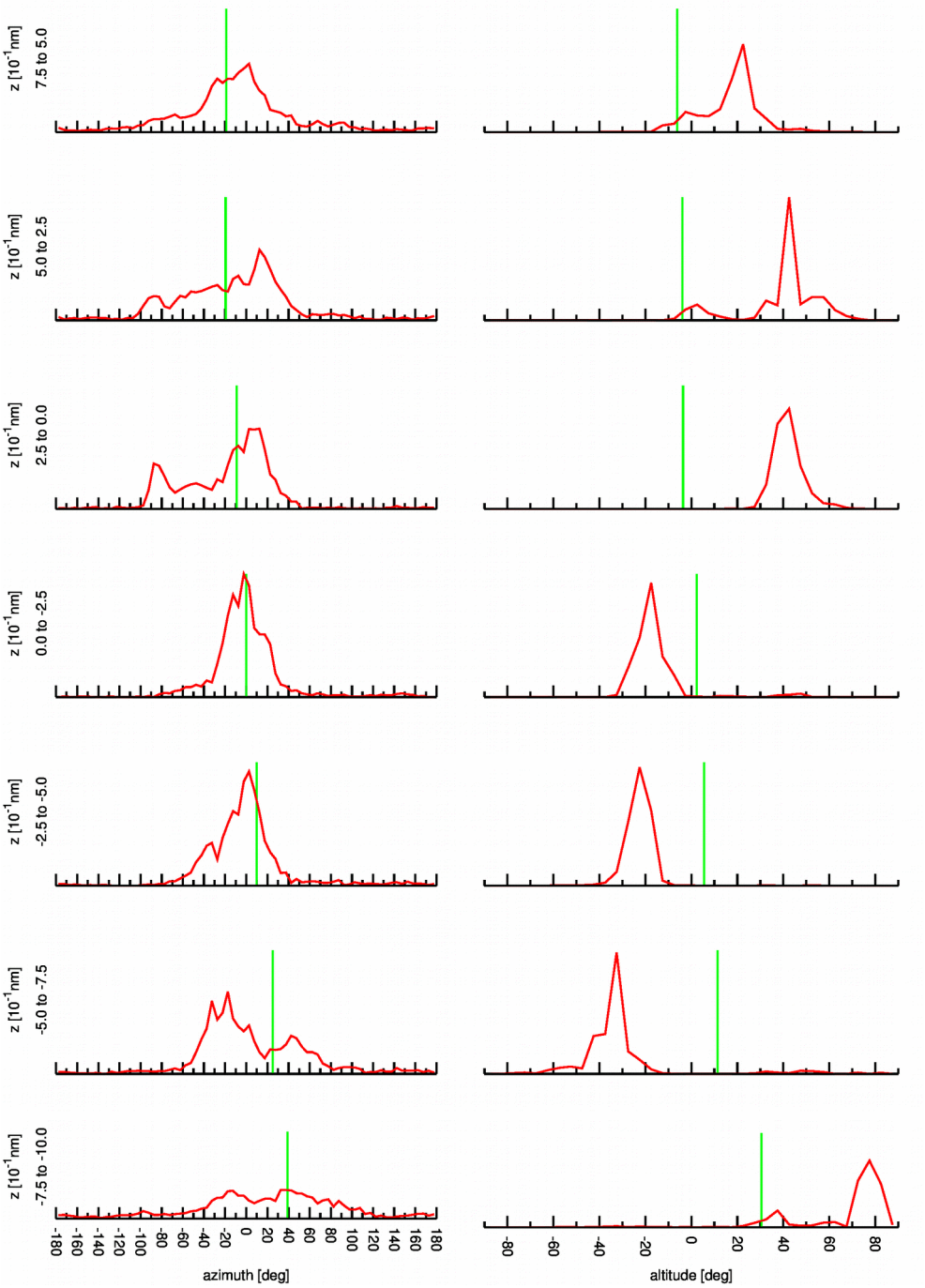

Fig. 3.18: The distribution of the azimuth and altitude angle of nacubactam modified's electric dipole is shown for 2.5 Å cross-sections along the channel axis of the OmpF porin. The cross-section (+10.0 Å < z < +7.5 Å) is in the preorientation region, the cross-section (0.0 Å < z < -2.5 Å) is in the constriction region of the pore. The green lines are used as a reference for the azimuth and altitude of the waters' net dipole in the same channel cross-section, calculated in the absence of antibiotic.

3.4.3 Relebactam

A different behavior is observed for relebactam. After the reorientation due to interactions in the preorientation region, the molecule is able to align its dipole in favor of xy-component of electric field during the passage into CR. Differently from the others inhibitors under study it does not need to reorient its dipole along altitude angle and exploits the interactions between its negatively charged sulfate group and positively charged residues of basic ladder in order to cross the CR.

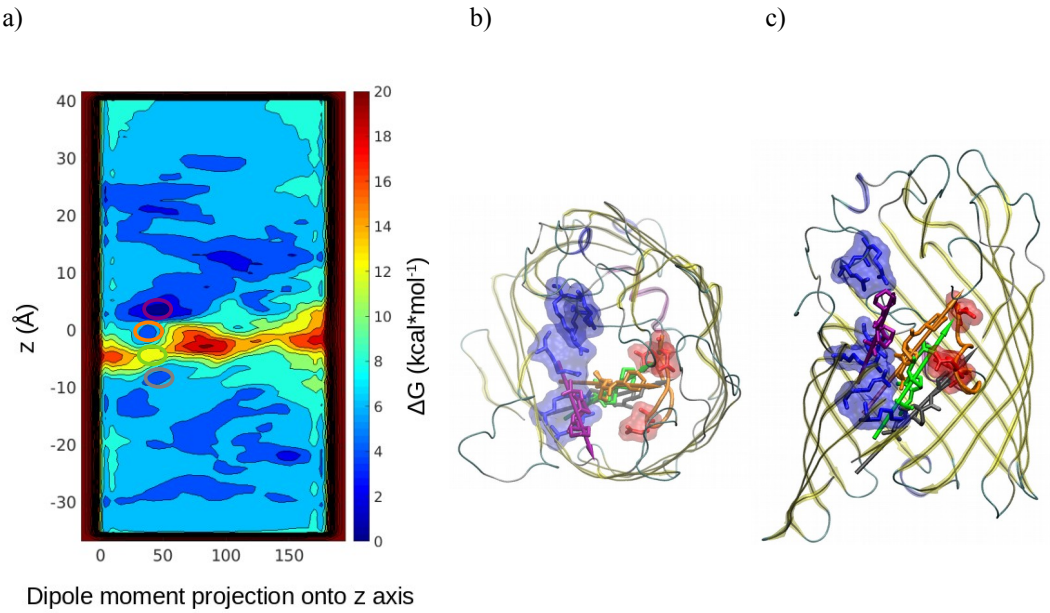

Fig. 3.19: Free-energy surfaces (FES) of relebactam obtained from WT-METAD simulation as a function of the 'position z' of the molecule along the permeation axes, reported on the y-axes, and the 'orientation Φ' of molecule's dipole moment, reported on x-axes. The colored circles show the basin from which the conformations that describe the minimum energy path were extracted; b) top view and c) side view of sequence of relebactam translocation through OmpF, structure colors are correlated with circle colors in a).

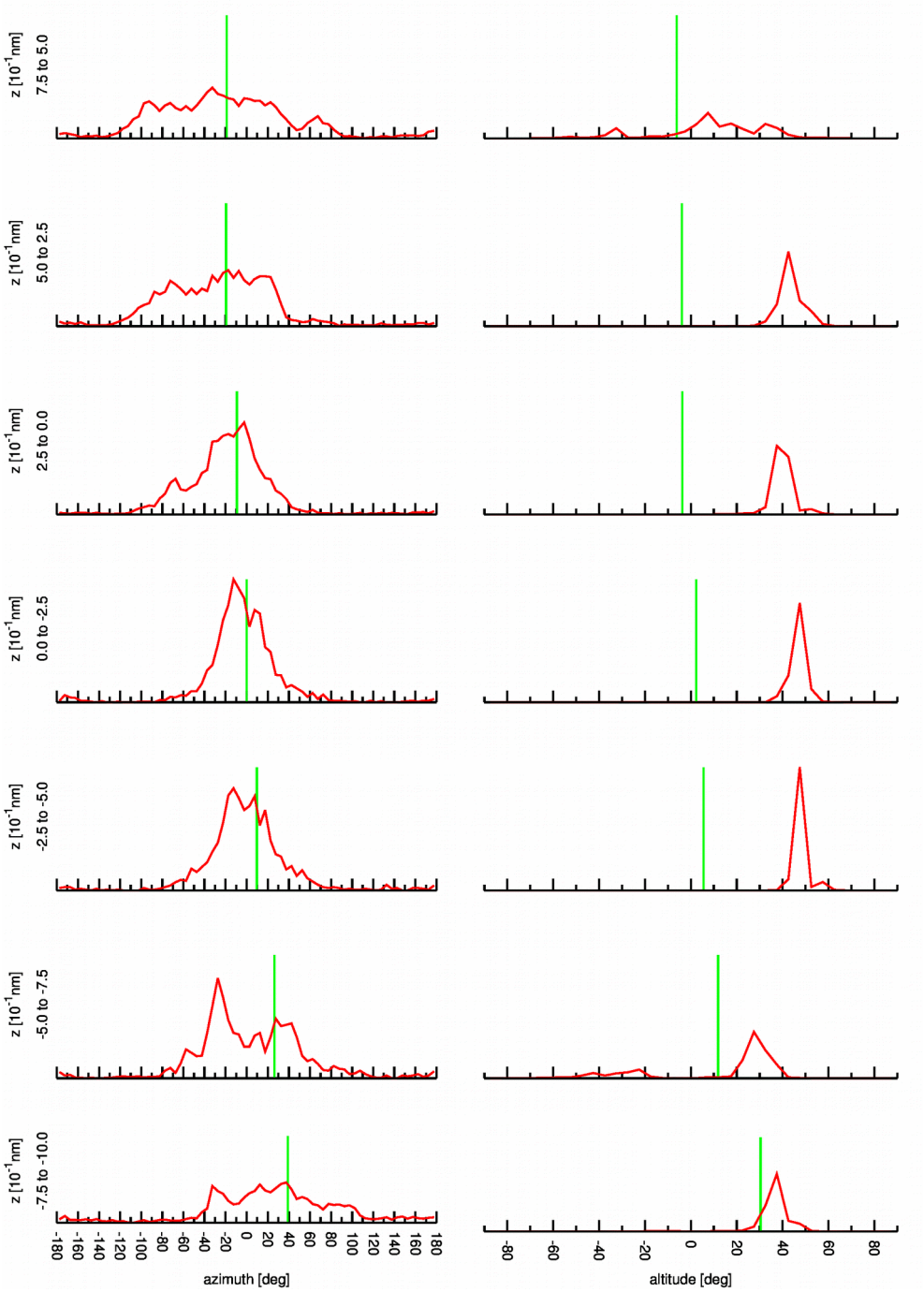

Fig. 3.20: The distribution of the azimuth and altitude angle of relebactam's electric dipole is shown for 2.5 Å cross-sections along the channel axis of the OmpF porin. The cross-section (+10.0 Å < z < +7.5 Å) is in the preorientation region, the cross-section (0.0 Å < z < -2.5 Å) is in the constriction region of the pore. The green lines are used as a reference for the azimuth and altitude of the waters' net dipole in the same channel cross-section, calculated in the absence of antibiotic.

3.4.4 Zidebactam

A similar behavior is shown by zidebactam; it does not reorient its dipole moment in the preorientation region but it needs to point its dipole towards PV region in order to pass the CR. At CR level (-2.5 Å <z< 0.0 Å) the azimuth angle distribution match with water reference and the strange orientation of conformer green in the figure 3.21, related to the saddle point, is due to the negative x-component of internal electric field. [54] It is worth to note how relebactam and zidebactam have a longer, larger and less flexible lateral chain compared to nacubactam.

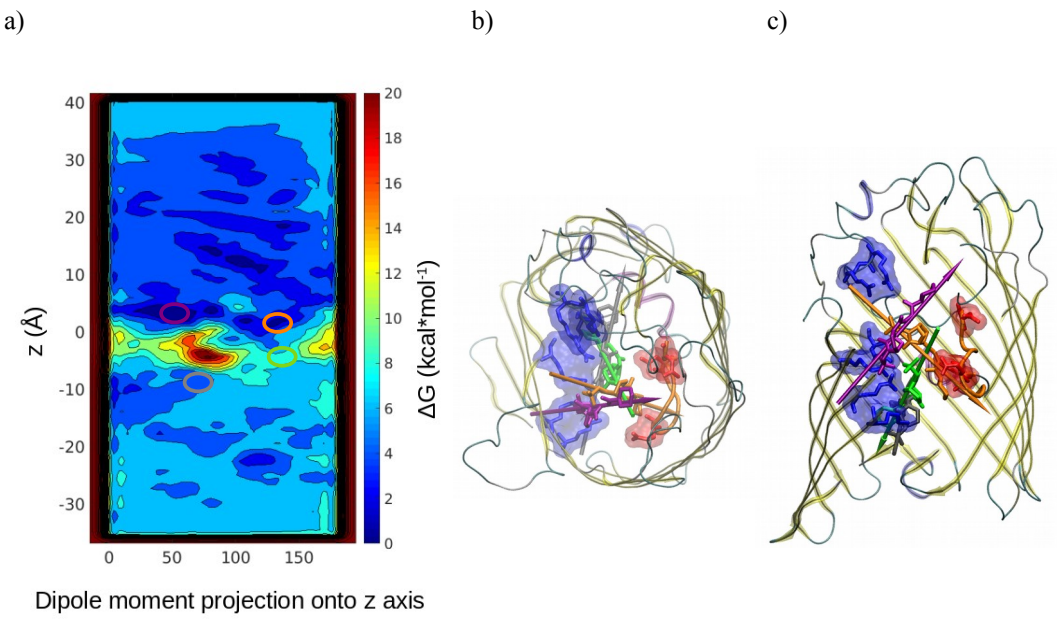

Fig. 3.21: Free-energy surfaces (FES) of zidebactam obtained from WT-METAD simulation as a function of the 'position z' of the molecule along the permeation axes, reported on the y-axes, and the 'orientation Φ' of molecule's dipole moment, reported on x-axes. The colored circles show the basin from which the conformations that describe the minimum energy path were extracted; b) top view and c) side view of sequence of zidebactam translocation through OmpF, structure colors are correlated with circle colors in a).

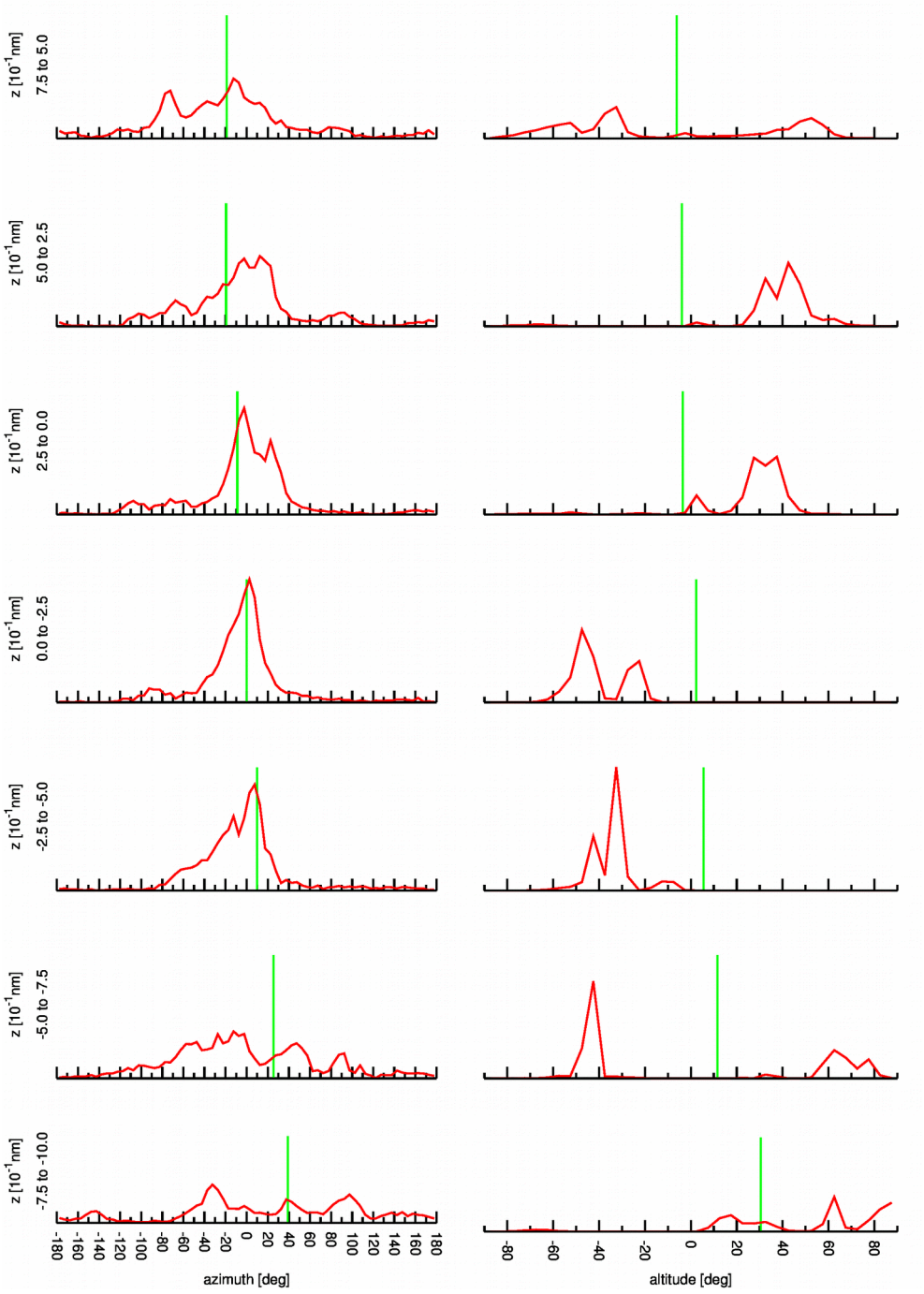

Fig. 3.22: The distribution of the azimuth and altitude angle of zidebactam's electric dipole is shown for 2.5 Å cross-sections along the channel axis of the OmpF porin. The cross-section (+10.0 Å < z < +7.5 Å) is in the preorientation region, the cross-section (0.0 Å < z < -2.5 Å) is in the constriction region of the pore. The green lines are used as a reference for the azimuth and altitude of the waters' net dipole in the same channel cross-section, calculated in the absence of antibiotic.

3.5 Convergence of the Free Energy

For those systems where the ergodicity is questioned by the high number of degree of freedom, to reach energy convergence is an important problem. In general, within metadynamics, the convergence is reached when a diffusive regime is obtained. In our case, we should see continuous translocation of molecules through the channel. Another parameter we can monitor is the value of the free energy in the bulk solution outside the pore, on both CIS and TRANS side. At convergence we expect these values to be the same.

Quantitatively, one possible test to verify the convergence of a simulation is represented by the error calculation (Eq. 53), by using the block analysis technique as suggested by the Plumed developer team. For different block sizes, the average free-energy and the error were calculated. The error increases with the block length until it reaches a plateau in correspondence of a dimension of the block that exceeds the correlation between data points. [55], [56] In other words, the error become constant when the length of the blocks is enough to have a representative value of the particular observable, i.e. the free energy in this case.

$$\text{average error} = \frac{1}{N}\sum_{i=1}^{N}\sigma_i \qquad 53)$$

In the expression N is the total number of grid points at which the function was evaluated and σ_i is the error bar for the estimate of the function that was calculated for the ith grid point. [55], [56]

In figure 3.22 the results for the simulated systems are reported; the convergence seems to be reached, the error value fluctuate around 0.5 kcal/mol with increasing the length of blocks for all the cases.

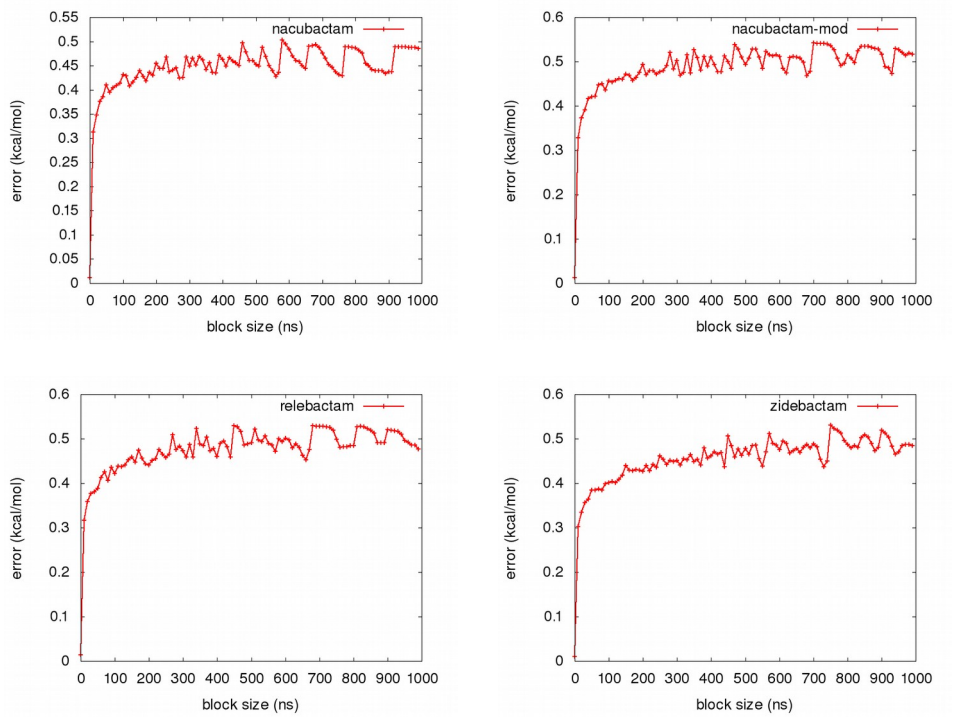

Fig. 3.22: The size of the error bars of free-energy from WT-METAD calculated with different lengths of block average.

Free energy calculation using reweighting technique, paragraph 2.2, represents another test to verify convergence of free energy profile. Both free energy obtained from WT-METAD simulations and from reweighting calculation should have a comparable profile. In figure 3.23 are reported the results obtained by using a code developed from the research group of Prof. Gervasio of UCL. Energy profiles are quite in agreement except for the case of zidebactam. This effect could be due to the asymmetrical

exploration of walkers in the phase space (see the FES on figure 3.12 and 3.21), suggesting the need to increase the length of metadynamics simulations.

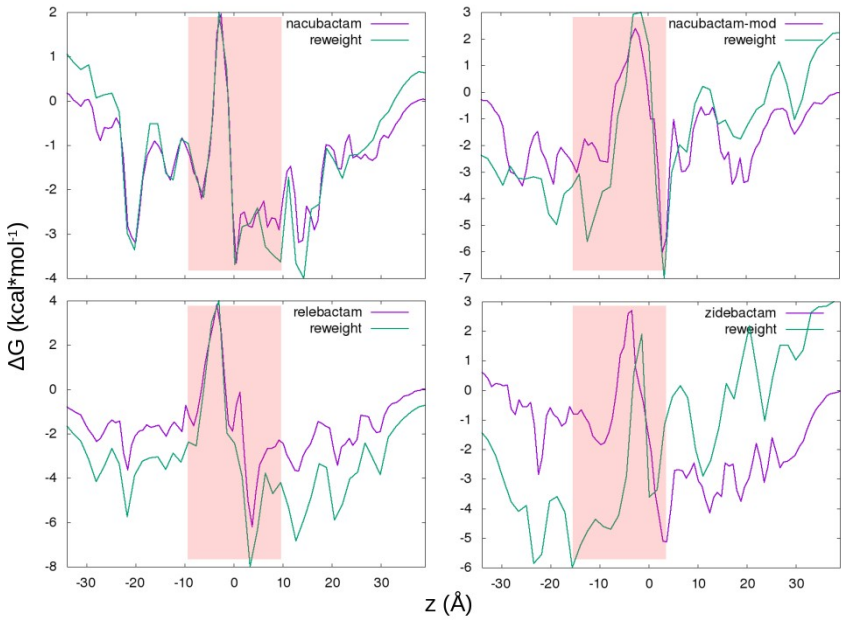

Fig. 3.23: One-dimensional free energy profiles of β-lactamase inhibitors under analysis. The color filled section delimit the area with preorientation region and constriction region (-10 Å <z< 10 Å). The purple curve is the free energy profile calculated from WT-METAD simulations, the green curve is the free energy profile calculated from reweighting technique.

4 Conclusions and Outlook

In this work, the first results obtained concerns the importance of "in silico" studies in all branches of science. MD simulations allowed confirming the possibility of using the two principal porins OmpF and OmpC as a model for the respective porin groups across the family of *Enterobacteriaceae*. Having a general model system, the same environment for different molecules could be simulated focusing the attention on substrate physico-chemical properties. In this specific case, where the complexity of the systems implies a long simulation time, such aspect results crucial in order to decrease the number of simulations needed to reach important data for the entire family of *Enterobatericeae*.

Computational studies were applied also to get atomistic details hard to obtain with experimental techniques. In order to develop a new experimental method that was able to provide information about the flux rates of β-lactamase inhibitors through OmpF, molecular details have been obtained by using MD and WT-METAD simulations. From experiments it was possible to observe that single-channel conductance of the three investigated inhibitors through OmpF unexpectedly presented the same order of magnitude as with NaCl, as reported on Table S1 in the manuscript [52]. By reconstructing the energy profile of Na^+, Cl^- and avibactam permeation through OmpF it was possible to understand the microscopic reasons for their similar permeability. Differently from chloride, avibactam has favorable interactions at the constriction region. Thanks to these interactions, it partially compensates the steric barrier, which is localized only at the level of the constriction region. Conversely, the barrier for the chloride ion, though smaller, is very broad and extends throughout the channel.

Finally, the comparison of FES related to four avibactam derivatives allowed understanding the physico-chemical parameters involved in protein-substrate interactions during the translocation process, allowing to lay the foundation for the future rational changes in the molecular structure of the drugs that need to cross general porins in order to penetrate the Gram-negative bacterial cell. The most important result of the present work is represented by the impossibility of finding a single physico-chemical parameter responsible of permeation. The Gibbs free energy of the process under investiygation in the NVT ensamble depends, obviously, on two main thermodynamics contributions:

$$\Delta G_{(NVT)} = \Delta H - T\Delta S \quad . \qquad 54)$$

The entropic contribution is the main hindrance to the substrate translocation; it depends on the narrowing at level of the CR of the protein channel and on the molecule size and shape, with the weight of its flexibility on the mpa value not to be underrated. The decrease of entropy must be compensated by increasing the module of the enthalpy. The enthalpic contribution to the permeation mostly depends on the electrostatic interactions between the aminoacidic residues inside the channel and the permeating substrate. The capability of a molecule to reorient its dipole moment in favor of the transversal electric field of the porin, in addition to the possibility of establishing interactions between charged groups or hydrogen bonds, enhances the permeation rate through the pore by lowering the overall energy barrier ~~which is opposed to the process~~. We understood that it is necessary to find a subtle combination among several physico-chemical features of substrates and to consider their fluctuations carefully ~~is needed~~ in

order to build new molecular species able to cross the outer membrane of Gram-negative bacteria using porins more efficiently.

For the near future, a new analysis tools aimed at monitoring the fluctuations of dipole moment and mpa during the permeation is under development. We would observe how a substrate can modulate the two main physico-chemical properties that allow it to enhance its translocation.

Moreover, a new promising class of non-β-lactam inhibitors is represented by boronic acid. By focusing on three inhibitors belonging to this class, we have started to use these molecules as model in a study aimed at setting-up a different simulation method in order to speed-up the sampling and, similar to what already done, understand physico-chemical parameters governing the translocation process.

[1] G. Taubes, “The Bacteria Fight Back,” Science (80-.)., vol. 321, no. 5887, pp. 356–361, Jul. 2008.

[2] J. G. V. Donald Voet, Biochemistry. 2010.

[3] S. Acosta-Gutierrez, M. A. Scorciapino, I. Bodrenko, and M. Ceccarelli, “Filtering with Electric Field: The Case of E. coli Porins,” J. Phys. Chem. Lett., vol. 6, no. 10, pp. 1807–1812, May 2015.

[4] A. L. Demain and R. P. Elander, “The β -lactam antibiotics : past , present , and future,” pp. 5–19, 1999.

[5] S. M. Drawz and R. A. Bonomo, “Three decades of β-lactamase inhibitors,” Clin. Microbiol. Rev., vol. 23, no. 1, pp. 160–201, 2010.

[6] X.-Z. Li and H. Nikaido, “Efflux-Mediated Drug Resistance in Bacteria,” Drugs, vol. 69, no. 12, pp. 1555–1623, Aug. 2009.

[7] V. P. Sandanayaka and A. S. Prashad, “Resistance to β -Lactam Antibiotics: Structure and Mechanism Based Design of β -Lactamase Inhibitors,” pp. 1145–1165, 2002.

[8] J.-M. Pagès, C. E. James, and M. Winterhalter, “The porin and the permeating antibiotic: a selective diffusion barrier in Gram-negative bacteria,” Nat. Rev. Microbiol., vol. 6, no. 12, pp. 893–903, Dec. 2008.

[9] C. Danelon, E. M. Nestorovich, M. Winterhalter, and M. Ceccarelli, “Interaction of Zwitterionic Penicillins with the OmpF Channel Facilitates Their Translocation,” vol. 90, no. March, 2006.

[10] H. Weingart, M. Petrescu, and M. Winterhalter, “Biophysical Characterization of In- and Efflux in Gram-Negative Bacteria,” pp. 789–796, 2008.

[11] E. Berkane et al., “Nanopores: Maltoporin channel as a sensor for maltodextrin and lambda-phage,” J. Nanobiotechnology, vol. 3, pp. 1–6, 2005.

[12] C. Danelon, E. M. Nestorovich, M. Winterhalter, and M. Ceccarelli, “Interaction of Zwitterionic Penicillins with the OmpF Channel Facilitates Their Translocation,” vol. 90, no. March, 2006.

[13] Christopher J. Cramer, Essentials of Computational Chemistry: Theories and Models, 2nd Edition. 2004.

[14] A. Barducci, M. Bonomi, and M. Parrinello, “Metadynamics,” Wiley Interdiscip. Rev. Comput. Mol. Sci., vol. 1, no. 5, pp. 826–843, Sep. 2011.

[15] A. Laio, A. Rodriguez-fortea, F. L. Gervasio, M. Ceccarelli, and M. Parrinello, “Assessing the Accuracy of Metadynamics,” pp. 6714–6721, 2005.

[16] A. Laio and M. Parrinello, “Escaping free-energy minima,” 2002.

[17] M. Ceccarelli, C. Danelon, A. Laio, and M. Parrinello, “Microscopic Mechanism of Antibiotics Translocation through a Porin,” Biophys. J., vol. 87, no. 1, pp. 58–64, Jul. 2004.

[18] P. Raiteri, A. Laio, F. L. Gervasio, C. Micheletti, and M. Parrinello, “Efficient Reconstruction of Complex Free Energy Landscapes by Multiple Walkers Metadynamics †,” pp. 3533–3539, 2006.

[19] A. Barducci, G. Bussi, and M. Parrinello, “Well-Tempered Metadynamics: A Smoothly Converging and Tunable Free-Energy Method,” Phys. Rev. Lett., vol. 100, no. 2, p. 020603, Jan. 2008.

[20] Y. Sugita and Y. Okamoto, “Replica-exchange molecular dynamics method for protein folding,” Chem. Phys. Lett., vol. 314, no. 1–2, pp. 141–151, Nov. 1999.

[21] B. Miasojedow, E. Moulines, and M. Vihola, “Adaptive parallel tempering algorithm,” May 2012.

[22] S. Piana and A. Laio, “A Bias-Exchange Approach to Protein Folding,” pp. 4553–4559, 2007.

[23] M. Road and B. House, “Bias - - exchange metadynamics simulations : an efficient strategy for the analysis of conduction and selectivity in ion channels.”

[24] W. D. Cornell et al., “A Second Generation Force Field for the Simulation of Proteins, Nucleic Acids, and Organic Molecules,” J. Am. Chem. Soc., vol. 117, no. 19, pp. 5179–5197, May 1995.

[25] W. F. van Gunsteren and H. J. C. Berendsen, “Groningen Molecular Simulation (GROMOS) Library Manual.” pp. 1–121, 1987.

[26] M. Christen et al., “The GROMOS software for biomolecular simulation: GROMOS05,” J. Comput. Chem., vol. 26, no. 16, pp. 1719–1751, Dec. 2005.

[27] A. D. MacKerell et al., “All-Atom Empirical Potential for Molecular Modeling and Dynamics Studies of Proteins †,” J. Phys. Chem. B, vol. 102, no. 18, pp. 3586–3616, Apr. 1998.

[28] G. A. Kaminski, R. A. Friesner, J. Tirado-Rives, and W. L. Jorgensen, “Evaluation and Reparametrization of the OPLS-AA Force Field for Proteins via Comparison with Accurate Quantum Chemical Calculations on Peptides †,” J. Phys. Chem. B, vol. 105, no. 28, pp. 6474–6487, Jul. 2001.

[29] P. Mark and L. Nilsson, “Structure and Dynamics of the TIP3P, SPC, and SPC/E Water Models at 298 K,” J. Phys. Chem. A, vol. 105, no. 43, pp. 9954–9960, Nov. 2001.

[30] J. L. F. Abascal and C. Vega, “A general purpose model for the condensed phases of water: TIP4P/2005,” J. Chem. Phys., vol. 123, no. 23, p. 234505, Dec. 2005.

[31] W. L. Jorgensen, J. Chandrasekhar, J. D. Madura, R. W. Impey, and M. L. Klein, “Comparison of simple potential functions for simulating liquid water,” J. Chem. Phys., vol. 79, no. 2, pp. 926–935, Jul. 1983.

[32] J. L. F. Abascal and C. Vega, “A general purpose model for the condensed phases of water: TIP4P/2005,” J. Chem. Phys., vol. 123, no. 23, p. 234505, Dec. 2005.

[33] H. J. C. Berendsen, J. P. M. Postma, W. F. van Gunsteren, and J. Hermans, “Interaction Models for Water in Relation to Protein Hydration,” 1981, pp. 331–342.

[34] U. Essmann, L. Perera, M. L. Berkowitz, T. Darden, H. Lee, and L. G. Pedersen, “A smooth particle mesh Ewald method,” J. Chem. Phys., vol. 103, no. 19, pp. 8577–8593, Nov. 1995.

[35] H. J. C. Berendsen, J. P. M. Postma, W. F. van Gunsteren, A. DiNola, and J. R. Haak, “Molecular dynamics with coupling to an external bath,” J. Chem. Phys., vol. 81, no. 8, pp. 3684–3690, Oct. 1984.

[36] J. C. Phillips et al., “Scalable Molecular Dynamics with NAMD,” 2005.

[37] M. J. Harvey, G. Giupponi, and G. De Fabritiis, “ACEMD : Accelerating Biomolecular Dynamics in the,” pp. 1632–1639, 2009.

[38] D. J. T. Michael P. Allen, Computer simulation of liquids. 2017.

[40] F. Marinelli, F. Pietrucci, A. Laio, and S. Piana, “A Kinetic Model of Trp-Cage Folding from Multiple Biased Molecular Dynamics Simulations,” PLoS Comput. Biol., vol. 5, no. 8, p. e1000452, Aug. 2009.

[41] M. Bonomi and M. Parrinello, “Enhanced Sampling in the Well-Tempered Ensemble,” Phys. Rev. Lett., vol. 104, no. 19, p. 190601, May 2010.

[42] World Health Organization “ANTIMICROBIAL RESISTANCE” Global Report on Surveillance 2014.

[43] S. Varma, S. Chiu, and E. Jakobsson, “The Influence of Amino Acid Protonation States on Molecular Dynamics Simulations of the Bacterial Porin OmpF,” vol. 90, no. January, pp. 112–123, 2006.

[44] K. R. Mahendran, M. Kreir, H. Weingart, N. Fertig, and M. Winterhalter, “Permeation of Antibiotics through Escherichia coli OmpF and OmpC Porins: Screening for Influx on a Single-Molecule Level,” J. Biomol. Screen., vol. 15, no. 3, pp. 302–307, Mar. 2010.

[45] Dolinsky TJ, Nielsen JE, McCammon JA, Baker NA. PDB2PQR: an automated pipeline for the setup, execution, and analysis of Poisson-Boltzmann electrostatics calculations. Nucleic Acids Research 32 W665-W667 (2004).

[46] G. Malloci, A. Vargiu, G. Serra, A. Bosin, P. Ruggerone, and M. Ceccarelli, “A Database of Force-Field Parameters, Dynamics, and Properties of Antimicrobial Compounds,” Molecules, vol. 20, no. 8, pp. 13997–14021, Aug. 2015.

[47] ChemAxon, “Marvin.” [Online]. Available: https://chemaxon.com/products/marvin.

48] Gaussian 09, Revision A.02, M. J. Frisch, G. W. Trucks, H. B. Schlegel, G. E. Scuseria, M. A. Robb, J. R. Cheeseman, G. Scalmani, V. Barone, G. A. Petersson, H. Nakatsuji, X. Li, M. Caricato, A. Marenich, J. Bloino, B. G. Janesko, R. Gomperts, B. Mennucci, H. P. Hratchian, J. V. Ortiz, A. F. Izmaylov, J. L. Sonnenberg, D. Williams-Young, F. Ding, F. Lipparini, F. Egidi, J. Goings, B. Peng, A. Petrone, T. Henderson, D. Ranasinghe, V. G. Zakrzewski, J. Gao, N. Rega, G. Zheng, W. Liang, M. Hada, M. Ehara, K. Toyota, R. Fukuda, J. Hasegawa, M. Ishida, T. Nakajima, Y. Honda, O. Kitao, H. Nakai, T. Vreven, K. Throssell, J. A. Montgomery, Jr., J. E. Peralta, F. Ogliaro, M. Bearpark, J. J. Heyd, E. Brothers, K. N. Kudin, V. N. Staroverov, T. Keith, R. Kobayashi, J. Normand, K. Raghavachari, A. Rendell, J. C. Burant, S. S. Iyengar, J. Tomasi, M. Cossi, J. M. Millam, M. Klene, C. Adamo, R. Cammi, J. W. Ochterski, R. L. Martin, K. Morokuma, O. Farkas, J. B. Foresman, and D. J. Fox, Gaussian, Inc., Wallingford CT, 2016.

[49] NBO Version 3.1, E. D. Glendening, A. E. Reed, J. E. Carpenter, and F. Weinhold.

[50] J. Tirado-Rives and W. L. Jorgensen, “Performance of B3LYP Density Functional Methods for a Large Set of Organic Molecules,” J. Chem. Theory Comput., vol. 4, no. 2, pp. 297–306, Feb. 2008.

[51] S. Acosta-Gutiérrez et al., “Getting Drugs into Gram-Negative Bacteria: Rational Rules for Permeation through General Porins,” ACS Infect. Dis., vol. 4, no. 10, pp. 1487–1498, Oct. 2018.

[52] I. Ghai et al., “General Method to Determine the Flux of Charged Molecules through Nanopores Applied to β-Lactamase Inhibitors and OmpF,” J. Phys. Chem. Lett., vol. 8, no. 6, pp. 1295–1301, 2017.

[53] M. A. Scorciapino, T. D’Agostino, S. Acosta-Gutierrez, G. Malloci, I. Bodrenko, and M. Ceccarelli, “Exploiting the porin pathway for polar compound delivery into Gram-negative bacteria,” Future Med. Chem., vol. 8, no. 10, pp. 1047–1062, Jun. 2016.

[54] M. A. Scorciapino et al., “Rationalizing the permeation of polar antibiotics into Gram-negative bacteria,” J. Phys. Condens. Matter, vol. 29, no. 11, p. 113001, Mar. 2017.

[55] PLUMED, “Trieste tutorial: Averaging, histograms and block analysis.” [Online]. Available: https://plumed.github.io/doc-v2.4/user-doc/html/trieste-2.html.

[56] PLUMED, “Exercise 3: estimating the error in free-energies using block-analysis.” [Online]. Available: https://plumed.github.io/doc-v2.4/user-doc/html/trieste-4.html.

[57] T. D’Agostino, “Enhanced sampling methods and their application in the study of molecular permeation in gram-negative bacteria.”

[58] L. Maragliano and E. Vanden-Eijnden, “A temperature accelerated method for sampling free energy and determining reaction pathways in rare events simulations,” Chem. Phys. Lett., vol. 426, no. 1–3, pp. 168–175, Jul. 2006.

Acknowledgments

The Ph.D. is only the height of my university career and at this point thanks must be done.

First of all, I would like to thank Prof. Mariano Casu who since my Bachelor's degree welcomed me into his research group, I'm honored by this!

Since that time I met Dr. Andrea Scorciapino who has helped me during all my career, from my Bachelor and Master thesis during all three years long of my Ph.D., for this I'm really grateful to him.

Furthermore, I wold like to thank Prof. Matteo Ceccarelli for trusting me during these three years and giving me the means to carry out my work.

I'm grateful to Dr. Silvia Acosta Gutiérrez too, she was close to me in difficult moments. Finally, thank to Prof. Francesco Luigi Gervasio who welcomed me to his research group in London and for his help.

It has been a long and tiring route and finally I can see the end…